

Non-Gaussianity in D3-brane inflation

Kareem Marzouk, ¹ Alessandro Marajo, ^{1,2} David Seery ¹

¹Astronomy Centre, University of Sussex, Falmer, Brighton, BN1 9QH, UK

²Institute for Astronomy, Royal Observatory, Blackford Hill, Edinburgh, EH9 3HJ, UK

E-mail: B.K.Marzouk@sussex.ac.uk, Marajo@roe.ac.uk, D.Seery@sussex.ac.uk

Abstract. We update predictions for observables in the ‘delicate’ D3/ $\overline{\text{D3}}$ inflationary model on the conifold. We use a full CMB likelihood calculation to assess goodness-of-fit, which is necessary because in this model the ζ power spectrum often cannot be approximated as a power-law over observable scales. For the first time we are able to provide accurate forecasts for the amplitude of three-point correlations. In a significant portion of its parameter space the model follows Maldacena’s single-field prediction $f_{\text{NL}} \approx -(5/12)(n_s - 1)$ if $|n_t| \ll 1$. Therefore $|f_{\text{NL}}|$ is usually small when the power spectrum satisfies observational constraints. In a small number of cases the bispectrum is instead dominated by effects from rapid switching between angular minima. The resulting amplitudes are larger, but mostly with unacceptable spectral behaviour. In the most extreme case we obtain $|f_{\text{NL}}^{\text{eq}}| \sim 75$ at $k_t/3 = 0.002 \text{ Mpc}^{-1}$. It has been suggested that the quasi-single field inflation (‘QSFI’) mechanism could produce significant 3-point correlations in this model. We do observe rare shifts in amplitude between equilateral and squeezed configurations that could possibly be associated with QSFI effects, but more investigation is needed to establish the full bispectrum shape. There is evidence of ‘shape’ running between equilateral and squeezed configurations that may be inherited from the scale dependence of the spectrum. We explore the dependence of observables on discrete choices such as the truncation point of the potential. Our analysis illustrates the advantages of a standard format for information exchange within the inflationary model-building and testing community.

¹The first two authors made equal contributions to the work reported in this paper.

Contents

1	Introduction	3
2	The $D3/\overline{D3}$ model of inflation	13
2.1	The conifold geometry	13
2.2	The D3-brane potential	16
2.3	Harmonic analysis on the conifold	18
2.4	Flux contributions	23
3	Experimental procedure	29
3.1	Software stack and sampling strategy	30
3.1.1	CppTransport pipeline	30
3.1.2	Computational issues	33
3.1.3	PyTransport pipeline	37
3.2	The adiabatic limit	38
3.3	Agreement between pipelines	39
4	Results	42
4.1	Background evolution and mass spectrum	43
4.2	Two- and three-point observables	48
4.2.1	Two-point observables	48
4.2.2	Three-point correlations	53
4.2.3	Squeezed configurations	56
4.2.4	Large non-Gaussianity from rapid change of angular minima	58
4.3	‘Small’ ensemble comparisons	60
5	Discussion	62
A	Data availability	66
B	Computational requirements	67
C	Transport equations for the spectral index	69
C.1	Scalar spectral index	69
C.2	Tensor spectral index	72

List of Figures

1	Schematic representation of the conifold geometry	15
2	Convergence test with increasing subhorizon e-folds	35
3	CppTransport/PyTransport comparison: Distribution of $f_{\text{NL}}^{\text{eq}}$ and n_s	40
4	CppTransport/PyTransport comparison: Distribution of $f_{\text{NL}}^{\text{eq}}$ and n_s in the cut region $A_s > 10^{-4}$	41
5	Background evolution for 100 sample trajectories	43
6	Evolution of mass spectrum in the primary catalogue	44
7	Distribution of slow-roll parameters at 60 e-folds	46
8	Posterior distribution of Q and α	47
9	n_s vs. r for primary catalogue	48
10	Power spectra for best-fit trajectory #43, 942	50
11	Power spectra for trajectory #88, 167	50
12	r vs. n_t for primary catalogue	53
13	$f_{\text{NL}}^{\text{eq}}$ vs. $f_{\text{NL}}^{\text{fold}}$ for primary catalogue	54
14	Distribution functions for $ f_{\text{NL}}^{\text{eq}} $	56
15	Analysis of $f_{\text{NL}}^{\text{sq}}$ and shape response	57
16	Example trajectory showing abrupt change between angular minima	59
17	Mass distribution for ‘small study’ with homogeneous terms only	61
18	Change in observables for ‘small study’ with homogeneous terms only	62
19	Distribution of A_s in the primary catalogue and ‘small study’ with $\alpha = 0$	62
20	Distribution of integration times in the primary catalogue	69

1 Introduction

Inflation continues to retain its favoured position as the leading scenario for the origin of structure in the universe—but there has been little progress towards identifying the degrees of freedom that were active during the inflationary era, or the manner in which they interacted. Among the major reasons for this slow progress are well-rehearsed arguments showing that inflation is sensitive to small, nonrenormalizable interactions suppressed by Planck-scale masses, and therefore may depend on the precise way in which the inflationary sector is embedded within its ultraviolet completion.

This phenomenon is not a failure of decoupling in the technical sense [1], but shares its double-edged character. On the one hand, if successful inflation can depend on physics at or near the Planck scale, we are encouraged to believe that it may be possible to discover details of quantum gravity by studying inflationary observables. On the other, dependence on high-scale physics means that inflation can *not* be studied on its own: assumptions about physics at higher energies are required, even if they are not made explicit. The predictivity of the scenario is therefore reduced.

This situation has encouraged development of approaches in which inflationary model-building takes place in the context of a concrete proposal for its ultraviolet completion. The most well-developed of these use string theory as the ultraviolet model, paired with a variety of suggestions for the microscopic origin of the low-energy fields that populate the inflationary sector. The field was surveyed at length in a recent monograph by Baumann & McAllister [2].

One proposal is that inflation is driven by the dynamics of a $D3/\overline{D3}$ brane pair within a warped deformed conifold. The attraction of this scenario is not that we think it more realistic than any other model, but that it is highly computable. In particular, the functional form of the low-energy effective action can be computed reliably, even accounting for contributions from moduli stabilization and supersymmetry breaking. This high degree of computability is remarkable.

The most significant drawback is the complexity of the resulting effective theory: the potential we describe in §2 below has 1,212 independent parameters and is a sum of 3,881 terms, many of which are themselves complicated. Numerical methods are necessary: it is impractical to extract observational predictions from such complex potentials using analytical techniques. Progress therefore becomes dependent on compute resource and the availability of suitable software tools. It is arguable that analysis of this model—and others of comparable complexity—has been hampered by *both* the paucity of powerful, general-purpose software tools for inflationary model analysis, *and* an accepted means for exchanging the specification of models within the community. In the sister discipline of collider phenomenology these roles are played by the FeynRules system and its [online model database](#) [3, 4].

These disadvantages notwithstanding, its unusual theoretical control has made the $D3/\overline{D3}$ model an interesting laboratory in which to study the likelihood of inflation, the distribution of observables such as the primordial spectral index, and the prospects for accommodating fine-tuning issues such as the well-known ‘ η -problem’ (that is, light scalar fields in a quasi-de Sitter spacetime typically acquire masses of order H). For these reasons the model has developed its own literature, which we review briefly beginning on p. 5.

Non-Gaussianity and observables.—In this paper we return to the $D3/\overline{D3}$ model and re-analyse it using updated numerical methods. Our principal aim is an accurate characterization of the primordial non-Gaussianity it produces, for which reliable estimates have not yet been reported. To achieve this we leverage new versions of the **CppTransport** [5, 6] and **PyTransport** [7, 8] codes that automate evaluation of inflationary correlation functions directly from low-energy effective action. Such automated methods are the most practical way to handle models whose numerical implementation is otherwise too laborious or error-prone, especially for calculation of three-point statistics. Some details of the improvements in the new versions of these codes are described below, but they will be discussed more completely in a forthcoming publication.

The underlying technology is an evolution of the ‘transport’ method already used to analyse the $D3/\overline{D3}$ model by Dias et al. [9]. It has already been described in the literature [10–15], and our implementation introduces no significant novelties compared to these treatments. Therefore we recapitulate only those properties relevant to our analysis or its interpretation. First, neither implementation makes use of the slow-roll approximation and therefore time dependence is treated exactly. However, in common with all other general-purpose frameworks for calculation of inflationary correlation functions, the **CppTransport** and **PyTransport** implementations are valid only to tree-level. Here, ‘tree-level’ has its usual meaning in which a term at n^{th} order in the loop expansion involves n unrestricted momentum integrals. There are two types of loop in the Schwinger (or ‘in–in’) formalism appropriate for cosmological correlation functions [16–18]. The first type represent the familiar averages over virtual quanta that appear in ‘in–out’ amplitudes, and can be absorbed into a renormalization of masses, coupling constants and field amplitudes.¹ The second type can be regarded as averages over unobserved physical particles, which may include decay products or particles generated from non-adiabatic evolution, including resonance [19, 20]. Momentum integrals of this type are a measure of back-reaction from these particle production processes. Any tree-level framework, including the transport method, is blind to this back-reaction. In this paper we simply assume there is no problematic back-reaction from particle production. However, see footnote 23 on p. 44.

What *is* included? In both two- and three-point functions we capture all effects from quadratic mixing between modes on superhorizon scales where momenta are soft compared to H in the sense $k/(aH) \ll 1$, and even small off-diagonal terms in the mass matrix are relevant. In the traditional language of inflationary phenomenology these effects describe transfer of power between adiabatic and isocurvature modes. Meanwhile, in the three-point function we capture the effect of three-body interactions. These can loosely be regarded as describing processes in which a pair of particles are produced from the gravitational field, before one member of the pair decays into two daughter particles [21, 22]. At later times the three resulting particles are correlated due to their shared history.

We capture effects from any nontrivial mass spectrum, including modes that are much lighter ($m \ll H$), much heavier ($m \gg H$), or comparable to the Hubble scale ($m \sim H$). At horizon exit these effects can reduce the amplitude of fluctuations, or change the subtle

¹A major advantage of the AdS/CFT computation used to obtain the D3-brane potential is that it accounts automatically for mixing between scales that is usually generated by averaging over virtual quanta.

interference effects imprinted in the three-point function—and higher-order correlations—from interaction between growing and decaying modes. They may also induce significant correlations, or anti-correlations, between the field degrees of freedom at horizon exit.

To detect the emergence of an adiabatic limit before the end of inflation we employ a technique based on tracking eigenvalues of the mass matrix [23, 24]. If an adiabatic limit is reached this implies the model is predictive without the need to specify details of a later reheating phase [23, 25–32].

Because our interest lies in computation of observables, the **CppTransport** and **PyTransport** codes are only the front-end of a longer pipeline. Once the inflationary computation is complete, the two-point function is used as an initial condition for the **CLASS** Boltzmann code [33].² This enables us to generate custom predictions for the CMB angular power spectra C_ℓ and hence the likelihood function. This is particularly important for the D3/ $\overline{\text{D3}}$ model because it frequently produces power spectra with significant scale dependence [9]. Summary statistics evaluated at a single scale—such as the scalar amplitude A_s and spectral index n_s —are therefore misleading, and use of the full primordial power spectrum is required. The entire pipeline is controlled by the **CosmoSIS** parameter estimation framework [34], allowing it to be attached to a number of efficient general-purpose sampling algorithms. We collect values for observables built from the two- and three-point functions and use these to estimate distribution functions. Our focus is on general properties of perturbations produced by the model, whether or not their statistical character falls in an observationally viable window.

Using this pipeline we are able to study the distribution of the three-point correlation amplitude on representative ‘equilateral’ and ‘folded’ configurations (where $k_1 \sim k_2 \sim k_3$ and $k_1 \sim k_2 \sim k_3/2$, respectively, if $\mathbf{k}_1, \mathbf{k}_2, \mathbf{k}_3$ are the 3-momenta appearing in the three-point correlator). ‘Squeezed’ configurations, where one of the k_i becomes significantly smaller than the other two, are substantially more expensive to simulate and we are not able to compute these for every realization. This is unfortunate because it is the squeezed correlation amplitude that can be measured most cleanly [35]. Instead, we study how the squeezed amplitudes correlate with the equilateral and folded ones by constructing a separate, smaller sample. From this we infer the behaviour of squeezed configurations in our full catalogue.

Previous results.—The brane inflation paradigm was introduced by Dvali & Tye [36], and elaborated into the concrete D3/ $\overline{\text{D3}}$ scenario by Burgess et al. [37] and Dvali et al. [38]. The branes carry opposite charges, and in early work the resulting Coulomb attraction was identified with the inflationary potential. Unfortunately, this proposal was not viable due to phenomenological difficulties.

Kachru et al. (‘KKLMMT’ [39], following earlier work by ‘KKLT’ [40]), showed that

²We use only the primordial two-point function (evaluated at the end of inflation) as an initial condition for the subsequent CMB calculation. We could equally well use this as an initial condition for the matter or galaxy power spectra, but we do not do so here because constraining the model from data is not the primary purpose of this paper and significant extra complexity is needed to describe galaxy bias. However, if desired, the flexibility of the **CosmoSIS** framework makes it simple to include more datasets in the likelihood calculation.

We will see below that computations of the primordial three-point function are still sufficiently expensive that we cannot routinely compute the *shape* of the bispectrum, for example to accurately model scale-dependent bias in the power spectrum, or to compute a full CMB bispectrum. We comment on the computational challenges in §3.1.2 and Appendix B below.

the Coulomb potential would be flattened by warping of the metric in the extradimensional space. Such warped-product geometries were already familiar from the Randall–Sundrum scenario [41, 42]. Although the flattened potential relieved most phenomenological problems, Kachru et al. demonstrated that it would receive significant corrections from effects due to moduli stabilization [39] and in particular that these would lift the inflaton mass to be of order H . This is a manifestation of the familiar η -problem of inflation. The conclusion is that successful D3/ $\overline{\text{D3}}$ inflation would have to be regarded as a ‘delicate’ accident caused by partial cancellation to produce a mass smaller than H .

An explicit computation of these corrections was given by Baumann et al. [43] for the case where stabilization is due to D7-branes wrapping four-cycles of the extradimensional space. The implications for D3/ $\overline{\text{D3}}$ inflation were summarized in Refs. [44, 45]. Their calculation showed that, by fine-tuning the cancellation between different effects, a small window existed for inflation to occur near an inflexion point of the D3-brane potential.

The approach used in these papers left open the question of what happens when moduli stabilization occurs by a more general mechanism. This issue was taken up by Baumann et al., first in a linearized analysis [46] and later including nonlinear effects [47, 48]. Their most developed method made use of the AdS/CFT correspondence to map operators in the D3-brane potential to the spectrum of non-normalizable perturbations of the warped conifold. These perturbations can be determined by harmonic analysis of the conifold base space, the coset space $T^{1,1}$, for which the necessary tools had already been assembled by Gubser [49] and Ceresole et al. [50, 51]. We review this method of constructing the brane potential in §2.

Inflationary analysis.—Each of these computations yields a prediction for the functional form of the D3-brane potential, parametrized by a number of mass scales M_i . These scales may be regarded as encoding ultraviolet information about the compactification that has been integrated out to produce the low-energy description. In our present state of ignorance they cannot be computed and must be estimated from observations.

If the low-energy effective action were to be expanded in a basis of local operators, the Wilson coefficient for each operator would be determined by the mass scales M_i . These coefficients would all have been regarded as independent by the methods of traditional effective field theory (‘EFT’). For the D3 model, however, relationships inherited from the functional form of the brane potential imply that certain Wilson coefficients are correlated or even absent. It is these correlations that represent the gain in information from using an explicit ultraviolet completion in contrast to a traditional analysis using an ultraviolet-agnostic EFT. We will see below that the likelihood of inflation and its detailed predictions can depend on this pattern of correlations. This clearly illustrates the weak decoupling between inflation and the assumed ultraviolet model.

Agarwal et al. assessed the importance of these correlations between the low-energy coefficients by repeatedly drawing values for the M_i from a specified distribution [52]—a strategy that had been introduced earlier by Easter, Peiris and collaborators [53, 54]. Assuming inflation would always begin from the same initial field configuration, Agarwal et al. were able to determine its likelihood as a function of the number of e-folds achieved. They also determined the distribution of the single-scale summary statistics A_s , n_s and r derived

from the two-point function. Because the angular directions are typically heavy they argued that an effectively unique inflationary trajectory would often emerge, and used a single-field approximation based on this trajectory to estimate observables. This approximation does not capture multiple-field effects that transfer power between entropic modes and the curvature perturbation. It also does not account for the contribution of fields that are not light compared to the Hubble scale.

Agarwal et al. used an ensemble of $> 70,000,000$ realizations to study the homogeneous background, finding that the probability of more than 60 e-folds of inflation was small, of order 10^{-5} to 10^{-4} . Two further ensembles were used to study observables: one with 4,900,000 realizations, of which 8,301 yielded more than 60 e-folds; and a second with 500,000 realizations, of which only 750 yielded more than 60 e-folds. The two ensembles differed in their truncation of the D3-brane potential, to be described in §2. Agarwal et al. concluded that the tensor–scalar ratio r would typically be unobservable, and that the scalar spectral index n_s fell roughly in the range $0.94 \lesssim n_s \lesssim 1.10$, with values in the WMAP7 range $n_s = 0.963 \pm 0.014$ (at $k = 0.002 \text{ Mpc}^{-1}$ [55, 56]) coming from cases where the single-field treatment was likely to be acceptable. Their results did not depend strongly on the truncation.

In a small fraction of cases, Agarwal et al. observed abrupt transitions between different angular minima and speculated that these might generate significant non-Gaussianity from multiple-field effects [23, 24]. Our results demonstrate that this suggestion is essentially correct. Indeed, the amplitude of three-point correlations generated in this way can be surprisingly large, although trajectories that exhibit the effect are rare within our ensemble.

Dias et al. used a more sophisticated numerical scheme to compute observables [9], based on superhorizon ‘transport’ of the inflationary correlation functions [10, 11, 24, 57, 58]. This approach was a precursor of the technology we deploy in this paper. (The approach used here is more complete because it correctly accounts for subhorizon effects.) Their method correctly tracked transfer of power on superhorizon scales, including contributions from fields that were not light at the time of horizon exit. Like the scheme of Agarwal et al., it applied only to the two-point function.³ As part of their analysis, Dias et al. attempted to quantify how many instances of inflation converged to an adiabatic limit. As explained above, when this occurs it implies that the model is predictive without specifying the details of a later reheating phase. Conversely, if an adiabatic limit is not reached, the final value of each observable may depend on the details of reheating [32].

Dias et al. used an ensemble with 564 realizations giving more than 60 e-folds of inflation. Within the statistical limits of their sample size, these results confirmed the conclusion of Agarwal et al. that r would be negligible, and yielded a comparable distribution for n_s . In most cases, they found that an adiabatic limit would be reached during the inflationary

³Strictly this applies to v2 of the arXiv version of this paper, which includes an erratum to the published version (matching arXiv v1). Originally this paper contained an error from omission of the conifold metric, pointed out in Ref. [59], which caused all fields to be light at horizon exit. Based on this error the published version included a discussion of the f_{NL} observable, but its conclusions were invalidated when the correct conifold metric was introduced in the erratum. We would like to thank Mafalda Dias and Jonathan Frazer for helpful correspondence, and for kindly sharing their Mathematica code.

phase.

Later, McAllister, Renaux-Petel & Xu studied the same model using a different numerical technique, finding 18,731 realizations that yielded at least 66 e-folds of inflation [59]. They found that 21% of their realizations were consistent with WMAP7 constraints on n_s (see above). In agreement with Agarwal et al., these realizations typically exhibited a unique inflationary trajectory over the final 60 e-folds of inflation, making a single-field treatment sufficient. This usually occurs when inflation is of long duration, with multiple-field effects appearing only as transients at early times. Finally, based on an analytic approximation for the ‘quasi single-field’ regime [60–62], they suggested that three-point correlations on squeezed configurations could occasionally become large, with $|f_{\text{NL}}| \gtrsim 10$ in perhaps 0.07% of realizations. If it occurs, this form of non-Gaussianity has a very different origin to the rapid shifting between angular minima suggested by Agarwal et al. Unfortunately, detecting the presence of ‘quasi single-field’ effects is numerically expensive, and in this paper we are not yet able to form a definitive judgement regarding their occurrence.

A different approach was pursued by Hertog & Janssen [63], who studied the possibility of eternal inflation near the flat inflexion point that characterizes inflating potentials in the D3/ $\overline{\text{D3}}$ model. This is very similar to the proposal of topological inflation [64, 65]; see Ref. [66] for an analysis of non-Gaussianity in related models. Hertog & Janssen computed observables in their scenario using a prior based on the no-boundary wavefunction proposal. Accordingly the observable distributions reported by these authors cannot be compared with those given here, although their suggestion $|f_{\text{NL}}| < 10^{-4}$ within their ensemble is notable.

Organization of this paper.—To build our primary catalogue required sampling more than 450,000,000 trajectories, of which over 90,000 yielded more than 60 e-folds of inflation. It will be explained in §3.3 that some of these are excluded due to concerns about representative sampling, leaving roughly 55,000 ‘safe’ trajectories for which observables can be computed. This is nearly three times the number of trajectories used by McAllister et al., and nearly 100 times the number used by Dias et al. The large sample size means we are able to characterize the distribution of each observable with reasonable accuracy. (However, we will see that there is evidence we still undersample away from the central region for some distributions.) The main obstruction to generating even larger ensembles is compute time. Running on a Haswell-era compute cluster, our production code required $\sim 95,000$ CPU hours to build the primary catalogue, and a further $\sim 40,000$ CPU hours to compute observables for each trajectory. We comment further on the resource requirements for the computation in Appendix B.

This primary catalogue is complemented by a number of ‘small’ catalogues, each comprising roughly 18,000 inflating trajectories, that are used to study the dependence of observables on various arbitrary choices made during construction of the model. These include the way the potential is truncated, the initial conditions for inflating trajectories, and the treatment of contributions to the brane potential from bulk fluxes (see §2.4). Each of these ‘small’ catalogues has similar size to the current best-in-class analysis reported in Ref. [59], giving us considerable statistical power when comparing distributions.

In §2 we review the construction of the D3-brane potential, paying particular attention to the harmonic modes on $T^{1,1}$. The elements of this discussion have all been given before,

but are scattered across a number of papers. We collect the relevant formulae in a unified notation.

During the course of this work we discovered instances where inadvertent omissions meant that previous analyses of this model had not been described in sufficient detail to allow replication. These relate to minor technical choices in the construction of the D3-brane potential or in specifying priors for the sampling procedure. To assist authors who wish to replicate our own analysis we have attempted to document the construction of the potential in sufficient detail to allow replication if desired. Our trajectory catalogues are available for download from the Zenodo open-access repository, and may be re-used under a permissive Creative Commons licence. (See Appendix A.) Further, our computational pipelines are open source and published on GitHub. We would like to thank the authors of the previous studies for their ready assistance in relating our analysis to theirs.

The reader whose interest lies solely with the prediction of inflationary observables may wish to skip §2, which involves ideas from extradimensional compactifications in string theory, and return to it only to understand the relationship between parameters. For this purpose Tables 1 and 2 may be helpful. Conversely, readers who are already familiar with the detailed constructions of Refs. [47, 48] will not find any new material and may also wish to proceed directly to §3.

In §3 we describe our software stack and the numerical method used to compute observables. We document our choice of priors and initial conditions, and the precise sampling strategy we apply to build both the primary catalogue and the ‘small’ catalogues used for comparison. In §3.1.1 and §3.1.3 we explain how observables are computed within each pipeline, and in §3.1.2 we discuss general computational issues that arise within the transport framework irrespective of implementation. In §3.2 we describe our procedure for detecting an adiabatic limit at the end of inflation. Finally, in §3.3 we compare the distributions reported by each pipeline and develop a choice of cuts intended to ensure the integrity of our analysis. Imposing these cuts reduces our primary catalogue from (roughly) 90,000 to 55,000 trajectories, as explained above.

In §4 we study the distribution for each observable over the catalogues constructed in §3. §4.1 discusses the behaviour of trajectories at the level of the background. In §4.2.1 we consider observables derived from the two-point function, and in §4.2.2 we extend this to include information on three-point correlations on equilateral, folded, and (via a separate catalogue) squeezed configurations. We compare our distributions with results previously given in the literature. In §4.2.4 we discuss a population of rare trajectories that exhibit the abrupt transitions between angular minima observed by Agarwal et al., and show that these yield very large three-point correlations of ‘local’ shape. Finally, we conclude in §5. Three appendices summarize information tangential to the main discussion. Appendix A provides information about the data deposit accompanying this paper. Appendix B gives more details on computational resource requirements. Appendix C summarizes the ‘transport’ computation of spectral indices, including new subleading terms intended to accelerate convergence.

Notation and conventions.—We work in natural units where $c = \hbar = 1$. The reduced Planck

mass is defined by $M_{\text{P}} = (8\pi G)^{-1/2}$ and is numerically equal to 2.435×10^{18} GeV. Latin indices a, b, \dots , label coordinates in four-dimensional space, and indices A, B, \dots , label coordinates in the six-dimensional compact space. The distributions $U(a, b)$ and $N(\mu, \sigma)$ are the uniform distribution with lower limit a and upper limit b , and the normal distribution of mean μ and standard deviation σ , respectively.

The D3/ $\overline{\text{D3}}$ model is very complicated—indeed, it may be the most complicated model for which inflationary observables have yet been computed. Its description entails a heavy overhead of notation. To assist readers who are unfamiliar with this maze of definitions we provide a glossary in Tables 1–2. Table 1 lists the parameters of the potential, together with their mass dimension, point of definition, and whether they are fixed, sampled, or derived quantities in our sampling procedure. Table 2 provides similar information for other relevant quantities that do not parametrize the potential.

In §2.2 and Appendix C we discuss the effective field theory for the D3-brane system and its fluctuations, for which we briefly summarize our conventions. The effective field theory comprises six scalar fields X^A inherited from the extradimensional coordinates, with momenta $\pi^A = \text{d}X^A/\text{d}N$, where $N = \int^t H \text{d}t$ represents the accumulated e-folds of expansion. We collect the fields and momenta into a phase space coordinate $\mathcal{X}^{\mathbb{A}}$ with index \mathbb{A} . The corresponding fluctuations are $\delta\mathcal{X}^{\mathbb{A}}$.

parameter ^a	mass dim.		definition	type
$r_{\text{IR}} = x_{\text{IR}} r_{\text{UV}}$	-1	IR limit of throat	p. 14	derived
$r_{\text{UV}} = \phi_{\text{UV}}/T_3^{1/2}$	-1	UV limit of throat	p. 14	derived
T_3	4	D3-brane tension	p. 14	fixed
x_{IR}	0	r_{IR} in dimensionless x coordinate	p. 16	fixed
ϕ_{UV}	1	UV limit of throat in ϕ coordinate	p. 16	fixed
$Z = (2M_{\text{P}}/\phi_{\text{UV}})^2$	0	D3-brane charge	p. 16	derived
$a_0 = e^{A(r_{\text{IR}})}$	0	value of warp factor at IR limit of throat	p. 17	fixed
$g_s = e^{\phi}$	0	string coupling	p. 16	not required
$D_0 = 2T_3 a_0^4$	4	normalization of Coulomb potential	p. 17	derived
$V_0 = \alpha D_0$	4	energy density from distant supersymmetry breaking	p. 17	derived
$\mu = (V_0 + D_0)^{1/4}(\phi_{\text{UV}}/M_{\text{P}})^{1/2}$	1	mass scale in $V_{\mathcal{H}}$ and $V_{\mathcal{F}}$	p. 17	derived
C_{LM}	0	Wilson coefficients for zero-model labelled by LM	p. 21	sampled
$D_{LM} = C_{LM} + C_{-L-M}^*$	0	combined Wilson coefficient for mode LM if $L > 0$	p. 23	derived
\mathcal{C}_{LM}	0	Wilson coefficient for flux mode LM	p. 29	sampled
α	0	relative magnitude of V_0 and D_0	—	sampled
Q	0	typical distance to nearest D7-brane stack ^b	—	sampled ^c

^a The initial conditions for the fields ϕ^A and their velocities $\dot{\phi}^A$ do not vary in our primary ensemble and do not appear in this table. See the discussion in §3.

^b The Q parameter was introduced by Agarwal et al. [52] [see Eq.(10) of this reference]. It effectively sets the normalization for the Wilson coefficients C_{LM} and \mathcal{C}_{LM} .

^c This prior for Q is selected with foreknowledge of the Q posterior and a view to sampling efficiency. We will see in §4 that Q -values which frequently allow $N > 60$ e-folds of inflation are rather tightly clustered. We have verified that our final distributions for observables are unchanged if we select a weaker, broad prior for Q , except that the sampling process spends more time in regions of parameter space where $N > 60$ e-folds are unlikely. We use the uniform prior quoted here only in the **CppTransport** pipeline. The **PyTransport** pipeline instead uses a 'beta-prime' distribution $\beta'(\alpha, \beta)$ with shape parameters $\alpha = 4.16$, $\beta = 4.94$. See the discussion of the Q -prior in §3.1.3. Note that this α parameter is not the same as $\alpha = V_0/D_0$ appearing in the table.

Table 1. Glossary of parameters for the D3/D $\overline{\text{D3}}$ model.

Table 2. Glossary of notation for the D3/ $\overline{\text{D3}}$ model.

quantity		definition
$T^{1,1}$	Romans manifold $SU(2) \times SU(2)/U(1)$; base of conifold	p. 13
G_{AB}	conifold metric	p. 13
$G_{AB}^{T^{1,1}}, ds_{T^{1,1}}^2$	metric on $T^{1,1}$	p. 16
$A(r)$	Klebanov–Strassler warp factor	p. 13
H	generator of $U(1)$ divisor in $T^{1,1}$	p. 14
K	generator of $U(1)$ R -symmetry of $T^{1,1}$	p. 14
T_i	generators of $SU(2)$	p. 14
$\Psi = (\theta_1, \theta_2, \phi_1, \phi_2, \psi)$	coordinates on $T^{1,1}$	p. 14
r	radial coordinate on the conifold	p. 13
$C_4 = \alpha \omega$	Chern–Simons form coupling to D3-brane ^a	p. 14
ω	volume form on D3-brane; $\omega = \star 1$	p. 14
γ_{ab}	induced metric on D3-brane	p. 14
X^A	embedding coordinates $X^A = X^A(x^a)$ of D3-brane	p. 15
$\Phi_- = e^{4A} - \alpha$	supergravity field; AdS/CFT dual to D3-brane potential ^a	p. 15
$x = r/r_{\text{UV}}$	dimensionless D3-brane radial coordinate	p. 16
R_4	4-dimensional Ricci scalar on D3-brane	p. 16
Λ	3-form flux derived from G_3	p. 16
G_3	3-form field of Type IIB supergravity	p. 16
$V_{\mathcal{C}}$	Coulomb contribution to potential	p. 16
$V_{\mathcal{M}}$	mass term in potential from R_4	p. 17
$V_{\mathcal{H}}$	‘complementary function’ part of potential	p. 18
$V_{\mathcal{F}}$	‘particular integral’ part of potential	p. 18
(μ)	label for representations of a Lie group G	p. 18
$D_{mm'}^{(\mu)}(\beta)$	Wigner’s D -matrix in representation (μ)	p. 18
$d_{mm'}^{(\mu)}(\beta)$	Wigner’s little d matrix in representation (μ)	p. 19
$L(g)$	coset representative of group element g	p. 18
$L = (\ell_1, \ell_2, R)$	labels representation of isometry group $SU(2) \times SU(2) \times U(1)$	p. 20
$M = (m_1, m_2)$	runs over representation space for representation L	p. 20
$\mathcal{E}_{LM}(\Psi)$	harmonic on $T^{1,1}$	p. 19
Λ_L	eigenvalue of \mathcal{E}_{LM} in Laplacian $\nabla_{T^{1,1}}^2$	p. 20
$J_{\ell,m,R}^{\text{r}}(\theta), J_{\ell,m,R}^{\Omega}(\theta)$	normalized θ modes on $T^{1,1}$	p. 20
$\Delta(L) = -2 + \sqrt{4 + \Lambda_L}$	scaling dimension of zero-mode for representation L	p. 21
Δ, δ	scaling dimensions <i>unrelated</i> to L	p. 23
$\mathfrak{Gr}(x, x'), g_L(r, r')$	Green’s function on conifold and eigensum decomposition g_L	p. 25
$\mathcal{L}, \mathcal{M}, \mathcal{R}$	quantum numbers in Clebsch–Gordan expansion	p. 28
\mathbb{L}, \mathbb{M}	$\mathbb{L} = (\mathcal{L}_1, \mathcal{L}_2, \mathcal{R}), \mathbb{M} = (\mathcal{M}_1, \mathcal{M}_2)$	p. 28
$\mathcal{A}(L, L', \mathbb{L})$	unknown amplitude in Clebsch–Gordan expansion	p. 28

^a The α appearing in C_4 and Φ_- is the same, but not the same α that appears in Table 1.

2 The D3/ $\overline{\text{D3}}$ model of inflation

The D3/ $\overline{\text{D3}}$ model has been studied extensively in the literature, to which we refer for a more complete account of its construction [36, 37, 39, 43–48, 67]; see also Ref. [2] for a textbook description. In this section we recall only those details needed to fix notation or make our account self-contained. Our primary intention is to give an unambiguous specification of the D3-brane potential and its parametrization.

In §2.1 we recall the geometry of the conifold and explain how its four-dimensional low energy description can support an inflationary phase. In §2.2 we summarize the procedure of Baumann et al. for constructing the D3-brane potential [47, 48]. This depends on the details of harmonic analysis on the conifold, originally discussed by Gubser [49] and Ceresole et al. [50, 51], and summarized here from a different perspective in §2.3. These details are used to construct zero modes of the conifold Laplacian, which represent a class of contributions to the brane potential from ‘unsourced’ deformations of the conifold geometry. Finally, in §2.4 we give our prescription for a second class of ‘sourced’ deformations. Although these have been included in previous analyses, certain arbitrary choices are required to completely specify their contribution. In this section we document our choices in sufficient detail (at least in intention) to allow replication of our analysis.

2.1 The conifold geometry

In the model, a mobile D3-brane moves in an extradimensional space due to its mutual Coulomb attraction with a distant $\overline{\text{D3}}$ -brane. From the perspective of a four-dimensional observer, the displacement between the branes in each coordinate can be regarded as a four-dimensional scalar field. These fields will be nearly homogeneous if the branes are nearly parallel. The forces experienced by the brane as it moves in the extradimensional space can be summarized as an effective potential for the displacement in each coordinate.

The Klebanov–Strassler throat.—It was explained in §1 that the Coulomb force generates a potential that is too steep to support inflation if the extradimensional geometry is flat. To flatten the potential requires warping in the extradimensional space. A candidate geometry is the singular warped conifold studied by Klebanov & Strassler [68]. The ten-dimensional metric is a warped product,

$$ds^2 = e^{2A} g_{ab} dx^a dx^b + e^{-2A} G_{AB} dX^A dX^B, \quad (2.1)$$

where g_{ab} is the four-dimensional spacetime metric with coordinates x^a and G_{AB} is the metric on the transverse extradimensional space with coordinates X^A . We take this to be a cone over the Romans space $T^{1,1} = SU(2) \times SU(2)/U(1)$ [69],

$$G_{AB} dX^A dX^B = dr^2 + r^2 ds_{T^{1,1}}^2. \quad (2.2)$$

The geometry is supposed to be supported by a stack of $Z \gg 1$ D3-branes positioned at the

tip. The base space $T^{1,1}$ is five-dimensional⁴ and carries the metric [70]

$$ds_{T^{1,1}}^2 = \frac{1}{9} \left(d\psi + \sum_{i=1}^2 \cos \theta_i d\phi_i \right)^2 + \frac{1}{6} \sum_{i=1}^2 \left(d\theta_i^2 + \sin^2 \theta_i d\phi_i^2 \right). \quad (2.3)$$

The coordinate ranges are $\theta_i \in [0, \pi]$, $\phi_i \in [0, 2\pi]$ and $\psi \in [0, 4\pi]$. The warp factor A can be computed explicitly for the unperturbed conifold, but is not required for the inflationary analysis.

If the branes are exactly parallel, their displacement is uniquely labelled by the coordinate r . It runs from a minimum value r_{IR} , where the geometry is ‘deformed’ by attaching to a smooth cap that resolves the singularity at the tip of the cone [70], and extends in principle to arbitrarily large r . However, we usually imagine that the Klebanov–Strassler solution is cut off at some large value r_{UV} and glued to a compact bulk space.⁵ In the field theory dual, small values of r correspond to the infrared and large values correspond to the ultraviolet. The $\overline{\text{D3}}$ -brane is located in the infrared, where the warp factor minimizes its energy, and the mobile D3-brane is drawn from the ultraviolet towards the infrared end of the cone. Inflation ends when the mobile brane becomes sufficiently close to the $\overline{\text{D3}}$ that a tachyonic instability develops and the brane pair dissolves into closed string modes. In the four-dimensional field theory description this is a hybrid transition in which the inflaton is destabilized by a waterfall field. See Fig. 1.

Kinetic and potential terms for the brane.—The dynamics of the mobile D3-brane are determined by the action

$$S = -T_3 \int d^4x \sqrt{-\det \gamma_{ab}} + T_3 \int d^4x \sqrt{-g} \alpha, \quad (2.4)$$

where x^a label coordinates on the brane and γ_{ab} is its induced metric. There are two contributions. The first is the Nambu–Goto action. This computes the total energy of the brane, given by its tension T_3 integrated over its worldvolume. The second is a Chern–Simons term that couples the brane worldvolume to a four-form potential $C_4 = \alpha\omega$, where $\omega = \star(1)$ is the volume form determined by g_{ab} .

⁴For a description of coordinates on $T^{1,1}$, see Refs. [50, 51, 69–72]. We follow Candelas & de la Ossa [70], especially §2 and Appendix A. $SU(2)$ is isomorphic to the three-sphere S^3 , which itself is a Hopf fibration of $U(1)$ over S^2 . The $U(1)$ can be regarded as parametrizing motion along a great circle of S^3 . In the product $SU(2) \times SU(2)$ there are two $U(1)$ fibres corresponding to motion along great circles of the left and right S^3 s. We define the linear combinations $H = T_3 + \hat{T}_3$ and $K = T_3 - \hat{T}_3$, where the T_i are generators of the left-hand copy of $SU(2)$ and \hat{T}_i are corresponding generators of the right-hand copy, and T_3, \hat{T}_3 generate the $U(1)$ factors.

$T^{1,1}$ is the quotient $SU(2) \times SU(2)/U(1)_H$, obtained by identifying points that can be reached by a rotation generated by H . (It is part of a family of spaces $T^{p,q}$ obtained by generalizing H to $H = pT_3 + q\hat{T}_3$. To preserve supersymmetry we must choose $p = q = 1$ [69].) Therefore, in local Euler angles $\vartheta, \hat{\vartheta}$ measured along each great circle, $T^{1,1}$ can be embedded as any hypersurface $\vartheta + \hat{\vartheta} = \text{const}$ [49]. The coset representatives are labelled by the angular coordinate along this hypersurface. Accordingly, functions on $T^{1,1}$ should depend only on the coset label $\vartheta - \hat{\vartheta}$ and not $\vartheta + \hat{\vartheta}$.

⁵The six extra dimensions must be compactified, unlike the Klebanov–Strassler solution, otherwise the effective Planck mass would be ∞ and there would be no dynamical gravity induced in the four-dimensional world.

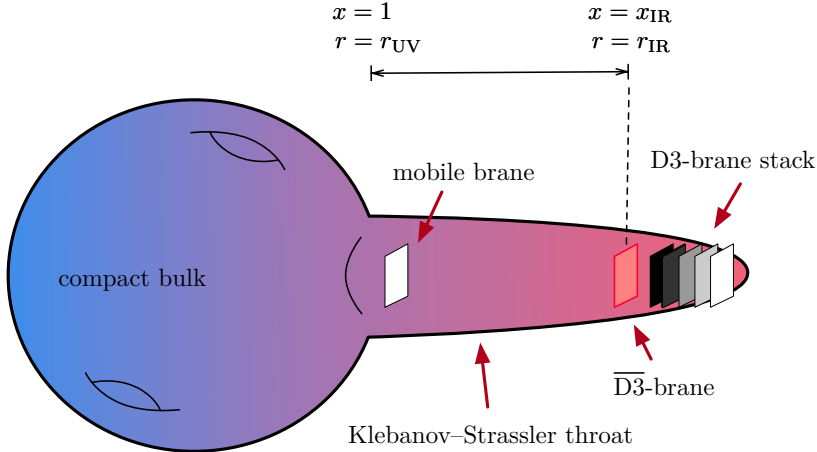


Figure 1. Schematic representation of the extradimensional geometry. The throat is supported by a stack of D3-branes placed at its tip and is approximately described by the Klebanov–Strassler solution. It attaches in the ultraviolet ($x = 1, r = r_{UV}$) to an unknown bulk manifold. In the infrared ($r = r_{IR}$) a $\overline{D3}$ -brane draws the mobile brane down the throat due to their mutual Coulomb attraction.

We now drop the parallel approximation. Assuming the brane is embedded in the transverse dimensions at $X^A = X^A(x^a)$, it follows that

$$\gamma_{ab} = e^{2A} g_{ab} + e^{-2A} G_{AB} \partial_a X^A \partial_b X^B, \quad (2.5)$$

where G_{AB} is the metric on the cone, Eq. (2.2). Therefore,

$$S = -T_3 \int d^4x \sqrt{-g} e^{4A} \sqrt{\det \left(\delta_c^a + e^{-4A} G_{AB} g^{ab} \partial_b X^A \partial_c X^B \right)} + T_3 \int d^4x \sqrt{-g} \alpha. \quad (2.6)$$

Assuming the brane is moving non-relativistically it suffices to work only up to quadratic order in derivatives. The zeroth order term from the determinant combines with the Chern–Simons term to generate a potential,

$$V = T_3 \equiv T_3 \Phi_-, \quad \text{where} \quad \Phi_- \equiv e^{4A} - \alpha. \quad (2.7)$$

If the Klebanov–Strassler geometry is unperturbed—meaning that the infrared $\overline{D3}$ -brane is absent—then $A = A(r)$ and $\alpha = \alpha(r)$ depend only on the radial coordinate. Therefore $V = V(r)$ also depends only on r , and the angles $\{\theta_1, \theta_2, \phi_1, \phi_2, \psi\}$ are flat directions. However, more careful analysis shows that in this case $\alpha = e^{4A}$ and the potential vanishes [73]. Generically, both A and α will depend on r and the angles. This lifts the flat directions. Notice that the potential depends on the warp factor, which produces the flattening observed in Refs. [39, 40].

At second order in derivatives we obtain

$$S = -\frac{T_3}{2} \int d^4x \sqrt{-g} G_{AB} \partial^a X^A \partial_a X^B, \quad (2.8)$$

in which the warp factor has cancelled. Eq. (2.8) is the kinetic term for a set of noncanonical four-dimensional scalar fields X^A with kinetic mixing matrix G_{AB} inherited from the

cone (2.2). Therefore, if the potential can be chosen suitably, the ϕ^A may support a phase of slow-roll inflation. Predictions from inflationary models of this type were studied by Sasaki & Stewart [74]. The theory was developed up to three-point observables by a number of authors [6, 23, 75–80].

Instead of r we choose to work in terms of the coordinate $x = r/r_{\text{UV}}$ introduced in Ref. [52]. Its range is $x_{\text{IR}} < x \ll 1$, where $x_{\text{IR}} \equiv r_{\text{IR}}/r_{\text{UV}}$. The throat attaches to the compact bulk space in the region $x \sim 1$. Further, if we simplify the brane kinetic term by absorbing the tension T_3 into the metric, we find

$$G_{AB} dX^A dX^B \rightarrow r_{\text{UV}}^2 T_3 (dx^2 + x^2 ds_{T^{1,1}}^2) \equiv \phi_{\text{UV}}^2 (dx^2 + x^2 ds_{T^{1,1}}^2), \quad (2.9)$$

where we have defined $\phi_{\text{UV}} = r_{\text{UV}} T_3^{1/2}$. Note that the fields $\{x, \theta_1, \theta_2, \phi_1, \phi_2, \psi\}$ appearing in the four-dimensional effective action all have engineering dimension zero. To compensate, the metric G_{AB} has engineering dimensions of $[\phi_{\text{UV}}^2] = [\text{M}^2]$.

Field range.—Baumann & McAllister argued that in a throat carrying D3-brane charge $Z \gg 1$, the field range would be bounded by $\phi_{\text{UV}} < 2M_{\text{P}}/Z^{1/2}$ [67]. Following Agarwal et al. [52] we generally take $\phi_{\text{UV}} = 10^{-1}$ and fix $T_3 = 10^{-2} M_{\text{P}}^4$. In §4.3 we briefly look at the effect of varying the field-range bound over the interval $10^{-1} < \phi_{\text{UV}} < 10^{-3}$.

2.2 The D3-brane potential

The remaining task is to enumerate permitted contributions to the D3-brane potential, Eq. (2.7). In the unperturbed Klebanov–Strassler geometry (without the infrared $\overline{\text{D3}}$ -brane) both $A = A(r)$ and $\alpha = \alpha(r)$ can be calculated explicitly [73], but as explained above this leads to a vanishing potential. The interpretation is that gravitational attraction between the mobile D3-brane and the D3-brane stack at the tip is balanced by repulsion due to their same-sign charges. This arrangement cannot support an inflationary epoch. To generate a nontrivial potential requires additional sources, so that we no longer expect exact cancellation.

How are we to determine the possible contributions? The general formula $V = T_3 \Phi_-$ given in (2.7) continues to apply, which reduces the problem to determination of Φ_- . The supergravity field equations in the throat can be shown to require

$$\nabla^2 \Phi_- = R_4 + \frac{g_s}{96} |\Lambda|^2 + e^{-4A} |\nabla \Phi_-|^2 + \text{local terms}, \quad (2.10)$$

where g_s is the string coupling, ∇^2 is the Laplacian on the conifold (2.2), and R_4 is the four-dimensional Ricci scalar. Λ is a 3-form flux that depends on the 3-form field G_3 of type IIB supergravity; for details, see Refs. [2, 46, 48]. The ‘local terms’ represent localized contributions from the mobile brane and the $\overline{\text{D3}}$ -brane, which we now introduce.

Coulomb and mass terms.—First, the local terms generate a Coulomb attraction between the mobile brane and the antibrane, with potential

$$V_{\mathcal{C}}(x) = D_0 \left(1 - \frac{27}{64\pi^2} \frac{D_0}{\phi_{\text{UV}}^4} \frac{1}{x^4} \right). \quad (2.11)$$

The parameter D_0 is defined by $D_0 \equiv 2T_3 a_0^4$ [46], where $a_0 \equiv e^{A(r_{\text{IR}})} \ll 1$. It is the smallness of D_0 , caused by warping of the conifold, that makes the potential sufficiently flat to inflate at modest values of x .

Second, the leading effect of the Ricci term R_4 is to generate the operator $R_4 \phi_{\text{UV}}^2 x^2 / 12$. During inflation the background geometry is approximately de Sitter, for which $R_4 = 12H^2$. If we take the inflationary phase to be supported by the constant term in (2.11), possibly augmented by a second uplift V_0 , then $3H^2 M_{\text{P}}^2 \approx V_0 + D_0$. Here V_0 accounts for constant contributions that do not originate in the Coulomb interaction, which could include distant sources of supersymmetry breaking. In total this yields a mass term for x of the form

$$V_{\mathcal{M}} = \mu^4 x^2 / 3, \quad (2.12)$$

where we have defined [52]

$$\mu^4 \equiv (V_0 + D_0) \left(\frac{\phi_{\text{UV}}}{M_{\text{P}}} \right)^2. \quad (2.13)$$

Note that μ has mass dimension [M].

Deformations of the throat.—Third, the throat geometry (2.2) may be disturbed because of back-reaction from the passage of the brane. It may also be deformed by the suture between the throat and the compact bulk geometry. Any such disturbances will affect the dynamics of the brane and contribute to its effective potential.

In the vicinity of the suture an adequate description of Φ_- will require boundary conditions that determine how information from the compact bulk is communicated to the ultraviolet end of the throat. This complicated structure for Φ_- will generate a large number of operators in the effective theory whose Wilson coefficients depend sensitively on the ultraviolet data. In this region there is little hope of performing a realistic analysis of the model.

On the other hand, in the infrared region $x \ll 1$ we expect that renormalization group running will suppress most of these operators, leaving only a handful of the most relevant terms. In this region fewer Wilson coefficients must be specified, making the model significantly simpler to analyse. In particular, as described in §1, we can parametrize our ignorance of the ultraviolet boundary data by drawing these unknown Wilson coefficients from one or more suitable statistical distributions.

Any deformation of the throat must satisfy (2.10). We work to leading order in perturbations. (For details of the approximation scheme being used we refer to the original literature [48].) The local terms and Ricci scalar generate only the additive contributions described above.⁶ The equation to be solved is therefore

$$\nabla_0^2 \Phi_- = \frac{g_s}{96} |\Lambda|^2, \quad (2.14)$$

where ∇_0^2 is the unperturbed conifold Laplacian. Notice that to solve (2.14) we do not need to know the behaviour of the remaining supergravity fields except for the dilaton that determines

⁶This is not true in general. As explained in Ref. [48], the effect of the Ricci term is to dress each term in the potential with higher powers of x . However, we will truncate the brane potential before the first of these

g_s . Its general solution consists of a particular integral (or ‘flux term’) $\Phi_{\mathcal{F}}$ supported by the source term $g_s|\Lambda|^2/96$ plus a complementary function (or ‘homogeneous term’) $\Phi_{\mathcal{H}}$ that satisfies the homogeneous equation. The complete potential is therefore

$$V = V_{\mathcal{C}} + V_{\mathcal{M}} + V_{\mathcal{H}} + V_{\mathcal{F}}, \quad (2.15)$$

where $V_{\mathcal{H}}$ and $V_{\mathcal{F}}$ are the potential terms generated by $\Phi_{\mathcal{H}}$ and $\Phi_{\mathcal{F}}$, respectively. We describe their construction in §§2.3–2.4 below.

2.3 Harmonic analysis on the conifold

The Peter–Weyl theorem.—Both $V_{\mathcal{H}}$ and $V_{\mathcal{F}}$ can be analysed using the methods of harmonic analysis on Lie groups. According to the Peter–Weyl theorem, an orthonormal basis for square-integrable functions on a compact Lie group G is furnished by the matrix coefficients $D_{mm'}^{(\mu)}$, summed over all unitary irreducible representations (μ) [81]. These are defined to satisfy

$$D_{mm'}^{(\mu)}(g) \equiv \langle m | \rho(g) | m' \rangle, \quad (2.16)$$

where $|m\rangle$ labels a basis for the representation (μ) and ρ is its representation map.

Specifically, for a square-integrable function Φ and $g \in G$, the Peter–Weyl theorem guarantees that Φ can be represented as the sum

$$\Phi(g) = \sum_{(\mu)} \sum_{mm'} c_{mm'}^{(\mu)} D_{mm'}^{(\mu)}(g), \quad (2.17a)$$

where $c_{mm'}^{(\mu)}$ are coefficients depending on Φ . Hence, the $D_{mm'}^{(\mu)}$ function as harmonics of G in a sense analogous to Fourier analysis. Observe that each representation occurs in (2.17a) with multiplicity equal to its dimension. Although we will not need this refinement, if Φ transforms in an irreducible higher-dimensional representation (ν) of G , in the sense

$$\Phi_m^{(\nu)}(g' \cdot g) = \sum_{m'} D_{mm'}^{(\nu)}(g') \Phi_{m'}^{(\nu)}(g), \quad (2.17b)$$

then the expansion (2.17a) is shortened and only the (ν) representation is present, with multiplicity one. For further details see Salam & Strathdee [82], who explained the application of (2.17a) to the typical case where Φ is a supergravity field transforming in some nontrivial representation of the tangent space $SO(1,3)$ symmetry.

Our interest lies in the case where Φ is a spacetime scalar and G is the coset $T^{1,1} = SU(2) \times SU(2)/U(1)$ described above. In this situation (2.17a) continues to apply, with

$$\Phi[L(g)] = \sum_{(\mu)} \sum_{mm'} c_{mm'}^{(\mu)} D_{mm'}^{(\mu)}[L(g)], \quad (2.17c)$$

where $L(g)$ is the coset representative of g .

dressed terms appears. See the discussion on p. 22. Therefore, for our analysis, it suffices to add the Coulomb term and mass term to the potential obtained from Eq. (2.14).

Application to $T^{1,1}$.—The unitary irreducible representations of $SU(2)$ are labelled by their spin ℓ . The corresponding matrix coefficients are given by Wigner’s *Darmstellung* or D -matrix,

$$D_{mm'}^\ell(\phi, \theta, \vartheta) \equiv \langle \ell m | e^{-i\phi T_z} e^{-i\theta T_y} e^{-i\vartheta T_z} | \ell m' \rangle, \quad (2.18)$$

where the T_i are generators of $SU(2)$, $\{\theta, \phi, \vartheta\}$ are corresponding Euler angles, and $-\ell \leq m, m' \leq \ell$. Representations of $SU(2) \times SU(2)$ are built from the tensor product of a pair of representations of spin ℓ_1, ℓ_2 associated with the left- and right-hand $SU(2)$ factors. We distinguish these factors using the labels $i = 1, 2$, respectively. It follows that the corresponding harmonics are

$$\mathcal{E}_{m_1, n_1, m_2, n_2}^{\ell_1, \ell_2}(\theta_1, \phi_1, \vartheta_1; \theta_2, \phi_2, \vartheta_2) \equiv \mathcal{N} D_{m_1, n_1}^{\ell_1}(\phi_1, \theta_1, \vartheta_1) D_{m_2, n_2}^{\ell_2}(\phi_2, \theta_2, \vartheta_2) \quad (2.19)$$

where the quantum numbers ℓ_i, m_i, n_i satisfy the usual constraints for representations of $SU(2)$. The prefactor \mathcal{N} is a normalization to be determined.

In terms of these Euler angles, $T^{1,1}$ can be embedded in $SU(2) \times SU(2)$ as a hypersurface Σ satisfying $\vartheta_1 + \vartheta_2 = \text{const.}$ (See the discussion in footnote 4 on p. 14, and the explicit discussion given by Gubser [49].) Eq. (2.17c) shows that the harmonics on $T^{1,1}$ follow from (2.19) by restriction to suitable coset representatives, and therefore we must project out dependence on $\vartheta_1 + \vartheta_2$. The representatives are labelled by $\psi = (\vartheta_1 - \vartheta_2)/2$, where $0 \leq \psi < 4\pi$. To obtain the correct projection, note that the Wigner D -matrix can be expressed in terms of the ‘little’ d -matrix, defined by

$$D_{mn}^\ell(\phi, \theta, \vartheta) \equiv e^{-im\phi} d_{mn}^\ell(\theta) e^{-in\vartheta}. \quad (2.20)$$

Therefore we must choose $n_1 = -n_2$. Note that $d_{mn}^\ell(\theta)$ is real.

We write $n_1 = -n_2 = R/2$. After making a parity inversion on the $i = 2$ sphere, the metric on Σ can be brought to the canonical form (2.3). Using the transformation rule $d_{-m, -n}^\ell(\theta) = d_{mn}^\ell(-\theta)$ we find that the harmonics can be written⁷

$$\mathcal{E}_{m_1, m_2, R/2}^{\ell_1, \ell_2}(\theta_1, \phi_1, \theta_2, \phi_2, \psi) = \mathcal{N}' \exp\left(\frac{R}{2}\psi + \sum_i m_i \phi_i\right) d_{m_1, R/2}^{\ell_1}(\theta_1) d_{m_2, R/2}^{\ell_2}(\theta_2), \quad (2.21)$$

where \mathcal{N}' is an adjusted normalization. To repeat, the properties of the quantum numbers follow from the selection rules for representations of $SU(2)$, viz.,

- ℓ_1 and ℓ_2 are nonnegative and *either* both integers *or* both half-integers;
- $m_1 \in \{-\ell_1, \dots, \ell_1\}$ and $m_2 \in \{-\ell_2, \dots, \ell_2\}$; and
- $R/2 \in \{-l, \dots, l\}$ where $l = \min(\ell_1, \ell_2)$.

This analysis clearly exhibits the Lie group structure underlying the harmonics. For practical calculations, however, we require explicit formulae for the \mathcal{E}_{LM} . Here we borrow

⁷Ceresole et al. define a ‘scalar harmonic condition’, which in our language can be written $m_1 = R/2$, $m_2 = -R/2$ [50, 51]. Harmonics satisfying this conditions depend only on $\Delta\phi = \phi_1 - \phi_2$, and not ϕ_1 or ϕ_2 separately. They are ‘scalar’ in the sense that they are uncharged under the $U(1)_H$ divisor of $T^{1,1}$. Notice, however, that this condition is immaterial for the expansion of a typical *spacetime* scalar such as (2.17a), which

the economical notation of Baumann et al. [43] in which the harmonics are distinguished by multi-indices $L = (\ell_1, \ell_2, R)$ and $M = (m_1, m_2)$. Specifically L labels the representation of the harmonic under the isometry group $SU(2) \times SU(2) \times U(1)$, and M runs over the corresponding representation space.

Explicit formulae.—Explicit formulae for the \mathcal{E}_{LM} were obtained by Gubser using a direct analysis of their governing differential equations [49]. Later, a more extensive discussion was given by Ceresole et al. [50, 51, 83], who used algebraic methods based on group theory [82]. The details were summarized by Baumann et al. [43]. Expressions for the zero-modes on the conifold were given in Ref. [48]; see also Ref. [84]. The expression (2.21) in terms of the little d -matrix was first given in Ref. [85].⁸ Here we briefly collect these details in a unified notation.

The \mathcal{E}_{LM} are eigenfunctions of the Laplacian on $T^{1,1}$ with eigenvalue Λ_L ,

$$\nabla_{T^{1,1}}^2 \mathcal{E}_{LM}(\Psi) = -\Lambda_L \mathcal{E}_{LM}(\Psi). \quad (2.22)$$

The eigenvalue spectrum depends on a sum of quadratic Casimir invariants for the representations specified by L , but not the representation-space labels M . It satisfies

$$\Lambda_L = 6 \left(\ell_1(\ell_1 + 1) + \ell_2(\ell_2 + 1) - \frac{R^2}{8} \right). \quad (2.23)$$

The necessary nonsingular solutions for $d_{m,R/2}^\ell(\theta)$ are⁹

$$\begin{aligned} \left(\frac{2\ell + 1}{2} \right)^{1/2} d_{m,R/2}^\ell(\theta) &= J_{\ell,m,R}^\Upsilon \\ &\equiv N_{LM}^\Upsilon (\sin \theta)^m \left(\cot \frac{\theta}{2} \right)^{\frac{R}{2}} {}_2F_1 \left(\begin{matrix} -\ell + m, 1 + \ell + m \\ 1 + m - R/2 \end{matrix} \middle| \sin^2 \frac{\theta}{2} \right), \end{aligned} \quad (2.24a)$$

if $m \geq R/2$, and

$$\begin{aligned} \left(\frac{2\ell + 1}{2} \right)^{1/2} d_{m,R/2}^\ell(\theta) &= J_{\ell,m,R}^\Omega \\ &\equiv N_{LM}^\Omega (\sin \theta)^{\frac{R}{2}} \left(\cot \frac{\theta}{2} \right)^m {}_2F_1 \left(\begin{matrix} -\ell + R/2, 1 + \ell + R/2 \\ 1 - m + R/2 \end{matrix} \middle| \sin^2 \frac{\theta}{2} \right), \end{aligned} \quad (2.24b)$$

if $m < R/2$. As explained above, both solutions are real. Here, ${}_2F_1(a, b; c | z)$ is the Gauss hypergeometric function, and we have introduced mode functions $J_{\ell,m,R}(\theta)$ to match the

contains representations of all dimensions, not just ‘scalar’ representations in the sense of Ceresole et al.

⁸Explicit formulae for the d_{mn}^ℓ were given by Wigner [86]. Their generating function was computed by Schwinger [87]. The connexion between harmonics on $T^{1,1}$ and Wigner’s little d -matrix was apparently not noticed prior to Ref. [85].

⁹These formulae match those quoted in Ref. [49]. The four cases given there can be related in pairs using an Euler transformation of the hypergeometric function.

notation of Ref. [43]. It follows from a Sturm–Liouville argument that the $J_{\ell,m,R}(\theta)$ are orthogonal for fixed m, R in the measure $\sin \theta d\theta$. Their normalization is fixed by adjusting $N_{LM}^\Upsilon, N_{LM}^\Omega$ so that

$$\int_0^\pi d\theta \sin \theta J_{\ell,m,R}(\theta) J_{\ell',m,R}(\theta) = \delta_{\ell\ell'}. \quad (2.25)$$

If we choose the normalization of the \mathcal{E}_{LM} so that

$$\mathcal{E}_{LM}(\Psi) = J_{\ell_1,m_1,R}(\theta_1) J_{\ell_2,m_2,R}(\theta_2) \exp i\left(m_1\phi_1 + m_2\phi_2 + \frac{R}{2}\psi\right), \quad (2.26)$$

then the \mathcal{E}_{LM} satisfy the larger orthogonality condition

$$\int d^5\Psi (-\det G_{T^{1,1}})^{1/2} \mathcal{E}_{LM}(\Psi) \mathcal{E}_{L'M'}^*(\Psi) = \delta_{LL'} \delta_{MM'}, \quad (2.27)$$

where Ψ stands schematically for the five angles on $T^{1,1}$, and $G_{T^{1,1}}$ is its metric.

Zero-modes on the conifold.—Each $T^{1,1}$ harmonic can be promoted to a zero-mode of the conifold—that is, a solution of the homogeneous equation $\nabla_0^2 \Phi_- = 0$. A simple calculation shows that if \mathcal{E}_{LM} is a harmonic on $T^{1,1}$ with eigenvalue Λ_L , then [43]

$$f_{LM}(r, \Psi) = r^{\Delta(L)} \mathcal{E}_{LM}(\Psi) \quad (2.28)$$

is a zero-mode of ∇_0^2 , where

$$\Delta(L) \equiv -2 \pm \sqrt{4 + \Lambda_L}. \quad (2.29)$$

Therefore the complementary function for Φ_- can be expressed as a linear combination of these zero-modes. It will make a contribution to the brane potential of the form

$$V_{\mathcal{H}}(x, \Psi) = \mu^4 \sum_{LM} C_{LM} x^{\Delta(L)} \mathcal{E}_{LM}(\Psi) + \text{c.c.}, \quad (2.30)$$

where the scale μ^4 , defined in Eq. (2.13), has been inserted by hand to account for the factor of the tension T_3 appearing in the dictionary between Φ_- and the brane potential V . The C_{LM} are taken to be unknown (complex) Wilson coefficients, and $\Delta(L)$ determines the radial scaling of each operator. In the region $|x| \ll 1$, away from the ultraviolet end of the throat, only a few operators of lowest scaling dimension will be relevant, as anticipated in the discussion above Eq. (2.14).

Although we would like to keep as many operators as possible, there are practical limitations. As we increase the number of terms that are retained, we incur corresponding costs from the automated symbolic manipulations carried out by the **CppTransport** and **PyTransport** platforms, and also in the numerical solution of the transport equations. We will see that it is already challenging to solve for the three-point function in a model of this complexity, so it is not realistic to attempt to retain operators of very high order. On the other hand, at a minimum, we would like to retain operators that contribute significantly to the effective cubic couplings. If these are large (as suggested by the parametric estimates given in Ref. [59]) they potentially source a large bispectrum from the quasi-single-field ‘QSFI’ mechanism [60–62, 88]. It follows that aggressive truncation of the potential risks serious misprediction for a key observable of the model.

Table 3. Scalar zero-modes of the conifold Laplacian ∇_0^2 . Tabulated values are the radial scaling dimension $\Delta(L)$; $SU(2) \times SU(2)$ representation labels (ℓ_1, ℓ_2) ; the $U(1)$ representation label R ; the mode normalization constant for $J_{\ell,m,R}(\theta)$; and the dimension of the representation. We limit inclusion to modes with lowest-lying radial scaling dimensions $\Delta(L) \leq 3.8$. This gives a total of 73 different modes, all of which occur with fixed multiplicities as described in §2.3.

$\Delta(L)$	decimal scaling	ℓ_1	ℓ_2	R	normalization $\times \pi^{3/2}$	dimension
3/2	1.5	1/2	1/2	-1	$3\sqrt{3}/2$	4
3/2	1.5	1/2	1/2	1	$3\sqrt{3}/4$	4
2	2.0	1	0	0	9/4	3
2	2.0	0	1	0	9/4	3
3	3.0	1	1	2	$9\sqrt{3}/16$	9
3	3.0	1	1	-2	$9\sqrt{3}/4$	9
$2\sqrt{7} - 2$	3.2915	1	1	0	$9\sqrt{3}/4$	9
7/2	3.5	1/2	3/2	-1	$3\sqrt{6}/4$	8
7/2	3.5	1/2	3/2	1	$3\sqrt{6}/2$	8
7/2	3.5	3/2	1/2	-1	$3\sqrt{6}/2$	8
7/2	3.5	3/2	1/2	1	$3\sqrt{6}/4$	8
						73

In Table 3 we tabulate the lowest-lying zero modes of ∇_0^2 with radial scaling dimensions that satisfy $\Delta(L) \leq \Delta_{\max} = 3.8$. (This choice was made by Agarwal et al. and Dias et al. [9, 52]. McAllister et al. [85] did not give their truncation explicitly, but apparently used the same prescription.) We use this truncation in §3 to construct our primary statistical ensemble, giving sufficient headroom to capture large QSFI effects. At this level there are eleven contributing representations $L = (\ell_1, \ell_2, R)$. However, it should be remembered that the number of *modes* is rather larger because the dimension of these representations lies between 3 (for $\ell_1 = 1, \ell_2 = 0$ and vice-versa) and 9 (for $\ell_1 = \ell_2 = 1$), and as explained in §2.3 each representation contributes with multiplicity equal to its dimension. There is a unique constant mode with $\ell_1 = \ell_2 = R = 0$ that we omit; it is proportional to the unit operator and merely renormalizes the vacuum energy. Therefore its effect can be absorbed into V_0 . (However, see Table 6.)

Reality properties of the zero-modes.—Because the ‘little’ d -matrices (or equivalently, the J mode functions) are real, complex conjugation simply reverses the sign of the labels R , m_1 and m_2 . This follows from Eqs. (2.24a)–(2.24b) after making an Euler transformation of the hypergeometric function. Therefore modes with $R < 0$ in Table 3 are related to those with $R > 0$ by complex conjugation. A special case of this observation is that modes with

$R = m_1 = m_2 = 0$ are purely real.

In the interest of clarity, we note that the sum in (2.30) is unrestricted and includes representations with both signs of R . Moreover, the coefficients C_{LM} are taken to be independent for each set of quantum numbers L, M . First, consider a complex mode \mathcal{E}_{LM} for which at least one of the labels R, m_1 and m_2 is nonzero. For convenience we define $-L = (\ell_1, \ell_2, -R)$ and $-M = (-m_1, -m_2)$. The contribution of \mathcal{E}_{LM} to $V_{\mathcal{H}}$ can be written as a sum of \mathcal{E}_{LM} and \mathcal{E}_{-L-M} ,

$$V_{\mathcal{H}} \supseteq \mu^4 x^{\Delta(L)} \left(C_{LM} \mathcal{E}_{LM} + C_{LM}^* \mathcal{E}_{LM}^* \right) = \mu^4 x^{\Delta(L)} \left(C_{LM} \mathcal{E}_{LM} + C_{LM}^* \mathcal{E}_{-L-M} \right), \quad (2.31)$$

where the notation \supseteq denotes that $V_{\mathcal{H}}$ contains the indicated contribution, together with other contributions that have not been written. Meanwhile a similar relation holds for \mathcal{E}_{-L-M} . In combination they yield

$$V_{\mathcal{H}} \supseteq 2\mu^4 x^{\Delta(L)} \operatorname{Re} \left(D_{LM} \mathcal{E}_{LM} \right) = 2\mu^4 x^{\Delta(L)} \left(\operatorname{Re}(D_{LM}) \operatorname{Re}(\mathcal{E}_{LM}) - \operatorname{Im}(D_{LM}) \operatorname{Im}(\mathcal{E}_{LM}) \right), \quad (2.32)$$

where $D_{LM} \equiv C_{LM} + C_{-L-M}^*$. It follows that we can equivalently restrict the sum in (2.30) to $L = (\ell_1, \ell_2, R)$ with $R > 0$ provided we adjust the summand to match (2.32). Later we will take the real and imaginary parts of C_{LM} to be random variables drawn from some distribution X . It is important to note that the real and imaginary parts of D_{LM} should then be drawn from the appropriate distributions for the sum and difference of two X -distributed random variables, respectively.

Second, consider a real mode with $R = m_1 = m_2 = 0$. This depends only on (at least one of) θ_1, θ_2 , unless $\ell_1 = \ell_2 = 0$. In this case it is a constant and is excluded from the sum as described above. Therefore the contribution from this mode to $V_{\mathcal{H}}$ is

$$V_{\mathcal{H}} \supseteq 2\mu^4 x^{\Delta(L)} C_{LM} \mathcal{E}_{LM} \quad (2.33)$$

where now C_{LM} is real with numerical value drawn from the distribution X .

2.4 Flux contributions

The final step is to include the ‘particular integral’ for (2.14)—that is, the perturbation to Φ_- sourced by the square of the 3-form flux $|\Lambda|^2$. The allowed contributions to Λ were enumerated by Baumann et al. [48] and fall into three distinct ‘series’, distinguished by the recipe for building the 3-form Λ from a seed zero-mode drawn from Table 3. Depending on the details of the recipe, the resulting fluxes may exhibit an adjusted radial scaling dimension Δ or an adjusted $U(1)$ quantum number R . We will not require explicit formulae for the fluxes, and therefore refer to the literature for details of their construction.

Flux contributions to Φ_- .—In Tables 4–6 we tabulate the required seed representations, and adjusted radial scaling dimensions, associated with these flux series, labelled Series I, II and III in the notation of Baumann et al. [48]. We limit attention to representations for which the adjusted scaling dimension Δ satisfies $2 < \Delta \leq 5.8$. At the upper limit, we will see later that fluxes with $\Delta \leq 5.8$ are sufficient to capture all contributions to Φ_- with radial scaling

Table 4. Series I fluxes. Tabulated values are the adjusted radial scaling dimension $\Delta = 1 + \Delta_f$, where f is the scalar seed mode; the $SU(2) \times SU(2) \times U(1)$ quantum numbers ℓ_1, ℓ_2, R for f ; dimension of the representation; and whether the flux is chiral, defined to mean $\ell_1 = \ell_2 = R/2$ for the seed mode. We include the 109 modes with radial scaling dimensions that satisfy $2 < \Delta \leq 5.8$.

Δ	decimal scaling	ℓ_1	ℓ_2	R	dimension	type
5/2	2.5	1/2	1/2	-1	4	non-chiral
5/2	2.5	1/2	1/2	1	4	chiral
4^a	4.0	1	1	-2	9	non-chiral
4	4.0	1	1	2	9	chiral
$\sqrt{28} - 1$	4.2915	1	1	0	9	non-chiral
9/2	4.5	1/2	3/2	-1	8	non-chiral
9/2	4.5	1/2	3/2	1	8	non-chiral
9/2	4.5	3/2	1/2	-1	8	non-chiral
9/2	4.5	3/2	1/2	1	8	non-chiral
$2\sqrt{10} - 1$	5.3246	2	0	0	5	non-chiral
$2\sqrt{10} - 1$	5.3246	0	2	0	5	non-chiral
11/2	5.5	3/2	3/2	-3	16	non-chiral
11/2	5.5	3/2	3/2	3	16	chiral
109						

^a The representations with $(\ell_1, \ell_2, R) = (1, 0, 0), (0, 1, 0)$ are absent, even though they appear in Table 3. These modes were excluded by Baumann et al. [48] without comment, apparently because they are projected out of the spectrum by the field equation for G_3 . These seed modes *do* appear for the Series II and Series III fluxes listed in Tables 5 and 6. In Ref. [9] they were accidentally excluded from Series II and III. In principle this could influence outcomes from the model, but see footnote 11 on p. 28. We would like to thank Mafalda Dias for very helpful correspondence on these issues.

dimension $\delta \leq \Delta_{\max} = 3.8$. Notice that in this section we carefully distinguish the adjusted radial scaling dimension Δ of the fluxes, and the dimension δ of the contribution that is ultimately produced in the potential. At the lower limit, fluxes with $\Delta \leq 2$ do not couple to a probe D3 brane [48] and can be discarded. When summed over all three series there are 197 flux modes. Clearly the resulting D3-brane potential is very complicated.

The possible contributions to $|\Lambda|^2$ involve combinations of any two fluxes drawn from Tables 4–6, with the proviso that two chiral modes can combine only if they belong to the same flux series [48]. A flux mode is said to be chiral if and only if its seed scalar mode is chiral in the sense $\ell_1 = \ell_2 = R/2$ [48].

The contribution to Φ_- from any pair of fluxes can be found using the method of Green’s

Table 5. Series II fluxes. Tabulated values are the adjusted radial scaling dimension $\Delta = 2 + \Delta_f$, where f is the scalar seed mode; the $SU(2) \times SU(2) \times U(1)$ quantum numbers ℓ_1, ℓ_2, R for f ; dimension of the representation; and whether the flux is chiral, defined to mean $\ell_1 = \ell_2 = R/2$ for the seed mode. We include the 73 modes with radial scaling dimensions that satisfy $2 < \Delta \leq 5.8$.

Δ	decimal scaling	ℓ_1	ℓ_2	R	dimension	type
7/2	3.5	1/2	1/2	-1	4	non-chiral
7/2	3.5	1/2	1/2	1	4	chiral
4	4.0	0	1	0	3	non-chiral
4	4.0	1	0	0	3	non-chiral
5	5.0	1	1	-2	9	non-chiral
5	5.0	1	1	2	9	chiral
$2\sqrt{7}$	5.2915	1	1	0	9	non-chiral
11/2	5.5	1/2	3/2	-1	8	non-chiral
11/2	5.5	1/2	3/2	1	8	non-chiral
11/2	5.5	3/2	1/2	-1	8	non-chiral
11/2	5.5	3/2	1/2	1	8	non-chiral
73						

functions. Specifically,

$$\Phi_{-}(x) = \frac{g_s}{96} \int d^6 y \, (-\det G_{AB})^{1/2} \mathfrak{Gr}(x, y) |\Lambda(y)|^2, \quad (2.34)$$

where G_{AB} is the metric (2.2) on the conifold and $\mathfrak{Gr}(x, y)$ is the corresponding Green's function obtained in Ref. [43]. It has the spectral representation

$$\mathfrak{Gr}(x, x') = \sum_{LM} \mathcal{E}_{LM}(\Psi) \mathcal{E}_{LM}^*(\Psi') g_L(r, r'), \quad (2.35)$$

where $x = (r, \Psi)$, $x' = (r', \Psi')$ are coordinates on the conifold, and Ψ, Ψ' represent the angles on $T^{1,1}$. The kernel $g_L(r, r')$ satisfies [43]

$$g_L(r, r') = -\frac{1}{2\Delta(L) + 1} \begin{cases} (r')^{-4} (r/r')^{\Delta(L)} & r_{\text{IR}} \lesssim r \leq r' \\ r^{-4} (r'/r)^{\Delta(L)} & r' \leq r \lesssim r_{\text{UV}} \end{cases}. \quad (2.36)$$

As explained above, some of the fluxes listed in Tables 4–6 have modified quantum numbers because they combine with other ingredients. For example (now passing to a Kähler description), some flux series involve the holomorphic 3-form $\Omega_{\text{abc}} = q\epsilon_{\text{abc}}$, where the indices $\mathbf{a}, \mathbf{b}, \mathbf{c}$ run over complex coordinates on the conifold, ϵ is the Levi-Civita tensor, and

Table 6. Series III fluxes. Tabulated values are the adjusted radial scaling dimension $\Delta = 3 + \Delta_f$, where f is the scalar seed mode; the $SU(2) \times SU(2) \times U(1)$ quantum numbers ℓ_1, ℓ_2, R for f ; dimension of the representation; and whether the flux is chiral, defined to mean $\ell_1 = \ell_2 = R/2$ for the seed mode. We include the 15 modes with radial scaling dimensions that satisfy $2 < \Delta \leq 5.8$.

Δ	decimal scaling	ℓ_1	ℓ_2	R	dimension	type
3^a	3.0	0	0	0	1	chiral
$9/2$	4.5	$1/2$	$1/2$	1	4	chiral
$9/2$	4.5	$1/2$	$1/2$	-1	4	non-chiral
5	5.0	0	1	0	3	non-chiral
5	5.0	1	0	0	3	non-chiral
15						

^a Considered as a zero-mode of the scalar Laplacian ∇_0^2 , this mode is a constant. It was excluded from Table 3 because it does not contribute to $V_{\mathcal{H}}$ as explained in the main text. It also does not appear in the Series I or II fluxes, Tables 4–5, because these fluxes are all built from derivatives of the seed f . However, Series III fluxes include contributions from f without differentiation, so this mode can yield a nontrivial flux [48].

$q^*q = (-\det G_{AB})^{1/2}$ is the determinant of the Kähler metric. However, in $|\Lambda|^2$ these factors cancel with contractions involving the inverse metric. Therefore the angular terms in (2.34) involve only a product of the seed modes appearing in these tables.

Radial profile.—The integral in (2.34) factorizes into an integral over the radius r of the cone and an integral over the angles on $T^{1,1}$. First, consider the radial integral. For the fluxes described in Tables 4–6, radial dependence arises only from their scaling dimensions. Accordingly, given two fluxes Λ_1, Λ_2 and a fixed representation L drawn from the sum in (2.35), the Green’s function produces a radial profile

$$\text{radial profile} \propto \int_{r_{\text{IR}}}^{r_{\text{UV}}} \frac{dr'}{r'} g_L(r, r') \left(\frac{r'}{r_{\text{UV}}} \right)^{\Delta_1 + \Delta_2}, \quad (2.37)$$

where the factor $1/r'$ is produced by combining $(r')^5$ from the Jacobian $(-\det G_{AB})^{1/2}$ and $(r')^{-6}$ from three copies of the inverse metric needed for the contractions implied by $|\Lambda|^2$. There is an overall constant of proportionality that we do not write explicitly. The result is

$$\text{radial profile} \propto \frac{1}{r_{\text{UV}}^4} \left(\alpha x^{\Delta_1 + \Delta_2 - 4} + \beta x^{\Delta(L)} + \gamma x^{-4 - \Delta(L)} \left(\frac{r_{\text{IR}}}{r_{\text{UV}}} \right)^{\Delta(L) + \Delta_1 + \Delta_2} \right), \quad (2.38)$$

where $x = r/r_{\text{UV}}$ as above, and α, β, γ are roughly $\mathcal{O}(1)$ numerical coefficients. The term involving the infrared regulator r_{IR} is small provided $r_{\text{IR}}/r_{\text{UV}} \ll 1$ and formally vanishes in the limit $r_{\text{IR}} \rightarrow 0$. Therefore the integral does not accumulate large contributions from the region $r \sim r_{\text{IR}}$ where we need a precise resolution of the conifold singularity. We assume this term is negligible, and it will be dropped in the following discussion.

The remaining terms source radial profiles $\sim x^{\Delta(L)}$ and $\sim x^{\Delta_1+\Delta_2-4}$. The $x^{\Delta(L)}$ profile reproduces the radial scaling dimension associated with the scalar zero-modes of Table 3. This term will modify the coefficients associated with the L -representation in $V_{\mathcal{H}}$, Eq. (2.30). Fortunately, this is harmless: our premise is that we cannot predict these coefficients, which already depend on ultraviolet data. Combining two unknown coefficients merely yields another unknown coefficient. The other term, scaling like $x^{\Delta_1+\Delta_2-4}$, is new. It will produce contributions to the potential involving modes in the L -representation, but with a radial scaling dimension $\Delta_{12} = \Delta_1 + \Delta_2 - 4$ *different* to $\Delta(L)$. Note that Δ_{12} is guaranteed to be positive because $\Delta > 2$ for all flux modes that participate in the cross product. If this dimension falls below the truncation point then such terms should be retained.¹⁰

Angular terms.—Now consider the angular part of (2.34). We have already explained that factors coming from copies of the inverse metric in the contraction $|\Lambda|^2$ cancel with normalization adjustments in the individual fluxes. Therefore the integrand involves only the combination

$$\text{angular part} \propto \sum_{LM} \mathcal{E}_{LM}(\Psi) \int d^5\Psi' (-\det G_{T^{1,1}})^{1/2} \mathcal{E}_{LM}^*(\Psi') \mathcal{E}_{L'M'}(\Psi') \mathcal{E}_{L''M''}^*(\Psi'). \quad (2.39)$$

The modes $\mathcal{E}_{L'M'}$ and $\mathcal{E}_{L''M''}$ represent the quantum numbers of the two flux modes contributing to $|\Lambda|^2$. The two modes with quantum numbers LM contribute to the sum in the spectral representation of the Green's function, Eq. (2.35).

The complex conjugation on $\mathcal{E}_{L''M''}$ can be dropped without loss of generality, because this merely reverses the labels $L'' \rightarrow -L''$ and $M'' \rightarrow -M''$. To build Φ_- we will sum (L', M') and (L'', M'') over all entries in Tables 4–6, so this reversal is immaterial. Moreover, since \mathcal{E} transforms as a pair of $SU(2)$ representations, the tensor product $\mathcal{E}_{L_1 M_1} \mathcal{E}_{L_2 M_2}$ can be decomposed as a direct sum of similar representations. This follows from the same property of $SU(2)$, expressed via Clebsch–Gordan coefficients. Specifically, Wigner's ‘little’ d -matrix satisfies

$$d_{mn}^\ell(\beta) d_{m'n'}^{\ell'}(\beta) = \sum_{L=|\ell-\ell'|}^{\ell+\ell'} \langle \ell m, \ell' m' | LM \rangle \langle \ell n, \ell' n' | LN \rangle d_{MN}^L(\beta), \quad (2.40)$$

where $M = m + m'$ and $N = n + n'$. Here, $\langle \ell m, \ell' m' | LM \rangle$ is an ordinary Clebsch–Gordan coefficient. The $J_{\ell, m, R}(\theta)$ mode functions used to build the \mathcal{E}_{LM} harmonics are related to d_{mn}^ℓ via (2.24a)–(2.24b). Therefore, recalling $L = (\ell_1, \ell_2, R)$, $L' = (\ell'_1, \ell'_2, R')$, $M = (m_1, m_2)$ and $M' = (m'_1, m'_2)$, we conclude

$$\begin{aligned} \mathcal{E}_{LM}(\Psi) \mathcal{E}_{L'M'}(\Psi) &= \sum_{\mathcal{L}_1=|\ell_1-\ell'_1|}^{\ell_1+\ell'_1} \sum_{\mathcal{L}_2=|\ell_2-\ell'_2|}^{\ell_2+\ell'_2} \sqrt{\frac{(2\ell_1+1)(2\ell'_1+1)}{2(2\mathcal{L}_1+1)} \frac{(2\ell_2+1)(2\ell'_2+1)}{2(2\mathcal{L}_2+1)}} \\ &\quad \times \langle \ell_1 m_1, \ell'_1 m'_1 | \mathcal{L}_1 \mathcal{M}_1 \rangle \langle \ell_1 \frac{R}{2}, \ell'_1 \frac{R'}{2} | \mathcal{L}_1 \frac{\mathcal{R}}{2} \rangle \\ &\quad \times \langle \ell_2 m_2, \ell'_2 m'_2 | \mathcal{L}_2 \mathcal{M}_2 \rangle \langle \ell_2 \frac{R}{2}, \ell'_2 \frac{R'}{2} | \mathcal{L}_2 \frac{\mathcal{R}}{2} \rangle \mathcal{E}_{LM}(\Psi), \end{aligned} \quad (2.41)$$

¹⁰In Tables 4–6 we retained terms with $2 < \Delta \leq 5.8$. Inspection of the formula for Δ_{12} shows that to capture

where $\mathcal{M}_1 = m_1 + m'_1$, $\mathcal{M}_2 = m_2 + m'_2$, $\mathcal{R} = R + R'$, $\mathbb{L} = (\mathcal{L}_1, \mathcal{L}_2, \mathcal{R})$ and $\mathbb{M} = (\mathcal{M}_1, \mathcal{M}_2)$.¹¹

Substitution of (2.41) in (2.39) and use of the completeness relation (2.27) shows that the integral $d^5\Psi'$ collapses to $\delta_{\mathbb{L}\mathbb{L}}\delta_{\mathbb{M}\mathbb{M}}$. For fixed (L', M') , (L'', M'') , the angular part therefore reproduces the right-hand side of (2.41) after suitable relabelling of indices. To summarize, consider the cross product between any two fluxes Λ , Λ' drawn from Tables 4–6, with labels (L, M) and (L', M') and (adjusted) radial scaling dimensions Δ , Δ' . Unless both fluxes are chiral, their cross product makes a contribution to the brane potential, via the particular integral for Φ_- , of the form

$$\begin{aligned} \Lambda \times \Lambda' \rightarrow \frac{g_s}{96} \mu^4 \sum_{\mathcal{L}_1=|\ell_1-\ell'_1|}^{\ell_1+\ell'_1} \sum_{\mathcal{L}_2=|\ell_2-\ell'_2|}^{\ell_2+\ell'_2} \mathcal{A}(L, L', \mathbb{L}) \alpha x^{\Delta+\Delta'-4} \\ \times \langle \ell_1 m_1, \ell'_1 m'_1 | \mathcal{L}_1 \mathcal{M}_1 \rangle \langle \ell_1 \frac{R}{2}, \ell'_1 \frac{R'}{2} | \mathcal{L}_1 \frac{\mathcal{R}}{2} \rangle \\ \times \langle \ell_2 m_2, \ell'_2 m'_2 | \mathcal{L}_2 \mathcal{M}_2 \rangle \langle \ell_2 \frac{R}{2}, \ell'_2 \frac{R'}{2} | \mathcal{L}_2 \frac{\mathcal{R}}{2} \rangle \mathcal{E}_{\mathbb{LM}}(\Psi). \end{aligned} \quad (2.42)$$

As explained above, we have dropped corrections from the infrared end of the conifold and from the term scaling like $x^{\Delta(\mathbb{L})}$ which is already included in $V_{\mathcal{H}}$.

If both fluxes *are* chiral then this expression applies if Λ and Λ' are drawn from the same series; if not, their contribution should be set to zero. The total potential $V_{\mathcal{F}}$ should be obtained by summing (2.42) over all fluxes Λ , Λ' . In this expression $\mathcal{A}(L, L', \mathbb{L})$ is an unknown amplitude that absorbs the unknown constants of proportionality in (2.37) and (2.39). It depends on the recipes used to construct Λ and Λ' from their seed zero-modes, and also the amplitude with which these ‘building block’ fluxes appear in the supergravity solution for G_3 . It also absorbs the normalization factor that appears under the square-root in Eq. (2.41).

The final result is very complicated,^{12,13} and depends on constants such as $\mathcal{A}(L, L', \mathbb{L})$ that we cannot predict. To use it in a practical analysis one must make a number of largely arbitrary choices. Unfortunately, prior analyses of this model have generally not documented the choices made to convert Eq. (2.42) to a practical expression for the potential. In §4.3

contributions to Φ_- with $\Delta \leq 3.8$ it is sufficient to consider fluxes with scaling dimension in this range.

¹¹Ref. [9] used a direct numerical evaluation of (2.39) to compute the re-expansion of flux cross-products into \mathcal{E}_{LM} harmonics, but their implementation inadvertently neglected the angular Jacobian $(-\det G_{T^{1,1}})^{1/2}$. This will slightly change numerical values appearing in the re-expansion, and it may also change the selection rules that couple the quantum numbers (L, M) , (L', M') and (L'', M'') . Nevertheless, based on the numerical evidence to be discussed in §4.3 below it seems possible that this will not significantly influence the final distribution of observables reported by these authors.

¹²In Refs. [2, 52] the combined potential from *both* the Φ_- complementary function and particular integral was represented in the form of Eq. (2.30); see Eq. (5) of Ref. [52] and Eq. (5.57) of Ref. [2]. Although this method of presentation was no doubt intended to suppress needless complexity, we believe that the more precise form of (2.42) is helpful. In particular, in (2.42) it is clear that the radial scaling dimension for each term cannot be computed just from knowledge of the representation L for the harmonic with which it appears, as (2.29) and (2.30) would imply. Terms generated from the cross-product between fluxes may occur with a radial scaling dimension $\Delta + \Delta' - 4$ that has no simple relation to the harmonic $\mathcal{E}_{\mathbb{LM}}$ with which they are partnered in the potential.

¹³In Agarwal et al. [52], a list of lowest scaling dimensions was given in Eq. (6). However, the value $\sqrt{28} - 3$ in this list should not appear. It is absent from the similar list given in Ref. [47]. We would like to thank

we discuss numerical experiments in which the flux-sourced contributions described in this section are dropped, and find that this significantly affects the mass spectrum. The impact on observables is more modest but not negligible, and therefore a precise specification of $V_{\mathcal{F}}$ is necessary.

Our choices are as follows. First, we do not attempt to model the numerical coefficient $g_s \alpha \mathcal{A} / 96$ that normalizes Eq. (2.42). We collect these numerical factors into a single statistical Wilson coefficient $\mathcal{C}_{\mathbb{LM}}$ whose real and imaginary parts are assumed to be drawn from the same distributions that characterize the coefficients C_{LM} in Eq. (2.30); see Table 1. Second, we *do* track the numerical value of the Clebsch–Gordan factors. If the same mode $x^{\Delta+\Delta'-4} \mathcal{E}_{\mathbb{LM}}$ is produced from more than one cross-product of the fluxes in Tables 4–6, we add their numerical coefficients coherently to produce a single numerical prefactor. An alternative would be to treat each occurrence as an independent random variable, rather than add the amplitudes coherently. Yet another choice would be to model the Clebsch–Gordan coefficients as a Kronecker- δ , equal to zero if the Clebsch–Gordan factors give zero and unity otherwise. Our procedure is intended to model, at least approximately, cases where the Clebsch–Gordan coefficients are unusually large or small, without causing a proliferation of parameters that unnecessarily enlarge the sample space. In practice the Clebsch–Gordan values typically do not vary significantly for the range of quantum numbers we are using and are almost always $\mathcal{O}(1)$.

Notwithstanding the foregoing discussion, the analysis discussed in §4.3 does offer hope that the precise procedure used to model the amplitude of individual contributions to the potential will not radically alter the final distribution of observables. A detailed understanding will require further numerical work that is beyond the scope of this paper.

Summary: the complete brane potential.—To summarize, the total potential for the D3-brane consists of:

- the Coulomb term (2.11),
- the mass term (2.12) generated by coupling to the four-dimensional Ricci scalar,
- the homogeneous terms (2.30) generated by the complementary function for Φ_- ,
- the terms generated by (2.42), with amplitudes modelled as described above, from the particular integral for Φ_- .

3 Experimental procedure

In §3.1 we describe our software stack and sampling strategy, and our procedure for collecting observables. In §3.2 we explain our definition of an adiabatic limit, based on studying eigenvalues of the mass matrix. Finally, in §3.3 we compare the performance of our pipelines and the resulting distributions, and show that (with some caveats) these demonstrate good agreement.

Nishant Agarwal for confirmation of this observation.

3.1 Software stack and sampling strategy

We employ two separate pipelines to harden our analysis against numerical and implementation errors. One pipeline is based on the **CppTransport** platform [5, 6]. This is a C++ framework for computation of inflationary observables, up to and including those derived from the three-point function, based on an implementation of the ‘transport’ method [10, 11, 14, 15]. The second pipeline is based on **PyTransport** [7, 8]. This is an independent Python implementation of the same transport system, but making different numerical choices and using a different numerical integrator. Neither pipeline uses the slow-roll approximation, except to set initial conditions for each correlation function.

Although **CppTransport** and **PyTransport** are related, they are not equivalent: their implementation details differ, including the exact set of equations that are solved and the underlying computer algebra system used to perform symbolic computations.¹⁴ Therefore comparison between these pipelines is not empty. Differences in their output can be regarded as an indication of the ‘implementation error’ from our inability to perform perfectly accurate computations.

At the base of the software stack we use a shared Python script that builds versions of Tables 3 and 4–6 and combines them according to the rules of Eqs. (2.30) and (2.42) to obtain their contribution to the D3-brane potential. We restrict attention to operators with radial scaling dimension $\delta \leq \Delta_{\text{max}} = 3.8$, as explained in §§2.3–2.4 above. The script writes out **CppTransport** and **PyTransport** model files containing canonical forms for the potential, its first three derivatives, the components of the field-space metric and its inverse, and the components of the field-space Riemann tensor R^A_{BCD} . By sharing expressions for these quantities we ensure that both pipelines perform their calculations using the *same* parametrization, so that subsequent analyses compare like to like. After this stage, symbolic manipulations carried out by the pipelines are independent.

3.1.1 CppTransport pipeline¹⁵

The **CppTransport** translator converts the model file into a custom **CosmoSIS** module [34]. It expects an input datablock containing the 1,212 parameters of the inflationary model,¹⁶ and uses **CppTransport**’s internal solver to obtain values for the corresponding background evolution and n -point functions. These are written into the outgoing datablock for use by later stages of the pipeline.

This implementation is used to generate our primary trajectory catalogue and compute observables for its members. There are two steps. First, as explained in §1, we generate a catalogue of inflationary solutions by sampling over 450,000,000 trajectories. Our methodology is essentially that proposed by Easter et al. [90]. We use the **apriori** sampler (part of the default **CosmoSIS** package) to repeatedly draw realizations of the parameters listed in Table 1. Each trajectory is evolved from fixed initial conditions $x = 0.9$ and $\theta_1 = \theta_2 = \phi_1 = \phi_2 = \psi = 1$, with the field velocities set to zero. The observables do not depend significantly on these

¹⁴The systems used are **GiNaC** [89] for **CppTransport** and **SymPy** for **PyTransport**.

¹⁵An early version of the **CppTransport** pipeline was written by Sean Butchers, whom we thank for assistance in preparing this section.

¹⁶For details of the data flow through a **CosmoSIS** pipeline, see Ref. [34].

choices, as we explain in §4.3 below. The calculation terminates when either: (1) inflation exits gracefully as ϵ smoothly approaches unity, or (2) the $D3/\overline{D3}$ pair dissolve in a hybrid transition, taken to occur when their separation is smaller than $\Delta x = 0.02$. The Lagrangian parameters and Wilson coefficients for the subset of roughly 90,000 trajectories that inflate for $N > 60$ e-folds constitute the required catalogue. A candidate trajectory is rejected if any of the following conditions apply:

- it is not initially inflating,
- it does not reach the hybrid transition that describes $D3/\overline{D3}$ annihilation while inflation is still ongoing, or within a cutoff of 10,000 e-folds,
- the brane is ejected from the ultraviolet end of the throat,
- the potential becomes negative at any point in the evolution,
- numerical overflow, underflow or an integration error occurs.¹⁷

Catalogue of observables.—Second, the completed catalogue is processed to determine inflationary observables for each trajectory. The calculation is broken into reusable components that are assembled as a second **CosmoSIS** pipeline, controlled programmatically rather than coupled to a sampler. For each entry in the catalogue the pipeline performs the following steps:

STEP 1 — TWO-POINT FUNCTION

Power spectra: It was explained in §1 that the power spectrum in the $D3/\overline{D3}$ model is often not scale invariant (or even monotonic), and therefore summary observables measured at a single scale are frequently a poor predictor of the goodness-of-fit to observation. Nevertheless, they have some uses. They allow us to compare with previous analyses, and they are still a convenient way to organize our catalogue of trajectories.

For these reasons we collect summary power spectrum observables A_s , A_t , and r , evaluated at $k_\star = 0.002 \text{ Mpc}^{-1}$. Here, $A_s \equiv \mathcal{P}_\zeta(k_\star)$ and $A_t \equiv \mathcal{P}_h(k_\star)$ measure (respectively) the amplitude of the dimensionless power spectra for the uniform-density gauge curvature perturbation ζ , and for tensor modes. They are defined in terms of equal-time correlation functions,

$$\langle \zeta(\mathbf{k}) \zeta(\mathbf{k}') \rangle = (2\pi)^3 \delta(\mathbf{k} + \mathbf{k}') P_\zeta(k) = (2\pi)^3 \delta(\mathbf{k} + \mathbf{k}') \frac{2\pi^2}{k^3} \mathcal{P}_\zeta(k), \quad (3.1a)$$

$$\langle h_s(\mathbf{k}) h_{s'}(\mathbf{k}') \rangle = (2\pi)^3 \delta(\mathbf{k} + \mathbf{k}') \delta_{ss'} \frac{\pi^2}{2k^3} \mathcal{P}_h(k), \quad (3.1b)$$

where $h_s(\mathbf{k})$ is a tensor perturbation of polarization s ($s = +, \times$) in a normalization where the polarization matrices \mathbf{e}^s satisfy $\text{tr}(\mathbf{e}^s \cdot \mathbf{e}^{s'}) = 2\delta^{ss'}$. With this definition the tensor spectrum is conventionally normalized and the tensor-to-scalar ratio satisfies $r \equiv A_t/A_s$.

Spectral indices: We evaluate the ζ spectral index n_s at $k = k_\star$,

$$n_s - 1 \equiv \left. \frac{d \ln \mathcal{P}_\zeta}{d \ln k} \right|_{k=k_\star}, \quad (3.2)$$

¹⁷During integration, **CppTransport** automatically tests for the following error conditions: (a) H^2 becoming

Because of the flatness of the tensor spectrum, there are trajectories for which it is not straightforward to collect a reliable numerical estimate of the spectral index $n_t \equiv d \ln \mathcal{P}_h / d \ln k$. For a detailed discussion of this and other computational details see §3.1.2 below.

Matching equation: To relate physical scales to a horizon-exit time we use the matching equation [91–93],¹⁸

$$N(k) = 59.57 - \ln \frac{k}{k_\star} + \ln \left(\frac{H_k}{10^{16} \text{ GeV}} \frac{M_{\text{P}}^{1/2}}{H_{\text{end}}^{1/2}} \right), \quad (3.3)$$

where $N(k)$ is the horizon exit time of the physical mode k , measured in e-folds from the end of inflation. The corresponding Hubble rates are H_k and H_{end} , respectively. We assume that reheating completes instantaneously, and that decay products from break-up of the scalar condensates thermalize into radiation.

STEP 2 — THREE-POINT FUNCTION

Equilateral and folded configurations: We measure the amplitude of three-point correlations for two indicative $\langle \zeta \zeta \zeta \rangle$ bispectrum configurations. In the Fergusson–Shellard parametrization,¹⁹ these are: (1) an equilateral configuration $\{k_t = 3k_\star, \alpha = 0, \beta = 1/3\}$; and (2) a folded configuration $\{k_t = 3k_\star, \alpha = 0, \beta = 0.005\}$. We report the correlation as a measurement of the reduced bispectrum $f_{\text{NL}}(k_1, k_2, k_3)$, defined by

$$f_{\text{NL}}(k_1, k_2, k_3) = \frac{6}{5} \frac{B_\zeta(k_1, k_2, k_3)}{P_\zeta(k_1)P_\zeta(k_2) + \text{cyclic}}, \quad (3.4)$$

where ‘+ cyclic’ implies that the preceding term is to be summed over cyclic permutations of the momenta k_1, k_2, k_3 . The ζ bispectrum B_ζ satisfies

$$\langle \zeta(k_1) \zeta(k_2) \zeta(k_3) \rangle = (2\pi)^3 \delta(\mathbf{k}_1 + \mathbf{k}_2 + \mathbf{k}_3) B_\zeta(k_1, k_2, k_3) \quad (3.5)$$

and the correlator is computed at equal times. When evaluated on our representative equilateral and folded configurations we denote the reduced bispectrum by $f_{\text{NL}}^{\text{eq}}$ and $f_{\text{NL}}^{\text{fold}}$, respectively.

negative; (b) $\epsilon \equiv -\dot{H}/H^2$ becoming negative; (c) ϵ becoming greater than 3; (d) V becoming negative; (e) any component of a correlation function becoming ∞ or NaN.

¹⁸See Eq. (20) of Ref. [93], from which we have dropped the slow-roll approximation. Note that there is a minor typo in the version of this equation that appears in Ref. [93]; the correct numerical constant appearing in it should be 55.98, not 55.75. The numerical constant quoted in (3.3) includes this correction. We thank Peter Adshead for helpful correspondence.

¹⁹The momenta $\mathbf{k}_1, \mathbf{k}_2, \mathbf{k}_3$ that participate in a three-point function such as $\langle \zeta(\mathbf{k}_1) \zeta(\mathbf{k}_2) \zeta(\mathbf{k}_3) \rangle$ satisfy the ‘triangle’ condition $\mathbf{k}_1 + \mathbf{k}_2 + \mathbf{k}_3 = 0$ as a consequence of statistical translation invariance. This makes the correlator a function only of k_1, k_2, k_3 . In the Fergusson & Shellard parametrization we set $k_t = k_1 + k_2 + k_3$

Squeezed configurations: As explained in §1 and Appendix B, it is too time-consuming to compute three-point correlations on a squeezed configuration for the entire primary catalogue. Instead, we sample the squeezed configurations $\{k_t = 3k_*, \alpha = 0, \beta = 0.9\}$ and $\{k_t = 3k_*, \alpha = 0, \beta = 0.95\}$ on a separate catalogue of trajectories to determine how their amplitudes correlate with the equilateral and folded configurations.

STEP 3 — ADIABATIC LIMIT

The mass spectrum is computed from the eigenvalues of the mass matrix $M^A{}_B$ [14, 74, 75],

$$M^A{}_B = \nabla^A \nabla_B V - R_J{}^A{}_{BK} \dot{X}^J \dot{X}^K - \frac{3 + \epsilon}{M_{\text{P}}^2} \dot{X}^A \dot{X}_B + \frac{\dot{X}^A \ddot{X}_B + \dot{X}_B \ddot{X}^A}{H M_{\text{P}}^2}, \quad (3.6)$$

where the X^A are the scalar fields $\{x, \theta_1, \theta_2, \phi_1, \phi_2, \psi\}$ appearing in Eqs. (2.8)–(2.9). Indices on \dot{X}^A and $\ddot{X}^A \equiv \dot{X}^B \nabla_B \dot{X}^A$ are raised and lowered using the conifold metric G_{AB} normalized as in Eq. (2.9), ∇_A is the covariant derivative compatible with G_{AB} , and R_{ABCD} is the Riemann tensor constructed from ∇_A . We sample these eigenvalues at $N = 55$, $N = 2.5$, $N = 1$ and $N = 0$ e-folds before the end of inflation. In §3.2 below we explain how these are used to detect the onset of an adiabatic limit.

STEP 4 — LIKELIHOOD FUNCTION

Finally, where possible we compute the CMB likelihood for this trajectory using the Planck2015 likelihood code [96].²⁰ The ζ power spectrum is sampled at 100 logarithmically-spaced wavenumbers in the range $10^{-6} \text{ Mpc}^{-1} \leq k \leq 50 \text{ Mpc}^{-1}$. This sample is passed to **CLASS** via the **CosmoSIS** pipeline and used to compute the CMB angular power spectra C_ℓ^{TT} , C_ℓ^{TE} and C_ℓ^{EE} . We do not vary the parameters of the post-inflationary cosmology, which are fixed to their Planck2015 best-fit values [97]. The bundled **CosmoSIS planck** module is used to calculate the likelihood for all these C_ℓ . If desired, any other likelihood could be substituted in this step.

3.1.2 Computational issues

Ultra slow-roll inflation.—In the D3/ $\overline{\text{D3}}$ model it is known that extended epochs of inflation are typically realized near an inflexion point in the potential [9, 44, 52]. Therefore we must allow for the possibility that some inflationary trajectories enter a phase of ultra slow-roll to be the perimeter of the momentum triangle. Then [94],

$$\begin{aligned} k_1 &= \frac{k_t}{4}(1 + \alpha + \beta), \\ k_2 &= \frac{k_t}{4}(1 - \alpha + \beta), \\ k_3 &= \frac{k_t}{2}(1 - \beta). \end{aligned}$$

An equivalent parametrization had earlier been introduced by Rigopoulos, Shellard & van Tent [95].

²⁰In fact, this is not done for all trajectories. In some cases we have $N \geq 60$ e-folds of inflation from the initial conditions, but too few total e-folds to allow 4.5 e-folds of subhorizon evolution for the largest scale $k = 10^{-6} \text{ Mpc}^{-1}$ needed for the **CLASS** computation of the C_ℓ . In such cases there is a choice between rejecting the trajectory or foregoing the Planck likelihood. We choose the latter.

dynamics [98–102]. Such phases are characterized by: (1) $V' \approx 0$, (2) a small and rapidly decaying value of $\epsilon \equiv -\dot{H}/H^2$, and (3) $\eta \approx -6$. Previously, the possibility of an ultra slow-roll phase in this model does not appear to have been considered.

At the level of the background, both **CppTransport** and **PyTransport** implement the full scalar field dynamics and therefore capture all ultra slow-roll effects. However, initial conditions for each correlation function are estimated using analytic expressions that assume slow-roll dynamics [15]. This is harmless if the dynamics are close to slow-roll while the momenta characterizing an individual correlation function are exiting the horizon, even if a transition to ultra slow-roll inflation occurs later. If slow-roll does not apply the procedure is still mostly harmless for the two-point function, because the slow-roll result $\mathcal{P}_{\delta\phi} \sim H^2$ continues to apply during ultra slow-roll inflation [98]. Therefore the initial condition will be significantly inaccurate only for modes that exit during a transition between slow-roll and ultra slow-roll phases.

The prospects for the three-point function are less straightforward because the slow-roll initial condition is corrected by terms of order η [103–105], which is large during ultra slow-roll. It follows that numerical three-point functions computed by **CppTransport** and **PyTransport** must be treated with caution for scales exiting during an ultra slow-roll phase. Nevertheless, if the calculation starts sufficiently far before horizon exit and the $\mathcal{O}(\eta)$ displacements do not take the initial condition out of the basin of attraction of the true solution, we may still expect the results to be valid. We return to this question in §4.1.

Power spectrum amplitudes.—The amplitudes A_s and A_t , and hence r , are computed directly. In a transport implementation, numerical accuracy is usually determined by the number of e-folds of subhorizon evolution; see Ref. [15] for a detailed discussion. We use 4.5 e-folds, which (subject to the caveats below for the tensor power spectrum) we find to be a reasonable compromise between accuracy and integration time. We have performed a small number of spot-checks to test convergence with increasing subhorizon e-folds, but these do not show significant improvement: see Fig. 2. Accuracy also depends on the choice of stepper. We find that Runge–Kutta (Dormand–Prince and Fehlberg) and Adams–Bashforth–Moulton methods sometimes exhibit instabilities, especially in three-point amplitudes, although in our tests these did not propagate to ζ observables. The Bulirsch–Stoer variable order method produces fast, high-precision solutions without significant instabilities. However, we do not find that the choice of stepper has a significant effect on our final distributions. For the construction of our primary catalogue we use the Dormand–Prince 4th/5th-order method.

Numerical precision.—The integrations needed for the D3/ $\overline{\text{D3}}$ model are complex and involve a large number of intermediate steps. If significant cancellations occur, there is a risk of accumulating inaccuracies from roundoff error. To test whether extended precision is needed we have compared a subsample of 1,000 trajectories from our main catalogue using **double** and **long double** precision.²¹ In nearly all cases we find only sub-percent shifts in n_s . However, for $f_{\text{NL}}^{\text{eq}}$ we find $\sim 9\%$ of trajectories exhibit shifts larger than 1%, and $\sim 2\%$ of trajectories exhibit shifts larger than 5%. A handful of trajectories shift by 10% or more.

²¹The meaning of **long double** is implementation-dependent, but on our production Linux platform with the GCC compiler this is an 80-bit extended precision format. For comparison, **double** is a 64-bit format.

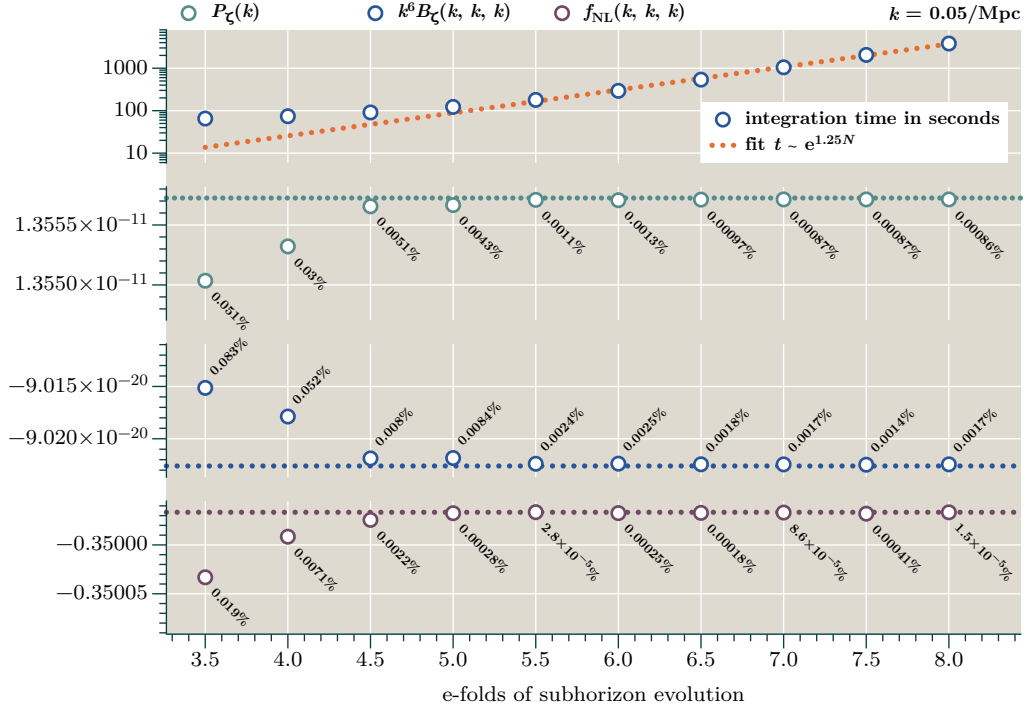


Figure 2. Dependence on number N_{subh} of e-folds of subhorizon evolution for the representative trajectory #32327. **Top panel:** integration time in seconds. The dotted orange line shows a fit to the exponential dependence $t \sim e^{1.25N}$, which is valid for $N_{\text{subh}} \gtrsim 5.5$. Increasing the number of subhorizon e-folds is very expensive, but the following panels show there are diminishing returns for $N_{\text{subh}} \gtrsim 4.5$. **Second panel:** Convergence of \mathcal{P}_ζ evaluated at $k = 0.05 \text{ Mpc}^{-1}$. The asymptote is extracted by fitting a function of the form $a - be^{-cN}$ and measuring a . The labels show the percentage deviation from this asymptotic value. **Third panel:** Same as second panel, but for $k^6 B_\zeta(k, k, k)$ measured on an equilateral configuration of side $k = 0.05 \text{ Mpc}^{-1}$. **Bottom panel:** Same as second panel, but for $f_{\text{NL}}(k, k, k)$ measured on the same equilateral configuration.

Therefore, while the enhanced precision is not required in most cases, it apparently *is* needed to accurately predict three-point observables for certain trajectories—but we will see in §3.3 that these differences do not seem to be reflected in the distribution over an entire catalogue. Nevertheless, we prefer to use the extended precision calculation out of an abundance of caution.

CppTransport supports arbitrary precision arithmetic (although with a significant performance penalty), so although we have not done so it would be possible to perform the calculation with even higher precision than `long double` to verify that it has properly converged. Similar benefits from use of `long double` precision are known to occur in models of ultra slow-roll inflation, which has features that are similar to the $D3/\overline{D3}$ model.

Spectral indices.—Computation of spectral indices is more challenging, especially for the tensor power spectrum which is extremely flat. Several numerical strategies are available. When applied to the ζ spectral index n_s these methods all yield consistent results, but none are entirely satisfactory for the tensor spectral index n_t .

To be concrete, we collect the fields X^A and the corresponding momenta $\pi^A \equiv dX^A/dN$ into a single phase-space coordinate $\mathcal{X}^{\mathbb{A}} = (X^A, \pi^B)$ and define the two-point function for $\delta\mathcal{X}^{\mathbb{A}}$ to satisfy

$$\langle \delta\mathcal{X}^{\mathbb{A}}(\mathbf{k}_1) \delta\mathcal{X}^{\mathbb{B}}(\mathbf{k}_2) \rangle = (2\pi)^3 \delta(\mathbf{k}_1 + \mathbf{k}_2) \Sigma^{\mathbb{AB}}(k), \quad (3.7)$$

where $k = |\mathbf{k}_1| = |\mathbf{k}_2|$. The ζ power spectrum P_ζ can be written $P_\zeta(k) = N_{\mathbb{A}} N_{\mathbb{B}} \Sigma^{\mathbb{AB}}(k)$, where explicit expressions for the coefficients $N_{\mathbb{A}}$ are known [10, 14, 15, 74, 106]. They become independent of k on superhorizon scales. The first option is to write a transport equation for the ‘spectral matrix’ $n^{\mathbb{AB}} \equiv d\Sigma^{\mathbb{AB}}/d \ln k$, which can be used to compute n_s [9, 14, 15],

$$n_s - 1 = 3 + \frac{N_{\mathbb{A}} N_{\mathbb{B}} n^{\mathbb{AB}}}{N_{\mathbb{C}} N_{\mathbb{D}} \Sigma^{\mathbb{CD}}}. \quad (3.8)$$

We briefly review this approach in Appendix C. It is conceptually clean, but as explained in Ref. [14] it can happen that we require more e-folds of subhorizon evolution to obtain good numerical results for $n^{\mathbb{AB}}$ than for $\Sigma^{\mathbb{AB}}$. This is partly because to compute $n_s - 1$ we effectively subtract the leading term from the right-hand side of (3.8).

A similar expression applies for n_t , although the calculation is simpler because no gauge transformation is required. For both n_s and n_t we attempt to accelerate convergence by using initial conditions that include subleading terms in both the slow-roll expansion and $k/(aH)$. We find that Eq. (3.8) gives results for n_s that agree with other methods, but its counterpart for n_t does not always yield good results even with a large number of subhorizon e-folds.

A second option is to fit a function of the form $\mathcal{P} = A_\star (k/k_\star)^n$ to sampled values of the power spectrum \mathcal{P} near the pivot scale k_\star , and extract the spectral index from the fit for n . This approach has the advantage that it requires only knowledge of the power spectrum and not the spectral matrix. The disadvantage is that the fit can be thrown off by small inaccuracies in the computed amplitude, perhaps caused by noise or other numerical artefacts. If the spectrum has non-negligible tilt these do not usually affect the measured spectral index. However, for the D3/ $\overline{\text{D3}}$ model, based on analytic estimates we expect roughly $10^{-14} \lesssim n_t \lesssim 10^{-2}$. Because n_t is so small, fluctuations in excess of $\delta \ln \mathcal{P}_h \sim n_t \delta \ln k$ can be present between samples with k -spacing $\delta \ln k$ (even with the high-precision Bulirsch–Stoer stepper).

Specifically, for some trajectories we find the tensor power spectrum to be contaminated by oscillations of very small amplitude. These can spoil automated measurement of n_t . The source of these oscillations is not clear, but they are almost certainly not physical. Their amplitude typically decreases when we allow more subhorizon e-folds. On some trajectories this is sufficient to extinguish the oscillations, but on others their amplitude appears nearly stable. Based on this, we speculate that they are possibly a discretization artefact. If so, the same effect (or a closely related one) may be responsible for the poor outcomes from the $n^{\mathbb{AB}}$ transport equation, which include positive values for n_t at some values of k . This is incompatible with the strong energy condition, which implies that H should decrease. We see similar results from attempts to fit for n_t , which can yield positive values by catching the rising edge of an oscillation. This effect can be mitigated by binning the power spectrum before performing the fit, but it is difficult to do this in an automated way without risking errors

from over-smoothing. The significant challenge entailed in obtaining an accurate estimate of n_t was already noted by McAllister et al. [59].

In practice, the sampling pipeline fits a quadratic polynomial to 15 logarithmically-spaced power spectrum samples between $k = 1.986 \times 10^{-3} \text{ Mpc}^{-1}$ and $k = 2.014 \times 10^{-3} \text{ Mpc}^{-1}$. We have performed spot-checks on roughly 1,200 trajectories to compare the ζ spectral index computed this way with Eq. (3.8). With 4.5 e-folds of subhorizon evolution we find these are typically consistent within 1%. For a handful of trajectories, we make a further confirmation that these estimates are *also* consistent with fits performed ‘by hand’ using a different range of k . Unfortunately, for n_t we find that these fitting procedures typically disagree. We conclude that computing the tensor spectral index using either method is not acceptable for the D3/ $\overline{\text{D3}}$ model.

A third option is to use an analytic approximation for the tensor power spectrum to estimate $n_t \approx -2\epsilon$, which requires only knowledge of the background. This approach has the advantage that it does not depend on the accuracy with which we can compute the power spectrum amplitude. Conversely, it is blind to information provided by the transport calculation that is not included in the analytic approximation. We find negligible correlation between measurements using our numerical procedure and those obtained from $n_t \approx -2\epsilon$, but this is to be expected in light of the foregoing discussion.

In conclusion, using the estimate $n_t \approx -2\epsilon$ is apparently the least unsatisfactory option. In §4 the values of n_t we quote are derived using this method with ϵ sampled at 60 e-folds before the end of inflation. Based on ‘by hand’ fits to the smoothed tensor power spectrum, we believe the resulting values of n_t are accurate within a factor of 2 (but sometimes much better). For now, it is prudent to treat our n_t estimates with caution.

3.1.3 PyTransport pipeline

The second pipeline is based on **PyTransport**. Its main purpose is to perform a number of smaller ($\sim 18,000$ trajectory) complementary studies that explore the dependence of observables on discrete choices made in §2. We also use it to test for consistency with the principal catalogue. Symbolic computation of the potential and curvature tensors is shared with the **CppTransport** pipeline, but otherwise there is no code re-use.

There are some important differences. The **PyTransport** pipeline collects less fine-grained metadata about the trajectory. Observables are mostly computed as explained above, except that to give discrepancies an opportunity to manifest we apply a different fitting prescription for the spectral index. This is based on fitting a spline to five sampled power spectrum values for k -modes with horizon exit values spaced 0.3 e-folds apart. We use 4.5 e-folds of subhorizon evolution, as above, but **PyTransport** does not offer an option to change the stepper or value type and therefore we use the built-in Runge–Kutta 4/5th-order solver and **double** precision arithmetic. **PyTransport** does not currently implement calculation of the tensor power spectrum, so we do not sample r . The pipeline is not controlled by **CosmoSIS**, but uses a custom sampling layer that draws parameter combinations from the priors listed in Table 1 until a prescribed number of trajectories supporting $N > 60$ e-folds of inflation have been sampled. However, the criteria for rejecting trajectories are the same as those given on p. 31. The **PyTransport** pipeline does not compute C_ℓ^{TT} , C_ℓ^{TE} , C_ℓ^{EE} , or the CMB

Table 7. ‘Small’ studies performed using the **PyTransport** pipeline

study	prior
initial conditions	$x \sim N(0.9, 0.02); \theta_i \sim U(0, \pi); \phi_i \sim U(0, 2\pi); \psi \sim U(0, 4\pi)$
size of throat ^a	$\phi_{UV} \sim N(0.1, 0.02)$
sensitivity to truncation ^b	$\Delta_{\max} \in \{3.8, 3, 2\}$
homogeneous potential ^c	$\mathcal{C}_{L,M} = 0$
drop V_0 uplift ^d	$\alpha = 0$

^a Notice that with our conventions, ϕ_{UV} also appears in the potential via the definition of the dimensionless radial coordinate x ; cf. Eqs. (2.11) and (2.13). Therefore variation of ϕ_{UV} does not *only* vary the size of the throat, but also adjusts the scale of some terms in the potential.

^b Agarwal et al. studied the potential with the same truncations used here, that is

$\Delta_{\max} \in \{3.8, 3, 2\}$ [52]. Dias et al. studied the cases $\Delta_{\max} \in \{3.8, 3\}$ [9].

^c This prior corresponds to switching off terms in the potential sourced by the flux product $g_s |\Lambda|^2 / 96$. Only the Coulomb term, mass term and the sum of scalar zero-modes (2.30) are retained.

^d Setting $\alpha = 0$ allows us to compare with the prior analyses reported by Agarwal et al. [52], Dias et al. [9], and McAllister et al. [59]. This study is smaller than the others and comprises $\sim 5 \times 10^3$ trajectories.

likelihood function.

Finally, we apply a different prior for Q . Specifically, we choose $Q \sim \beta'(4.16, 494)$, where the ‘beta-prime’ (or ‘inverted beta’) distribution $\beta'(\alpha, \beta)$ is characterized by shape parameters α, β and has the probability distribution function $\mathbf{P}(x) = x^{\alpha-1}(1+x)^{-\alpha-\beta}/B(\alpha, \beta)$, where $B(x, y) = \Gamma(x)\Gamma(y)/\Gamma(x+y)$ is the Euler β -function. This choice is not motivated by physics, but rather sampling efficiency. We will see below that values of Q that frequently support $N > 60$ e-folds of inflation are tightly clustered. It is this phenomenon that underlies the choice $Q \sim U(0, 0.04)$ made in Table 1, which enhances sampling efficiency but has the drawback that it excludes the region $Q > 0.04$ completely. To assist in exploring this region we use the opportunity provided by the **PyTransport** pipeline to introduce a prior that cannot be implemented using **CosmoSIS**. The beta-prime distribution samples the region of parameter space that is preferential for obtaining $N > 60$ e-folds of inflation, while still exhibiting broad tails that allow less-likely regions to be explored. We find that the posterior distribution for Q is completely consistent with the posterior produced from the more restrictive prior used by **CppTransport**.

In Table 7 we list the different ensembles to be analysed using the **PyTransport** pipeline. In each case the priors match those given in Table 1 except for the stated variations. Each sample comprises roughly 18×10^3 trajectories, except for the $\alpha = 0$ study which uses a smaller number of trajectories ($\sim 5 \times 10^3$).

3.2 The adiabatic limit

To determine whether the observables we collect are related to quantities observable in the CMB or large-scale structure, we must understand whether the dynamics become adiabatic

before the end of inflation. Where this happens the perturbations are typically conserved through the subsequent evolution, provided they remain on superhorizon scales. On the other hand, if the evolution does not become adiabatic then the value of each observable may evolve during and after reheating until all isocurvature modes are exhausted [26–30, 107–109]. Here, ‘adiabatic’ has its usual cosmological meaning that there is effectively a single trajectory followed by each patch of spacetime smoothed on some superhorizon scale. The difference between neighbouring patches can only be a time offset δt along this trajectory, from which all other perturbations can be derived.

To diagnose the emergence of an adiabatic trajectory we inspect the eigenvalues of the mass matrix (3.6) collected in STEP 3 of §3.1.1. Note that the relevant mass matrix is not merely the covariant Hessian $\nabla^A \nabla_B V$ that would describe the mass matrix for the scalars alone, but includes mixing with scalar modes of the metric. To obtain the correct mass spectrum it is critical to account for this mixing [110, 111].

On an inflationary trajectory there will typically be one massless or tachyonic mode that is the would-be conserved Goldstone mode $\zeta \sim \delta\phi_{\text{ad}}/(\sqrt{2\epsilon}M_{\text{P}})$ associated with broken time translation invariance along the adiabatic direction [106]. Eigenvectors in the subspace orthogonal to this adiabatic direction span the available isocurvature modes, and their corresponding eigenvalues determine their growth or decay. Fluctuations in a direction with eigenvalue m^2 typically evolve like $s(N) = s_0 e^{-\eta(N-N_0)}$, where s_0 is the amplitude at a fiducial time $N = N_0$ and $\eta = m^2/(3H^2)$. Therefore fluctuations decay rapidly in any ‘heavy’ direction where the eigenvalue satisfies $m^2 \gtrsim 3H^2$.

Exponential suppression implies that isocurvature modes rapidly become small but are never completely extinguished, so there is no unique criterion to determine when a trajectory has become ‘sufficiently’ adiabatic. We choose to sample the mass spectrum at $N = 0$, $N = 1$ and $N = 2.5$ e-folds before the end of inflation. The trajectory is declared to be adiabatic if the following conditions apply at all three sample points: (1) one eigenvalue of the mass-matrix is tachyonic, and (2) $N - 1$ eigenvalues are heavy in the sense $m^2/(3H^2) > 1$ [23–25, 112].²² This implies a minimum suppression of $e^{-2.5} \approx 8 \times 10^{-2}$ in each isocurvature direction, but usually substantially more.

3.3 Agreement between pipelines

We now turn to the question of compatibility between the two pipelines, which enables us to assess the integrity of our numerical computations.

Trajectory-level agreement.—First, we have performed a number of spot-checks to verify that the pipelines yield compatible results given the same input data. With matching initial conditions and parameter values, we typically find agreement to better than 0.1% for n_s and

²²This is a sharper criterion than the one proposed in Refs. [9, 24], in which it was suggested by analogy with the formation of caustics that adiabaticity could be associated with regions where the dilation θ of a narrowly collimated bundle of trajectories becomes large. For a flow of inflationary trajectories the dilation is approximately given by a normalized sum of eigenvalues $\theta \approx \sum_i m_i^2/H^2$. Therefore the criterion $\theta \gg 1$ is necessary but not sufficient to yield an adiabatic limit in our sense. For example, it can happen that $\theta \gg 1$ but more than one eigenvalue remains light. In this case the trajectories converge onto a sheet rather than degenerating to a single adiabatic trajectory.

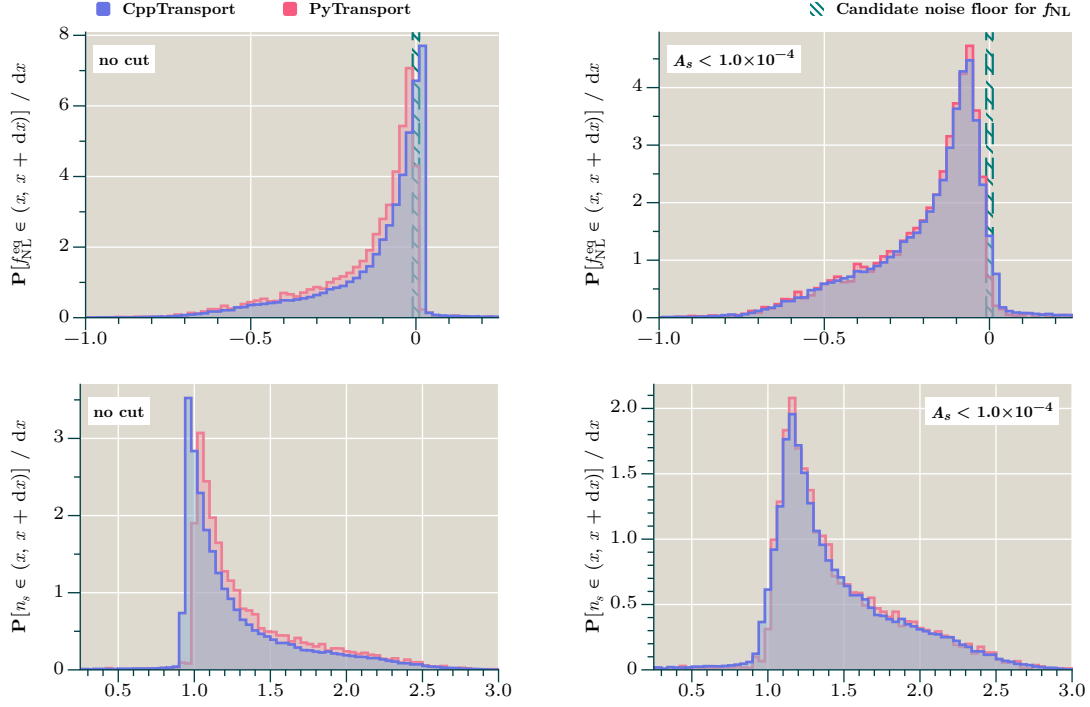


Figure 3. Comparison of distributions for $f_{\text{NL}}^{\text{eq}}$ and n_s derived from the **CppTransport** (blue) and **PyTransport** (red) pipelines. Before cutting on A_s , the **CppTransport** distributions contain 90,039 trajectories and the **PyTransport** distributions contain 22,453 trajectories. **Left column:** no cuts applied. The distributions are qualitatively similar but disagree in detail. **Right column:** applying the cut $A_s < 10^{-4}$ brings the distributions into agreement. The green hatched region is common to Figs. 3, 4 and 13. Its interpretation is described in the second bullet point on p. 41.

better than 0.5% for the three-point correlation amplitudes. We should regard these as a lower limit on the implementation error for individual trajectories in the catalogue.

Catalogue-level agreement.—Second, to test agreement at the level of the catalogue as a whole, we construct a ‘small’ **PyTransport** catalogue using the same ϕ_{UV} , Δ_{max} , initial conditions and parameter priors used to construct our primary catalogue. In the left-hand column of Fig. 3 we show the resulting distributions of $f_{\text{NL}}^{\text{eq}}$ and n_s for **CppTransport** (blue) and **PyTransport** (red). They are qualitatively similar but different in detail. For both observables the most obvious difference is the change in amplitude and location of the peak. In the right-hand column we show the same distributions with the cut $A_s > 10^{-4}$. The amplitude and location of each peak, and the structure of the tails, now show excellent agreement.

A similar effect can be achieved by cutting out trajectories for which $|f_{\text{NL}}^{\text{eq}}| \lesssim 3 \times 10^{-2}$. This removes the region around the peak of the distribution for $f_{\text{NL}}^{\text{eq}}$, and (although not obvious from Fig. 3) the resulting transfer of statistical weight into the tails brings the distributions in agreement. The nontrivial outcome (also for the cut on A_s) is that a *single* cut brings multiple distributions into alignment. The underlying reason, to be demonstrated in §4.2.1, is that A_s , n_s and $f_{\text{NL}}^{\text{eq}}$ are all highly correlated in this model. However, choosing

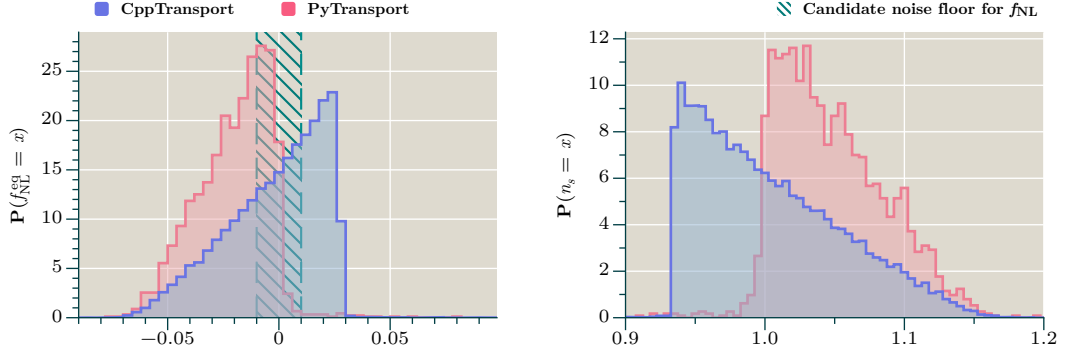


Figure 4. Distribution of $f_{\text{NL}}^{\text{eq}}$ and n_s in the cut region $A_s > 10^{-4}$. **CppTransport** produces a smooth distribution over this range. The apparent falloff near the boundary value $f_{\text{NL}}^{\text{eq}} = -2.8 \times 10^{-2}$ is a binning artefact, whereas the falloff near $f_{\text{NL}}^{\text{eq}} = +2.8 \times 10^{-2}$ is the steep falloff to the right of the peak visible in Fig. 3. In comparison, the peak/cutoff values for the **PyTransport** distribution occur at $f_{\text{NL}}^{\text{eq}} > 0$ and $n_s < 1$. The green hatched region is common to Figs. 3, 4 and 13. Its interpretation is described in the second bullet point on p. 41.

to cut on A_s removes marginally fewer trajectories.

The origin of this discrepancy is not completely clear. In the discussion below we enumerate a number of possibilities that we believe are *not* the cause. In Fig. 4 we plot the distribution of $f_{\text{NL}}^{\text{eq}}$ and n_s in the cut region, which clearly exhibits the difference in structure of the peak. The $f_{\text{NL}}^{\text{eq}}$ and n_s distributions are both characterized by a sharp peak and a one-sided tail. The similarity in shape of the distribution is due to the strong correlation between $f_{\text{NL}}^{\text{eq}}$ and n_s . The ‘missing’ tail is so sparsely populated that there are barely any samples beyond the peak, which therefore serves as a cutoff.

We have considered a number of possible explanations for this discrepancy.

- First, it is not caused by disagreement between the pipelines for trajectories that populate the region $f_{\text{NL}}^{\text{eq}} \gtrsim 0$, $n_s \lesssim 1.0$ where the **PyTransport** pipeline produces almost no statistical weight. Comparison of output from both pipelines shows excellent agreement for trajectories producing observables in this region.
- Second, one could imagine that small values of $f_{\text{NL}}^{\text{eq}}$ are simply unreliable because they are dominated by noise. This explanation has the drawback that it would not naturally explain the disagreement in n_s . However, it is a possible interpretation for the distribution of $\Delta(\text{eq} \rightarrow \text{fold}) \equiv f_{\text{NL}}^{\text{eq}} - f_{\text{NL}}^{\text{fold}}$ in the right-hand panels of Fig. 13 (see below). In a single-field model $|\Delta(\text{eq} \rightarrow \text{fold})|$ should be proportional to n_t [113] and therefore negligible on most trajectories, whereas Fig. 13 shows that it is typically of order 10^{-2} . This might happen if each f_{NL} were contaminated by noise at this level. The different behaviour of **CppTransport** and **PyTransport** could be ascribed to the differing ODE solvers. The green hatched regions in Figs. 3, 4 and 13 indicate the region that should be excluded in this interpretation. Coincidentally it is roughly the same region that must be excluded to bring the distributions reported by each pipeline into agreement.

However, this interpretation does not seem viable. It is clear from Fig. 4 that trajectories for which $f_{\text{NL}}^{\text{eq}}$ falls within the green hatched region form part of a smooth distribution that extends to much larger values of $|f_{\text{NL}}^{\text{eq}}|$. In the noise interpretation we would be obliged to assume that this structure can somehow be ascribed to properties of the noise—and that noise contaminates values of $f_{\text{NL}}^{\text{eq}}$ for which Fig. 13 gives no reason to believe it is significant. In our judgement this does not appear probable.

- Third, the discrepant region is associated with large values of A_s —indeed, much larger than the observationally-allowed window. At sufficiently large A_s the tree-level approximation will break down, making all predictions unreliable [14, 15]. It is *possible* (if perhaps unlikely) that $A_s \approx 10^{-4}$ is already large enough for the leading loop correction to become important, especially if the power spectrum runs to large values on small scales.

While this suggests we should already be skeptical of observables computed from trajectories yielding large A_s , there seems no reason for **CppTransport** and **PyTransport** to fail in different ways if the numerical integration remains under control.

We therefore reject each of these proposed explanations. Instead, we apparently must conclude that the most likely explanation is the performance of the samplers—that is, a systematic difference in the way the pipelines draw parameter combinations leading to trajectories that populate this region. However, we have not managed to identify an error in either pipeline that would cause such a difference. Therefore, to be conservative, we impose the cut $A_s > 10^{-4}$ when discussing observable distributions in §4. In this region there is excellent agreement between the pipelines, and we have good reason to believe that the reported distributions are robust.

In any case, as explained above, this cut (or a similar one) is likely to be required to exclude trajectories for which the tree-level approximation is inadequate. Further work is required to improve our understanding of all these issues.

4 Results

We now present key outputs from our sampling procedure. Agarwal et al. [52] previously discussed the relationship between n_s and r , but the reliability of their predictions was unclear in regions of parameter space where the single-field approximation was insufficient. A subsequent analysis performed by Dias et al. [9] yielded comparable results, but also certain differences of detail. Unfortunately, although their computation was more accurate, their catalogue of 564 inflating trajectories was much smaller. McAllister, Renaux-Petel & Xu [59] considered a significantly larger catalogue, but their primary interest was in the frequency of occurrence of multiple-field effects and they did not report distributions for observables. Relationships involving the observables n_t , $f_{\text{NL}}^{\text{eq}}$, $f_{\text{NL}}^{\text{fold}}$ and $f_{\text{NL}}^{\text{sq}}$ have not yet been studied.

In this section our intentions are twofold. First, we use our primary catalogue of 55,000 trajectories to characterize correlations among the observables A_s , n_s , A_t , n_t , r , $f_{\text{NL}}^{\text{eq}}$ and $f_{\text{NL}}^{\text{fold}}$. This enables us to compare (up to certain ambiguities) with the results of previous analyses. However, despite their convenience, we emphasize that these observables often have

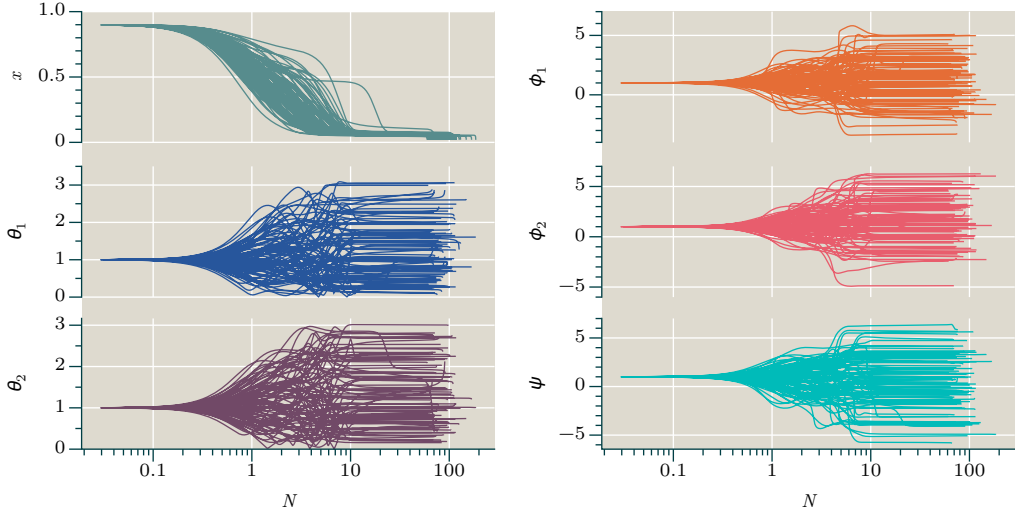


Figure 5. Background evolution for a subsample of 100 realizations. The horizontal scale shows e-folding number N measured from the initial time.

limited utility. A full likelihood analysis is often needed to determine the goodness-of-fit for each trajectory. Second, the small catalogues listed in Table 7 are used to study changes to these distributions when we vary discrete features of the model, such as the truncation of the potential or our choice of initial conditions.

Except for Figs. 17–18, all distributions reported in this section respect the cut $A_s < 10^{-4}$ discussed in §3.3.

4.1 Background evolution and mass spectrum

Field evolution.—In Fig. 5 we plot the evolution of the background fields for a subset of 100 trajectories as a function of e-folding number N measured from $N = 0$ at the initial data. Typical trajectories show very similar evolution for the radial position $x = r/r_{UV}$, characterized by the onset of rapid motion after a few e-folds followed by an extended loitering period as the inflationary potential flattens at small values of x . Very similar behaviour was described by Dias et al. [9]. The angular fields show more variability, but in most cases their values become constant after ~ 10 e-folds. This is an indication that trajectories frequently evolve to an adiabatic limit.

To express this quantitatively we apply the criteria for adiabaticity given in §3.2, according to which a trajectory is adiabatic if each heavy isocurvature mode satisfies $m^2/H^2 > 3$. Before applying any cuts, we find that 64% of trajectories become adiabatic by the end of inflation. For trajectories that respect the cut $A_s < 10^{-4}$ the corresponding figure is 62%. If the adiabaticity condition is relaxed to $m^2/H^2 > 1$ for the heavy eigenstates, the fraction of adiabatic trajectories increases to $\sim 95\%$. These proportions are consistent between our pipelines and appear roughly consistent with the conclusions of previous studies [9, 52, 59].

Mass spectrum.—In Fig. 6 we show the evolution of the mass spectrum over the period of observable inflation. In each panel we overlay histograms for the ordered eigenvalues of

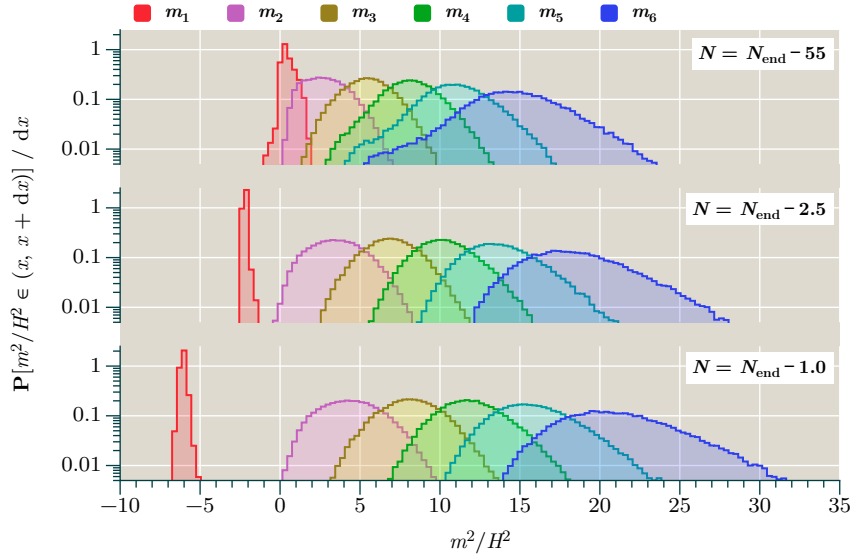


Figure 6. Evolution of the mass spectrum over the period of observable inflation. Each panel contains six histograms showing the distribution of m^2/H^2 for the ordered eigenvalues m^2 associated with the mass matrix. **Top:** 55 e-folds before the end of inflation. **Middle:** 2.5 e-folds before the end of inflation. **Bottom:** 1 e-fold before the end of inflation.

the mass matrix M^A_B given in Eq. (3.6). The top panel shows the mass spectrum 55 e-folds before the end of inflation, which can be regarded roughly as the time of horizon exit for modes contributing to the CMB. The spectrum is relatively closely packed and evenly spaced. The lightest mode is most sharply defined and extends to tachyonic values. The middle and bottom panels show the spectrum at 2.5 e-folds and 1 e-fold before the end of inflation, respectively. In the middle panel, the spectrum is broader and the heavier modes have shifted to slightly higher masses. The lightest mode has become increasingly tachyonic. Similar behaviour was reported in Ref. [59]. Between the middle and bottom panels the distribution of higher-lying heavy modes is stable, but the lightest mode moves even further towards tachyonic values and develops a sizeable gap relative to the rest of the spectrum. This behaviour is expected. On an adiabatic trajectory, $\zeta = \delta\phi/\sqrt{2\epsilon}$ is conserved [29, 30], and ϵ is typically growing near the end of inflation if there is a graceful exit. Therefore $\delta\phi$ must also grow, requiring the adiabatic direction in field-space to be a tachyon. Before applying cuts we find that all trajectories exhibit at least one tachyonic mode at 1 e-fold before the end of inflation, but only 0.2% exhibit a second tachyon.²³ There are no trajectories exhibiting three tachyons. The relative occurrence of two tachyonic modes is essentially the same for trajectories that respect the cut $A_s < 10^{-4}$.

²³One might have some reservations regarding the emergence of multiple tachyonic states with large values of $|m^2/H^2|$ given that our pipeline is based on tree-level codes. In single-field inflation, or multiple-field inflation near an adiabatic limit, this is harmless because ζ is exactly massless and therefore stable (even at loop-level) even though $\delta\phi$ is a tachyon [114, 115]. The situation with multiple tachyons is less clear. In this paper we continue to assume that a tree-level calculation gives an honest representation of the phenomenology, but we note that the issue does not yet appear to have been adequately explored in the literature.

Our mass spectra are in qualitative but not quantitative agreement with Dias et al. [9] and McAllister et al. [59]. These references reported mass spectra near horizon exit for a mode contributing to the CMB. Dias et al. did not discuss the spectrum at later times, whereas McAllister et al. found only mild evolution between horizon exit of CMB modes and the end of inflation. In comparison with Dias et al. the shape of our mass distribution at horizon-exit shows good agreement, but the detailed numerical values of the masses are different. This possibly points to a difference in treatment of the ‘particular integral’ modes (2.42) sourced by bulk fluxes, which contribute significantly to the masses of the heavy eigenstates (see §4.3).

In comparison with McAllister et al. the numerical values of the masses are similar, but the shape of the distribution is different. We reproduce their conclusion that contributions to the mass matrix from mixing with the metric are generally smaller than contributions from the Hessian $\nabla^A \nabla_B V$ when CMB scales are leaving the horizon, although the mixing contributions increase in importance towards the end of inflation and are eventually necessary to keep ζ conserved on an adiabatic trajectory. McAllister et al. observed a mild tachyonic drift of the lightest eigenstate, but at late times the effect is more significant in our realizations. This may be attributable to gravitational mixing. Further, they found that typically the masses m_i^2 of the $i = 3, 4$ and $i = 5, 6$ isocurvature states were degenerate at the level of individual realizations. We do not observe this degeneracy, even if we approximate the mass matrix by the Hessian. This apparently points to an underlying difference in the construction of our potentials, perhaps again caused by a differing treatment of the flux-sourced contributions.

Slow-roll parameters.—In the upper plot of Fig. 7 we plot the distribution of the slow-roll parameters $\epsilon \equiv -\dot{H}/H^2$ and $\eta \equiv d \ln \epsilon / dN$, and their mutual correlation. These parameters are measured at $N = 60$ e-folds prior to the end of inflation, which we denote by the subscript ‘60’. The ϵ_{60} distribution is bimodal. It would be interesting to understand whether this is related to the effect described by Frazer [116] in which peaks in the distribution function of some observable O are related to critical points in the map $O = O(\theta)$ giving O as a function of the field-space coordinates θ on a suitable initial hypersurface.

The main weight of the distribution is centred near $\epsilon_{60} \sim 10^{-10}$, which is just a little larger than the typical value $\epsilon \sim 10^{-12}$ reported by McAllister et al. [59], although their evaluation time was not specified. The secondary peak is near $\epsilon_{60} \sim 10^{-4}$. In comparison, McAllister et al. reported only 7% of samples yielded $\epsilon > 10^{-8}$ and no samples with $\epsilon > 10^{-6}$. In our full catalogue we find $\sim 50\%$ of samples yield $\epsilon_{60} > 10^{-8}$ and $\sim 30\%$ yield $\epsilon_{60} > 10^{-6}$. We find no cases where $\epsilon_{60} > 10^{-3}$. The conclusion is apparently that typical values of ϵ in our catalogue are a few orders of magnitude larger than those reported by Agarwal et al. and McAllister et al. The distribution of ϵ is also broader. This is perhaps related to the inclusion of α in our sampling procedure, which effectively adjusts H while leaving gradients of the potential unchanged.

Ultra slow-roll inflation.—Fig. 7 demonstrates that, while ϵ_{60} is always very small, η_{60} has excursions to large positive and negative values, although rarely as large as $\eta_{60} \approx 6$. This suggests that full-blown ultra slow-roll is unlikely to occur, although there may be periods during which ϵ is being suppressed—albeit less dramatically. Inspection of a subsample of trajectories exhibiting large $|\eta_{60}|$ suggests this is the case. In the lower plot of Fig. 7 we show

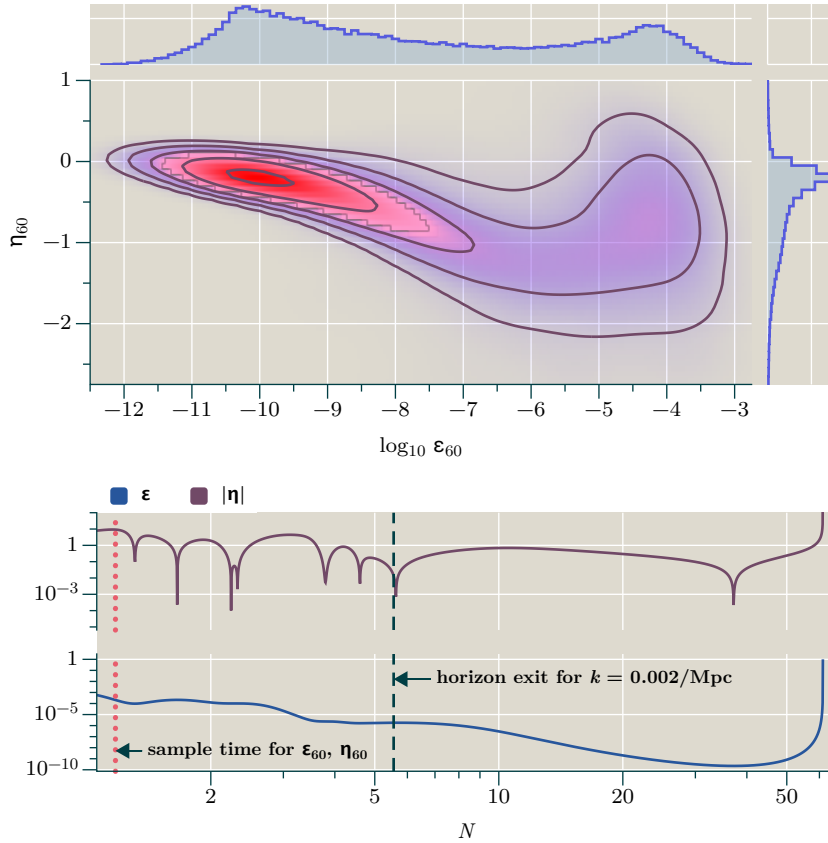


Figure 7. Top: Distribution of the slow-roll parameters ϵ and η at 60 e-folds before the end of inflation, and their correlation. **Bottom:** representative time evolution of the ϵ and η parameters. The vertical green dashed line shows the horizon exit time for $k_* = 0.002 \text{ Mpc}^{-1}$. The vertical orange dotted line shows the time at which we sample ϵ_{60}, η_{60} . The principal features appearing in the plot are typical, including the slow evolution of ϵ to very small values before a rapid increase as inflation ends. On this trajectory $|\eta|$ is briefly ~ 5 for a period of roughly one e-fold just before horizon exit. In general, although excursions to large positive and negative values are present, they are transient.

the time evolution of η for a trajectory belonging to this subsample. Excursions to modestly large $|\eta|$ are present, although on this trajectory they occur before horizon exit of k_* . These excursions are associated with periods during which ϵ decays in a way similar to the ultra slow-roll phenomenology, but less extreme because $|\eta|$ is not as large.

We have not encountered any trajectories for which the behaviour of η clearly supports a diagnosis of full-blown ultra slow-roll. This does not exclude the possibility that, for some trajectories in our catalogue, the initial conditions for observables might be affected by transiently large $|\eta|$. A full analysis of these effects, if they occur, is beyond the scope of this paper. Here we only note that in both the full catalogue and the subsample satisfying WMAP7 constraints on A_s at 3σ , no more than $\sim 5\%$ of trajectories exhibit $|\eta_{60}| > 2$.²⁴ As-

²⁴We use the WMAP7 limits rather than more recent Planck values to simplify comparison with earlier analyses that used WMAP data.

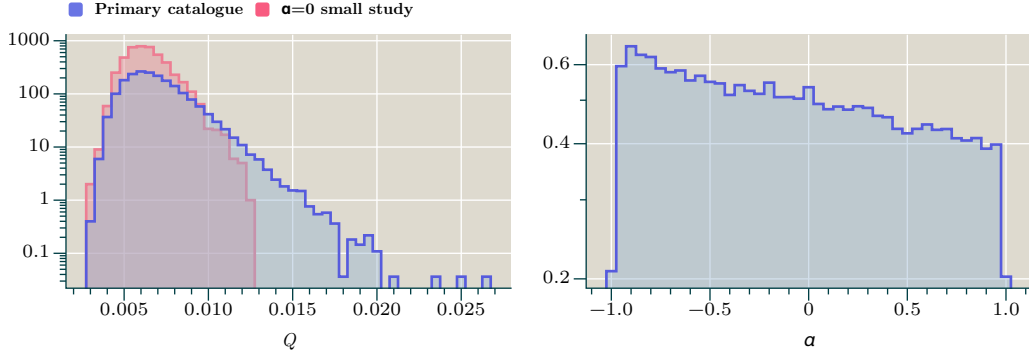


Figure 8. Posterior distributions. **Left:** posterior for Q (blue). The corresponding distribution for the $\alpha = 0$ study (red; see Table 7) is shown for comparison. **Right:** posterior for α .

suming this fraction is representative of the proportion of trajectories that could be affected, ultra slow-roll-like effects appear unlikely to distort the final distribution of observables.

Q parameter and Wilson coefficients.—We now consider the posterior distribution of Q and α , after applying the cut $A_s < 10^{-4}$. (For definitions, see the bottom two lines of Table 1.) Both parameters affect the relative scale of terms in the potential, and therefore influence the likelihood of finding a ‘delicate’ region of field space where the potential is sufficiently flat to inflate.

The left panel of Fig. 8 shows that the probability of obtaining an extended epoch of inflation depends strongly on Q , with successful realizations clustering tightly around $Q \sim 0.006$. This differs from the value $Q \sim 0.04$ reported by Agarwal et al. [52]. However, as explained in that reference, the narrow range of Q for which prolonged inflation can be realized reflects the need to carefully balance Coulomb attraction with repulsion from the bulk contributions for typical values of the Wilson coefficients C_{LM} . Repulsion from the bulk terms scales with Q , and the precise point of balance depends on how many terms are retained. The numerical value of Q therefore has no physical significance. However, the discrepancy supports our suggestion of a systematic difference between typical trajectories in our catalogue and those of Refs. [9, 52]. It is not yet clear whether the difference in Q is caused by the same difference responsible for the difference in typical values of ϵ .

Meanwhile, the α distribution is very roughly flat on both sides of $\alpha = 0$, with a small bias to values near the endpoint $\alpha = -1$ where the constant uplift $V_0 + D_0$ to the vacuum energy disappears. This is a selection effect caused by the cut $A_s < 10^{-4}$. We have already seen that increasing α adjusts H while leaving gradients of the potential unchanged, causing ϵ to decrease. The net result is that \mathcal{P}_ζ must increase. Imposition of an upper limit on \mathcal{P}_ζ will therefore depopulate the high- α part of the distribution.

When comparing with the results of Ref. [52] and Ref. [9] it should be remembered that these references set $\alpha = 0$.²⁵ The $\alpha = 0$ study discussed in Table 7 and §4.3 (also plotted in Fig. 8) confirms that the posterior Q distribution changes when we drop α as a sampling

²⁵Although this is not said explicitly in either reference, we understand it to be the case. We thank Nishant Agarwal for helpful correspondence on this issue.

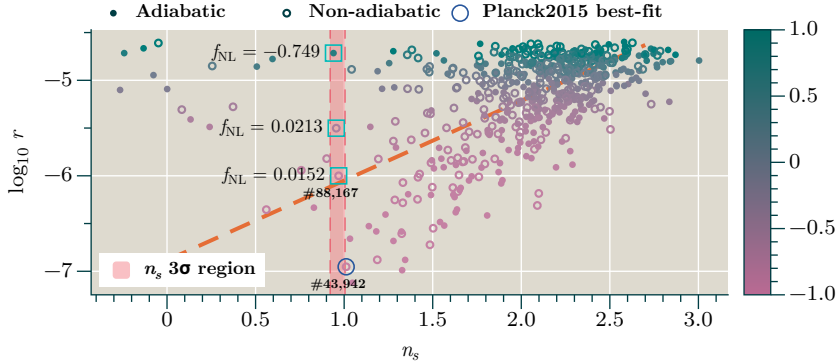


Figure 9. Correlation between r and n_s for the 528 trajectories in our principal catalogue that satisfy the WMAP7 constraint on A_s at 3σ . The points are colour-coded by their value of α . The dashed orange line shows the approximate fit $\log_{10} r \approx -6.78 + 0.785n_s$, computed for the region $0.5 \leq n_s \leq 2.5$. The best-fit trajectory (#43,942) according to the Planck2015 likelihood is highlighted (enclosed in an open circle). We also highlight trajectories whose values of A_s and n_s fall within the WMAP7 bound at 3σ (enclosed in open squares). Trajectories #43,942 and #88,167 are discussed in the text, and are also marked in Figs. 12 and 13. Power spectra for Trajectory #43,942 are given in Fig. 10, and spectra for Trajectory #88,167 are given in Fig. 11.

parameter.

4.2 Two- and three-point observables

We are now in a position to examine the correlation between the summary statistics A_s , A_t , n_s , n_t , r , $f_{\text{NL}}^{\text{eq}}$, $f_{\text{NL}}^{\text{fold}}$ and $f_{\text{NL}}^{\text{sq}}$. To be clear, we recall that these are defined in Eqs. (3.1a)–(3.1b), (3.2), and (3.4). Only the relationship between the scalar spectral index n_s and the tensor-to-scalar ratio r has previously been studied [9, 52].

4.2.1 Two-point observables

Failure of scale invariance and monotonicity.—In Fig. 9 we plot the relationship between n_s and r for the subsample in which A_s is compatible with the 3σ WMAP7 constraint $A_s = (2.43 \pm 0.33) \times 10^{-9}$ [55]. This distribution enables a comparison with previous analyses.

We highlight the WMAP7 3σ region $n_s = 0.963 \pm 0.014$ in red [55, 56]. It is populated only by a handful of trajectories, subject to the caveats mentioned below. This is somewhat surprising. In our other catalogues, the proportion of trajectories that fall within the WMAP7-allowed region is relatively larger, perhaps by a factor of $\mathcal{O}(10)$. Presumably, this happens because the allowed region corresponds to such a small fraction of the model’s large parameter space that our sampling is not entirely representative even with 55,000 trajectories. However, in this paper our aim is not to optimize the fit to current datasets, but to explore the statistical distribution of observables for typical values of the parameters appearing in the Lagrangian. We expect the sampling in these typical regions to be more accurately representative.

In Fig. 9 the trajectories that fall in the allowed region are highlighted by enclosing cyan squares. One of these is adiabatic; the other two are non-adiabatic. The adiabatic

trajectory has an unusually large amplitude of three-point correlations, $f_{\text{NL}}^{\text{eq}} = -0.749$, to be discussed in §4.2.2 below. One might expect the best-fit trajectory to be one of these three. However, according to the Planck2015 $TT+TE+EE$ likelihood, the best-fit is Trajectory #43,942 with log-likelihood $\ln \mathcal{L} \sim -600$. It produces a spectrum for which n_s measured at $k = 0.002 \text{ Mpc}^{-1}$ is marginally blue and does not fall in the WMAP7 3σ -region at all. This trajectory is highlighted by an enclosing dark blue circle. Note that the general trend with α is opposite to the catalogue as a whole, in which increasing α is correlated with *decreasing* $\epsilon \sim r/8$ as explained above. In Fig. 9 the smallest r are correlated with the smallest α .

In Fig. 10 we plot the primordial power spectrum for the best-fit trajectory, together with the corresponding angular spectra C_ℓ^{TT} , C_ℓ^{TE} , C_ℓ^{EE} , and the Planck2015 allowed region at 1σ [96]. In Fig. 11 we plot the same quantities for Trajectory #88,167, which is one of the non-adiabatic trajectories that falls in the WMAP7 3σ region for A_s and n_s . For ease of comparison these trajectories are labelled in Figs. 9, 12 and 13.

The situation is clear. Fig. 11 demonstrates that Trajectory #88,167 produces a scale dependent, non-monotonic power spectrum. Its form is similar to a portion of the characteristic non-monotonic shape emphasized by Dias et al. [9]. Strictly, the angular spectra C_ℓ^{XY} computed from this primordial spectrum are unreliable, because $\mathcal{P}_\zeta(k)$ will be modified by quenching of isocurvature modes before it is communicated to the CMB. However, for the present discussion this is not of primary concern. What *is* important is that the apparent near scale invariance suggested by measurement of n_s at $k = 0.002 \text{ Mpc}^{-1}$ is evidently fictitious; in fact, n_s varies significantly over the observable range. Our estimates for the C_ℓ show that this trajectory significantly overpredicts the correlation amplitude for TT and EE .

Conversely, the best-fit trajectory #43,942 produces a nearly featureless power-law spectrum over the entire observable range of k ; only a very small running is visible for $k \lesssim 10^{-4} \text{ Mpc}^{-1}$. From the inset zoom panel in TT it can be seen that although the overall fit is good, the trajectory very slightly overpredicts the amplitude near the third peak, but (not shown) underpredicts near the first peak—as might be expected for a blue primordial spectrum. It is probable that further trajectories can be found that yield an even better fit. Dias et al. already observed that nonmonotonic $\mathcal{P}_\zeta(k)$ occur relatively frequently in this model due to the characteristic behaviour of ϵ as trajectories roll towards, through and away from the inflexion point. We discuss this in more detail on p. 52 below. To correctly assess the goodness-of-fit for these examples we cannot rely on summary statistics such as A_s and n_s , but instead require a realistic likelihood calculation.

Note that because H is usually close to constant while observable scales are leaving the horizon, the tensor power spectrum is commonly featureless. Therefore r will inherit scale dependence from $\mathcal{P}_\zeta(k)$, and—if it were not so small—predictions for the observability of gravitational waves would also require careful treatment.

n_s - r correlation.—Fig. 9 should be compared with Fig. 9 of Agarwal et al. [52] and Fig. 17 of Dias et al. (arXiv version 2) [9]. The same qualitative features are visible in all these plots, but there are quantitative differences. In Fig. 9 the general trend is for larger values of n_s to be correlated with larger values of r , with no clear separation between adiabatic and non-adiabatic trajectories. The samples fill out a wedge-shaped region, producing considerable

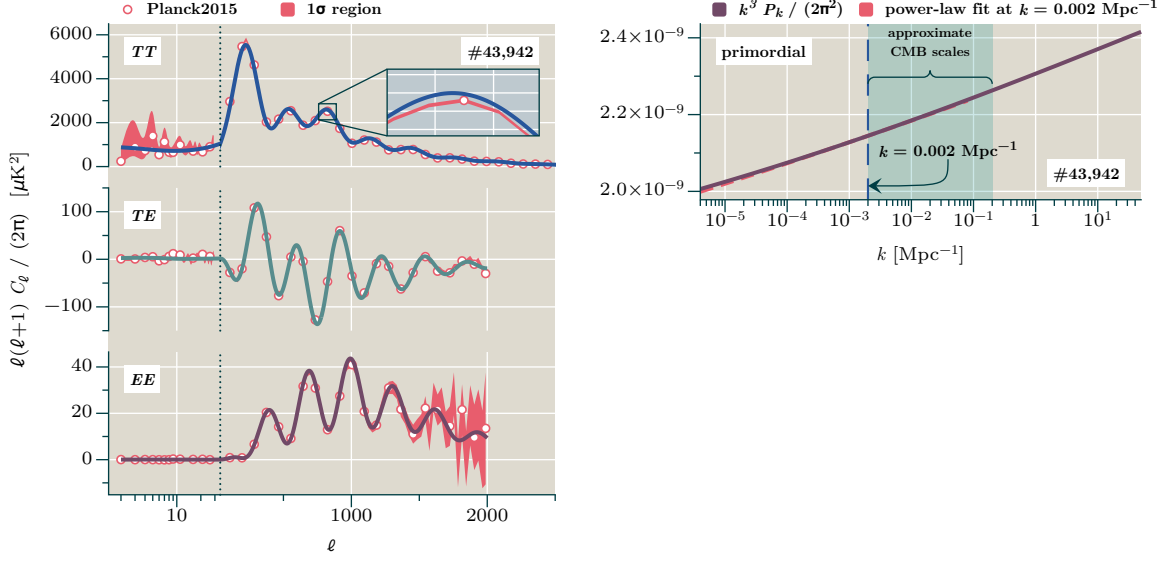


Figure 10. Power spectra for our best fit trajectory #43,942. **Left:** angular spectra C_ℓ^{TT} , C_ℓ^{TE} and C_ℓ^{EE} for the temperature and E -mode fluctuations, and their cross-correlation. **Right:** primordial dimensionless power spectrum $\mathcal{P}_\zeta(k) = k^3 P(k)/(2\pi^2)$. The power-law fit at $k = 0.002 \text{ Mpc}^{-1}$ is marked. Note that the primordial spectrum has very little running, and is accurately given by the power-law fit over a wide range $10^{-6} \text{ Mpc}^{-1} \lesssim k \lesssim 50 \text{ Mpc}^{-1}$. The green shaded region highlights the scales $0.002 \text{ Mpc}^{-1} \lesssim k \lesssim 0.2 \text{ Mpc}^{-1}$ that (approximately) contribute significantly to the angular power spectrum for $\ell \lesssim 2000$.

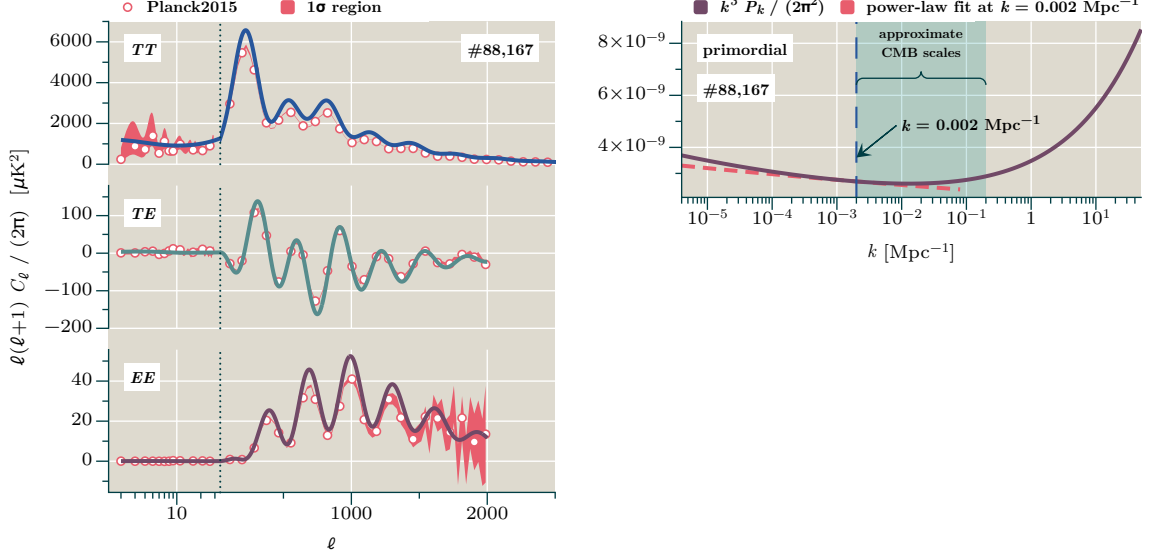


Figure 11. Power spectra for Trajectory #88,167. The left and right panels match Fig. 10.

scatter for very red values of n_s . Most trajectories cluster in the opposite limit near $n_s \approx 2$, where the spectrum is very blue. These trajectories have an unfavourable CMB likelihood.

In Agarwal et al. the observed values of n_s cover $0.93 \lesssim n_s \lesssim 1.10$ and the corresponding

values of r cover $-14 \lesssim \log_{10} r \lesssim -11$. Our values of n_s are typically rather more blue, which could be attributed to the single-field approximation used by Agarwal et al. In Dias et al. [9] the corresponding range of r is not clear because of the choice of axes, but is plausibly $-9 \lesssim \log_{10} r \lesssim -7$; the authors of Ref. [9] did not comment on the discrepancy with Ref. [52]. Our range of r is different again but closer to Dias et al., spanning roughly $-4.6 \lesssim \log_{10} r \lesssim -7.0$. The reason for this substantial variation in r between different analyses is not clear. Trajectories with small ϵ in the range $-12 \lesssim \log_{10} \epsilon \lesssim -10$ are present in our catalogue, which would correspond to values of $\log_{10} r$ much closer to those of Agarwal et al. However, they are associated with A_s that are outside the observable window. The $\alpha = 0$ study discussed in §4.3 suggests that the distribution of observables is not significantly affected by our inclusion of $\alpha \neq 0$ during sampling, so the discrepancy is apparently caused by a structural difference in the potential or a difference in sampling methodology.

One possible explanation is variation of the energy scale at which the brane ‘loiters’ near the inflexion point in its potential. The inflexion point is itself a consequence of delicate cancellations between the attractive Coulomb force and repulsive bulk contributions, and (as has already been said) the exact location of the balance point depends on the treatment of the bulk terms. Small changes to the cancellations that produce the inflexion point could perhaps change the corresponding value of V significantly.

Second, we sample parameters at the fixed scale $k_\star = 0.002 \text{ Mpc}^{-1}$, yielding a range of horizon-exit times corresponding roughly to $55 \lesssim N_\star \lesssim 57$, where N_\star measures horizon exit of the scale k_\star in terms of e-folds prior to the end of inflation. Agarwal et al. reported values at the fixed horizon exit time $N_\star = 60$ [52], and Dias et al. used $N_\star = 55$ [9]. For slow-roll inflation such small shifts in the evaluation time often lead only to small shifts in observables, but in this model the character of the trajectories can change depending on the relative position of the initial conditions and the inflexion point. (For example, compare the power spectrum for Trajectory #88,167 given in Fig. 11.) A systematic difference in the evaluation point could perhaps modify statistical properties of the observables.

Finally, Agarwal et al. used a simple single-field approximation to compute A_s which will produce unreliable estimates where multiple-field effects are significant. We have already noted that the same applies to the spectral index, especially if the power spectrum is not close to scale invariance. This may explain the different range of n_s observed between our catalogues. To decide which of these possible causes, if any, contribute significantly to the differences in the n_s – r relation would require a forensic analysis of each implementation, which is beyond the scope of this paper. We comment further on these issues in §5.

Moving beyond the difference in normalization, the form of the n_s – r relationship is qualitatively similar in all analyses. In Agarwal et al. the correlation is tightest and the relationship is approximately linear. In Dias et al. and our Fig. 9 the correlation is compatible with linearity, but there is considerable scatter and it is not clear that other functional forms are excluded. Assuming linearity, however, the slope of the relationship differs between analyses with our Fig. 9 being shallowest and Dias et al. being steepest.

Red and blue spectral indices.—The majority of our trajectories yield blue spectral indices, although Figs. 10 and 11 show that any numerical value for n_s should be interpreted with

care. The same effect was reported by Agarwal et al. [52], Dias et al. [117] and McAllister et al. [59], who all observed that when $\epsilon \ll 1$ (which is the case in the vicinity of the inflexion point), the spectral index inherits its sign from V'' , where $'$ denotes a derivative in the adiabatic direction in field space. Therefore, modes leaving the horizon before the inflexion point are blue-tilted, whereas those leaving the horizon after the inflexion point are red-tilted. This is one cause of non-monotonicity in the power spectrum.

Agarwal et al., Dias et al. and McAllister et al. noted that this effect limited the number of trajectories producing red n_s , because it is more difficult to obtain sufficient e-folds of inflation after crossing the inflexion point. Our sample contains populations of trajectories with red and blue values of n_s that conform to these expectations, which is a primary driver for the preponderance of blue values $n_s > 1$ in Fig. 9. We also find a relatively larger population of trajectories yielding red n_s where horizon exit occurs *prior* to crossing the inflexion point, but *before* approaching an adiabatic limit. This invalidates expectations based on the sign of V'' . Further, these trajectories typically pass through a sequence of critical points where slow-roll may not be a good approximation. This population of red- n_s trajectories does not appear to have been identified in previous analyses. However, their spectra clearly cannot be monotonic, so it is not yet clear whether their detailed properties can be observationally acceptable.

Consistency equation.—In single field models the tensor-to-scalar ratio and tensor spectral index are related to leading order in slow-roll by the ‘consistency relation’ $r = -8n_t$ [118, 119]. In multiple-field models this is weakened to an inequality $r \leq -8n_t$, also valid only to leading order in slow-roll and assuming that all modes contributing to ζ are massless²⁶ [74]. This follows from the Cauchy–Schwarz inequality applied to the projection $\zeta = N_{\mathbb{A}} \delta\mathcal{X}^{\mathbb{A}}$ from field fluctuations $\delta\mathcal{X}^{\mathbb{A}} = (\delta X^A, \delta\pi^B)$ onto ζ . In Fig. 12 we plot r against our estimated n_t for trajectories satisfying the WMAP7 bound on A_s at 3σ . The ‘consistency bound’ is represented by the orange dotted line, and is respected by a clear majority of trajectories. A small number of trajectories exhibit marginal transgressions. The most likely explanation is that these are effectively single-field models that *should* lie exactly on the bound, but our procedure for estimating n_t has produced a result that is slightly too small.

In the full catalogue we observe a population of trajectories that exhibit more significant (but still not dramatic) transgression of the ‘consistency bound’. There are several possible explanations of this effect, including misprediction of n_t as suggested above. However, it is also possible that these are trajectories for which the massless approximation fails and the fields become *anticorrelated* at horizon exit, leading to a reduction in the final power spectrum amplitude below what would be predicted based on the adiabatic mode alone. If this reduction is sufficiently dramatic it could cause a violation of the massless consistency bound.

This anticorrelation was observed by McAllister et al., who described it as ‘destructive

²⁶The massless condition was not discussed in Ref. [74] and has frequently not been stated in the literature, but it is required. In the analysis of Ref. [74] it appears in the assumption that the scalar two-point function is proportional to the kinetic mixing matrix. This need not be true if the fields have a non-negligible mass matrix, as may be the case in the D3/ $\overline{\text{D3}}$ model. For a similar discussion from a different perspective, see §4.3.4 of Ref. [59].

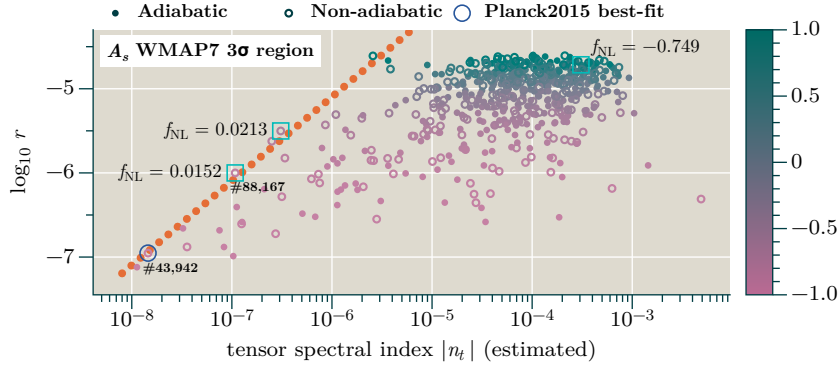


Figure 12. Tensor-to-scalar ratio r against n_t for trajectories satisfying the WMAP7 constraint on A_s at 3σ . The orange dotted line shows the consistency ‘bound’ $r = 8|n_t|$, and the points are colour-coded by their value of α . The best-fit trajectory is highlighted with a large open circle, as in Fig. 9.

interference’ [59]; see the discussion in §4.3.4 of this reference. Our results apparently reproduce their observations. After performing ‘by hand’ fits to the tensor power spectrum in order to obtain the most accurate possible measurements of n_t , we find that residual violations of the consistency bound are no more than a few percent. It is not yet clear whether this is a genuine effect caused by violation of the massless condition, or is simply an unmodelled error in fitting to the tensor power spectrum. To produce a convincing demonstration of violation of the consistency bound, or otherwise, would require an investment in higher-quality numerical computations of the tensor spectral index. It would be interesting to return to this question in future work.

4.2.2 Three-point correlations

Equilateral and folded configurations.—Next consider the amplitude of three-point correlations, measured by $f_{\text{NL}}^{\text{eq}}$ and $f_{\text{NL}}^{\text{fold}}$, which represent the major new results presented in this paper. (Recall that we sample these quantities at a fixed scale $k_t = 3k_* = 3 \times 0.002 \text{ Mpc}^{-1}$. For details of our observables, see §3.1.1.) In general $f_{\text{NL}}^{\text{eq}}$ and $f_{\text{NL}}^{\text{fold}}$ need have no simple relation, but in a single-field model they are connected by Maldacena’s formula²⁷

$$f_{\text{NL}}(k_1, k_2, k_3) = -\frac{5}{12}(n_s - 1) + g(k_1, k_2, k_3)n_t, \quad (4.1)$$

where $g(k_1, k_2, k_3)$ is a calculable function of the momenta k_i [113], but does not depend on slow-roll parameters or other model-dependent data. Hence, in a single-field model, the ‘residual’ $\Delta(\text{eq} \rightarrow \text{fold}) \equiv f_{\text{NL}}^{\text{eq}} - f_{\text{NL}}^{\text{fold}}$ is proportional to n_t multiplied by a fixed factor depending only on the momentum configuration.

In Fig. 13 we plot $f_{\text{NL}}^{\text{eq}}$ and $f_{\text{NL}}^{\text{fold}}$ for trajectories that satisfy the WMAP7 constraint on A_s within 3σ . As in Figs. 9 and 12 the points are colour-coded by their value of α , with values

²⁷Compare Eq. (4.9) of Maldacena, arXiv version 5 [113]. Note there is a sign flip of f_{NL} between this equation and Eq. (4.1), because Ref. [113] defined f_{NL} with the opposite sign convention.

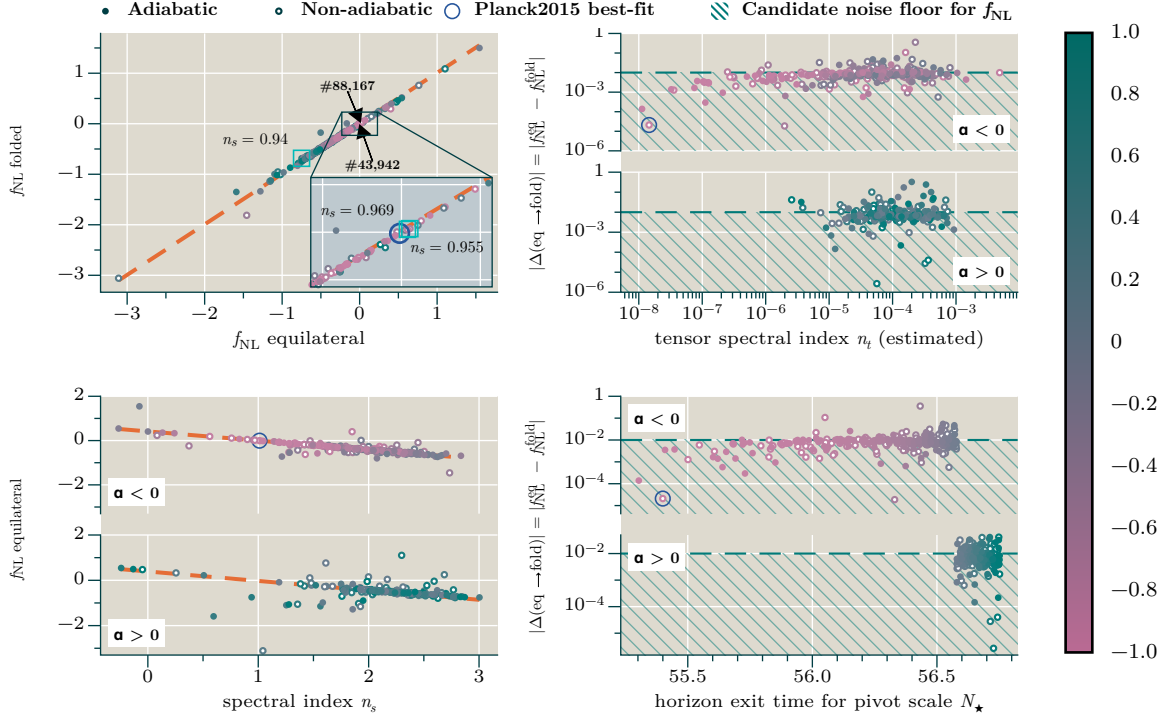


Figure 13. Relation between three-point correlation amplitudes in equilateral and folded configurations with $k_t = 3k_* = 3 \times 0.002 \text{ Mpc}^{-1}$. (For details of the three-point configurations we sample, see §3.1.1.) Plotted points correspond to trajectories that satisfy the 3σ WMAP7 constraint on A_s . Except in the top-left panel, the populations with $\alpha > 0$ and $\alpha < 0$ are plotted separately to aid comparison. **Top left:** $f_{\text{NL}}^{\text{fold}}$ against $f_{\text{NL}}^{\text{eq}}$. The dashed orange line has the functional form $f_{\text{NL}}^{\text{fold}} = a + f_{\text{NL}}^{\text{eq}}$, where $a = 8.3 \times 10^{-3}$ is fit to the measured values with correlation coefficient $R > 0.995$. **Bottom left:** $f_{\text{NL}}^{\text{eq}}$ against n_s . The dashed orange line has functional form $f_{\text{NL}}^{\text{eq}} = b - (5/12)(n_s - 1)$ as in Eq. (4.1). For $\alpha > 0$ we find $b = -0.0270$ and for $\alpha < 0$ we find $b = -0.00286$. **Top right:** the ‘residual’ $|\Delta(\text{eq} \rightarrow \text{fold})| \equiv |f_{\text{NL}}^{\text{eq}} - f_{\text{NL}}^{\text{fold}}|$ against n_t (estimated from ϵ_{60} as described in §3.1.2). **Bottom right:** $|\Delta(\text{eq} \rightarrow \text{fold})|$ against N_* , where N_* measures the horizon exit time (in e-folds before the end of inflation) of the pivot scale $k_* = 0.002 \text{ Mpc}^{-1}$. The interpretation of the green hatched region was discussed in §3.3. **Colour bar:** in each panel, points are colour-coded by their value of α . In all four panels the best-fit trajectory is highlighted as in Figs. 9–12.

near $\alpha = +1$ coded green and values near $\alpha = -1$ coded purple. Previous analyses have assumed $\alpha = 0$. We highlight the Planck2015 $TT+TE+EE$ best-fit trajectory, described above, which has small amplitudes $f_{\text{NL}}^{\text{eq}} \approx -4.73 \times 10^{-3}$ and $f_{\text{NL}}^{\text{fold}} \approx -4.75 \times 10^{-3}$. We will see below that these values are typical when both A_s and n_s fall in the observationally-allowed window.

The top-left panel of Fig. 13 shows tight correlation between $f_{\text{NL}}^{\text{fold}}$ and $f_{\text{NL}}^{\text{eq}}$, as would be predicted by (4.1). In single-field cases the small scatter is due to the smallness of n_t . However, even in cases where multiple-field effects are important, this panel shows that $f_{\text{NL}}^{\text{eq}}$ and $f_{\text{NL}}^{\text{fold}}$ remain highly correlated. This correlation does not depend significantly on α and is a consequence of the bispectrum ‘shape’ usually being close to local [120], which makes

$f_{\text{NL}}(k_1, k_2, k_3)$ nearly independent of configuration. However, the scatter is larger over the full catalogue, showing that three-point correlations do not always have an exactly local shape when A_s is not in the observational range.

The bottom-left panel shows $f_{\text{NL}}^{\text{eq}}$ as a function of n_s . For ease of comparison we break out the populations $\alpha > 0$ (bottom plot) and $\alpha < 0$ (top plot) separately. In both cases a group of effectively single-field trajectories is visible that accurately match the dashed orange lines, each of which is chosen to have the slope $-5/12$ predicted by (4.1). This is especially clear for small values of n_s , where almost all points cluster close to the line. For larger values of n_s the scatter becomes more significant, especially for $\alpha > 0$, and may indicate that multiple-field effects are relevant in this region. Even here, however, the $-(5/12)(n_s - 1)$ dependence predicted by (4.1) is strikingly well reproduced. Clearly, this dependence is the principal driver for large values of $|f_{\text{NL}}|$. A notable exception is the single adiabatic trajectory in the WMAP7 3σ regions for both A_s and n_s (see Fig. 9). This has $n_s - 1 \approx -0.06$ but a large amplitude $f_{\text{NL}}^{\text{eq}} = -0.749$, derived from an abrupt change of angular minimum to be discussed in §4.2.4. However, the plot shows that examples of this kind are relatively rare.

In the top-right panel we plot the absolute value of the ‘residual’ $|\Delta(\text{eq} \rightarrow \text{fold})|$ as a function of our estimated n_t . To be clear, we repeat that these are computed using the analytic approximation $n_t = -2\epsilon_{60}$. According to Eq. (4.1), $|\Delta(\text{eq} \rightarrow \text{fold})|$ should be proportional to n_t , which on logarithmic axes would correspond to a line with unit slope. This is *not* what we find; instead, $|\Delta(\text{eq} \rightarrow \text{fold})| \approx 10^{-2}$ is roughly constant, independent of n_t . Here there is a clear segmentation of the populations $\alpha \gtrless 0$. The $\alpha > 0$ population has more scatter and is restricted to $n_t \gtrsim \times 10^{-6}$. The $\alpha < 0$ population extends (with decreasing density) to $n_t \sim 10^{-8}$ with roughly constant amplitude.

The possibility that this behaviour is caused by contamination from numerical noise was rejected in §3.3. Instead, we must apparently attribute it to multiple-field effects. The size of the effect is comparable to the running from equilateral to squeezed configurations to be discussed in §4.2.3 below, which is consistent with a multiple-field origin.

Finally, the bottom-right panel shows $|\Delta(\text{eq} \rightarrow \text{fold})|$ as a function of N_\star , the horizon-exit time for $k_\star = 0.002 \text{ Mpc}^{-1}$. The structure is very similar to the top-right panel, but the segmentation is even clearer with each population confined to nearly exclusive regions. The $\alpha > 0$ population is restricted to $56.6 \lesssim N_\star \lesssim 56.8$, whereas the $\alpha < 0$ population is restricted to the wider range $55.3 \lesssim N_\star \lesssim 56.6$.

Amplitude distribution for $|f_{\text{NL}}|$.—A key question is the typical amplitude of $f_{\text{NL}}(k_1, k_2, k_3)$ on observationally accessible configurations, because this determines whether non-Gaussian effects are detectable. In Fig. 14 we plot distribution functions for $|f_{\text{NL}}^{\text{eq}}|$. (We do not give separate distributions for $f_{\text{NL}}^{\text{fold}}$ because Fig. 13 shows it to be highly correlated with $f_{\text{NL}}^{\text{eq}}$.)

Fig. 9 shows that many trajectories yield $n_s \approx 2$, so the estimate $f_{\text{NL}} \approx -(5/12)(n_s - 1)$ suggests we should expect a concentration near $f_{\text{NL}} \approx -0.8$. It should be borne in mind that bispectra satisfying this estimate will be strongly scale dependent whenever the spectrum, and likewise n_s , are strongly scale dependent.

This expectation is approximately borne out the detailed distribution for $|f_{\text{NL}}^{\text{eq}}|$ given in the left panel of Fig. 14. For the minimal cut $A_s < 10^{-4}$ (blue), the distribution is rather flat

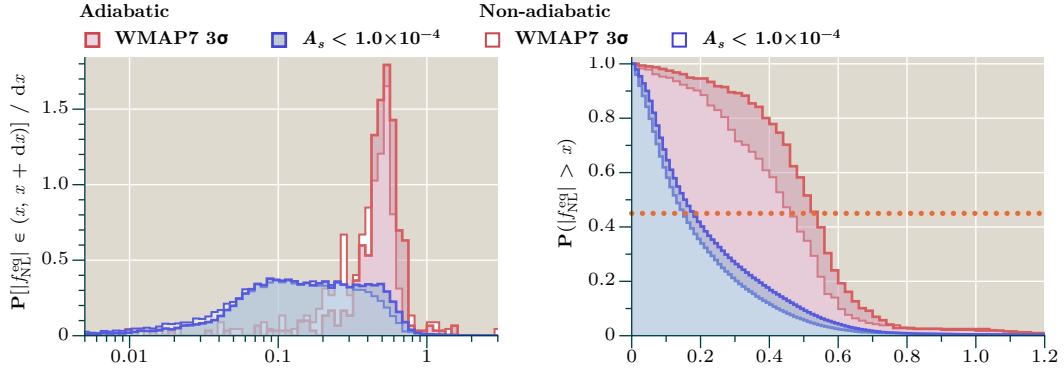


Figure 14. Distribution functions for $|f_{\text{NL}}^{\text{eq}}|$. **Left:** probability density function $\mathbf{P}[|f_{\text{NL}}^{\text{eq}}| \in (x, x + dx)]/dx$ for different cuts on the catalogue. The blue histogram applies the minimal cut $A_s < 10^{-4}$. The red histogram represents the subsample of trajectories satisfying the WMAP7 constraint on A_s at 3σ . **Right:** Tail distribution $\mathbf{P}(|f_{\text{NL}}^{\text{eq}}| > x)$, measured using different cuts on A_s . The orange horizontal dotted line marks the point where $\mathbf{P}(|f_{\text{NL}}^{\text{eq}}| > x) = 0.45$, which for the WMAP7 cut corresponds roughly to $|f_{\text{NL}}^{\text{eq}}| > 0.5$.

for $0.1 \lesssim |f_{\text{NL}}^{\text{eq}}| \lesssim 0.6$. There is a gently decaying tail to smaller absolute values, and more abrupt decay for larger values. There is almost no weight in the distribution for $|f_{\text{NL}}^{\text{eq}}| > 0.8$, as can be seen by comparison with the right panel showing the tail distribution.

For the subsample of trajectories that satisfy the WMAP7 constraint on A_s at 3σ (red), the distribution is clustered in the region $0.5 \lesssim |f_{\text{NL}}^{\text{eq}}| \lesssim 0.6$, as suggested by the distribution for n_s . The tail to low absolute values $|f_{\text{NL}}^{\text{eq}}| \lesssim 0.1$ is heavily depopulated and there are only a handful of samples for which $|f_{\text{NL}}^{\text{eq}}| \gtrsim 1$. In the right-hand panel, the orange horizontal dotted line marks the point where $\mathbf{P}(|f_{\text{NL}}^{\text{eq}}| > x) = 0.45$, chosen because for the WMAP7 sample it corresponds roughly to $|f_{\text{NL}}^{\text{eq}}| > 0.5$. In the full catalogue $|f_{\text{NL}}^{\text{eq}}|$ exceeds 0.5 much less frequently, in no more than 8% of cases. This reflects an approximate trend within our catalogue (already mentioned in §3.3), that larger values of A_s are correlated with smaller values of f_{NL} .

Unfortunately these large $|f_{\text{NL}}|$ can not be regarded as an observable signature in our own universe, because they derive from values of $n_s - 1$ of order unity. For trajectories that satisfy observable constraints on *both* A_s and n_s , it appears that $|f_{\text{NL}}|$ will typically be small—as is the case for our best-fit trajectory.

4.2.3 Squeezed configurations

Finally, we turn to squeezed configurations. In Appendix B we show that modestly squeezed isosceles configurations with $\beta = 0.9$ and $\beta = 0.95$ (corresponding to squeezings $k_3/k_t = 0.05$ and 0.025 , respectively) require integration times in the range 1,000 s to 2,000 s. Taking the CMB to receive contributions from approximately 0.005 Mpc^{-1} to 0.2 Mpc^{-1} , the maximum observable squeezing is roughly $k_3/k_t \approx 0.0125$ or $\beta \approx 0.975$. Therefore these estimates can be taken as a reasonably reliable lower limit on the compute time required for predictions in the observational range. This would increase processing time for the entire catalogue by a factor

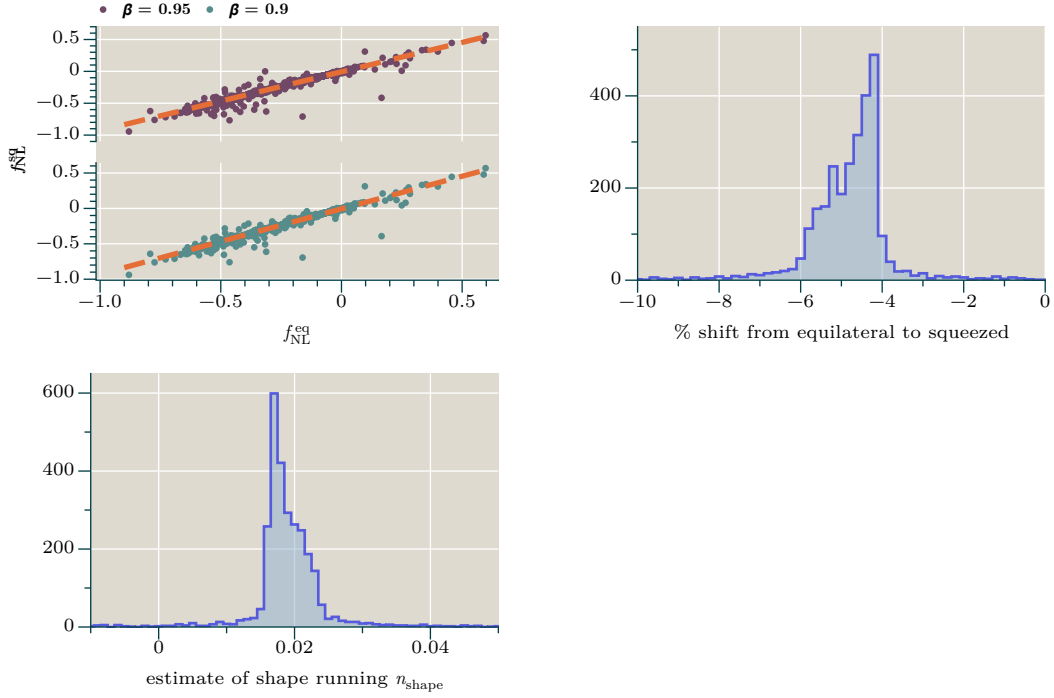


Figure 15. Analysis of the squeezed amplitude $f_{\text{NL}}^{\text{sq}}$. We impose our standard cut $A_s < 10^{-4}$. **Top left:** $f_{\text{NL}}^{\text{sq}}$ against $f_{\text{NL}}^{\text{eq}}$. Green points correspond to $\beta = 0.9$ and squeezing $k_3/k_t = 0.005$. Brown points correspond to $\beta = 0.95$ and squeezing $k_3/k_t = 0.0025$. The dashed line has approximate form $f_{\text{NL}}^{\text{sq}} = -0.006 + 0.92f_{\text{NL}}^{\text{eq}}$, which is common for both squeezings. **Bottom left:** Distribution of the estimated ‘shape running’ parameter n_{shape} . **Top right:** Distribution of percentage shift between $f_{\text{NL}}^{\text{eq}}$ and $f_{\text{NL}}^{\text{sq}}$ for $\beta = 0.95$

perhaps in the range 3 to 5, which is prohibitive given the already sizeable computational demands for obtaining observables.

Gelaton and QSFI effects.—Instead, we study the relationship between $f_{\text{NL}}^{\text{sq}}$ and $\{f_{\text{NL}}^{\text{eq}}, f_{\text{NL}}^{\text{fold}}\}$ on a smaller sample of roughly 3,000 trajectories. In the top-left panel of Fig. 15 we plot the computed value of $f_{\text{NL}}^{\text{sq}}$ against $f_{\text{NL}}^{\text{eq}}$ for trajectories that satisfy the WMAP7 bound on A_s at 3σ . As expected this shows strong correlation, which applies equally to the full catalogue satisfying $A_s < 10^{-4}$. The same conclusion applies to $f_{\text{NL}}^{\text{fold}}$, which itself correlates strongly with $f_{\text{NL}}^{\text{eq}}$. The orange dashed line corresponds to the approximate relation $f_{\text{NL}}^{\text{sq}} = -0.006 + 0.92f_{\text{NL}}^{\text{eq}}$, from which we conclude that the typical amplitude of $f_{\text{NL}}^{\text{sq}}$ is very similar to $f_{\text{NL}}^{\text{eq}}$ but just a little smaller. The characteristic clustering of values between $-0.6 \lesssim f_{\text{NL}}^{\text{eq}} \lesssim -0.1$ is clearly visible (cf. the blue distribution in Fig. 14).

In the top right panel of Fig. 15 we plot the shift $\Delta(\text{sq} \rightarrow \text{eq}) \equiv f_{\text{NL}}^{\text{sq}} - f_{\text{NL}}^{\text{eq}}$ between squeezed and equilateral configurations, expressed as a percentage of the equilateral amplitude. The shift almost always falls between -4% and -6% , with values near -4% being favoured. In absolute values this corresponds to $\Delta(\text{sq} \rightarrow \text{eq}) \approx \text{few} \times 10^{-3}$. In models for which the slow-roll approximation applies throughout, we expect the slow-roll parameters to

set the scale of the shift [113, 121]. For example, in the axion–quadratic model studied in Ref. [15] the shift computed between the same configurations is roughly $\sim \text{few} \times 10^{-2}$, which is comparable to $\eta = d \ln \epsilon / dN$. From this point of view the typical value of Δ observed in the D3/ $\overline{\text{D3}}$ model is not unusually large, and indeed is comparable to η in many realizations (see Fig. 7 and also the discussion of the residual $\Delta(\text{eq} \rightarrow \text{fold})$ above).

It is possible that some of the more significant shifts of 10% or larger are associated with an unusual change in amplitude near equilateral configurations, which might be expected from a ‘gelaton’-like or ‘QSFI’-like scenario [60–62, 122]. Assuming the rate 0.07% suggested by McAllister et al., we would expect to observe perhaps $\mathcal{O}(10)$ QSFI-like examples in a catalogue of this size [59]. It would be exceptionally interesting (but numerically expensive) to compute exact bispectrum shapes for the trajectories that exhibit the largest shifts between equilateral and squeezed configurations.

Shape dependence.—In general the bispectrum may depend on shape and scale through the ratios k_t/k_\star and k_i/k_t for $i = 1, 2, 3$. As we move from equilateral to squeezed configurations, taking \mathbf{k}_3 to be the squeezed momentum, the ‘shape’ ratios k_1/k_t , k_2/k_t vary between $1/3$ and $1/2$. Meanwhile, k_3/k_t varies between $1/3$ and 0.0025 . Assuming the strongest dependence comes from the squeezed momentum, the effective ‘shape’ running can be written in terms of a parameter n_{shape} [121, 123]

$$f_{\text{NL}} \approx f_{\text{NL}}^\star \left(\frac{k_3}{k_t} \right)^{n_{\text{shape}}}, \quad (4.2)$$

where f_{NL}^\star is a fiducial value taken here to be the value of f_{NL} on an equilateral configuration at $k_t = 3k_\star$. In the bottom left panel of Fig. 15 we plot the distribution of n_{shape} for our sample of squeezed configurations. It shows very pronounced clustering near $n_{\text{shape}} \approx 0.02$. The scale dependence of the spectrum is divided out of f_{NL} by construction, but it is possible that this shape dependence is generated by the same underlying process [123, 124]. In particular, the shape of the n_s distribution in Fig. 3 is qualitatively similar to (but not the same as) the distribution of n_{shape} in Fig. 15. One might therefore expect the shape running to be small when the spectrum falls in the observationally-allowed window, but our ‘squeezed’ catalogue contains too few trajectories to make a definitive statement. It would be interesting to study the shape running in a larger sample.

4.2.4 Large non-Gaussianity from rapid change of angular minima

In certain very rare examples we observe the synthesis of large non-Gaussianity, apparently caused by abrupt shifts in the brane trajectory. These occurrence of these rare shifts was recognized by Agarwal et al., who conjectured they might generate appreciable three-point correlations [52]. Our results demonstrate this conjecture to be essentially correct.

Typical evolution.—In Fig. 16 we show the time evolution for a typical trajectory exhibiting a rapid transition between distinct angular minima. In the top-left panel we plot the time evolution of the background fields. The transition occurs at roughly $N \approx 6.8$ e-folds from the initial time (marked by the dotted vertical line) and is characterized by rapid evolution of ϕ_2 and ψ . The motion is overdamped by Hubble friction and the fields settle smoothly

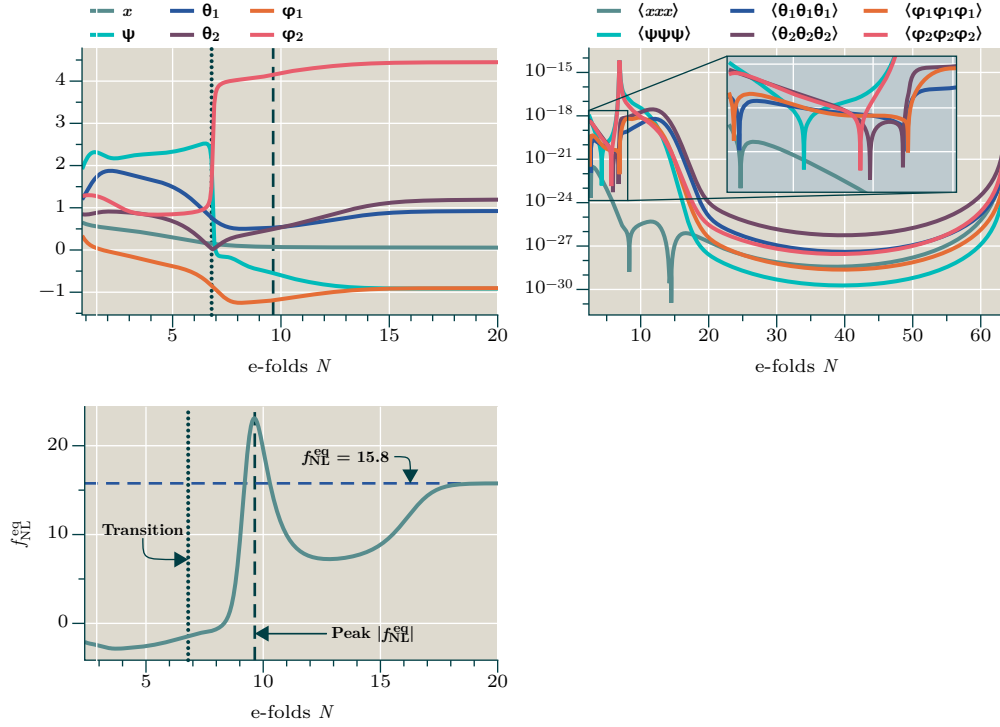


Figure 16. Example trajectory exhibiting rapid transition between angular minima. **Top left:** Evolution of background fields. The dotted vertical line indicates the approximate time of the transition. The dashed vertical line indicates the time at which peak $|f_{\text{NL}}^{\text{eq}}|$ is achieved (see bottom left panel). **Bottom left:** Evolution of $f_{\text{NL}}^{\text{eq}}$ on a scale $k_t/3 = k_\star = 0.002 \text{ Mpc}^{-1}$. The axes match the top left panel, and the approximate transition time and peak $|f_{\text{NL}}^{\text{eq}}|$ are marked in the same way. **Top right:** Time evolution of the dimensionless 3-point functions $(k_1 k_2 k_3)^2 \langle O_1(\mathbf{k}_1) O_2(\mathbf{k}_2) O_3(\mathbf{k}_3) \rangle'$, for selected operators O_i . The prime ' attached to the correlation function denotes that the momentum-conserving δ -function $(2\pi)^3 \delta(\mathbf{k}_1 + \mathbf{k}_2 + \mathbf{k}_3)$ has been removed.

into the new vacuum. After the transition the system approaches an adiabatic limit. The dashed vertical line indicates the time at which maximum $|f_{\text{NL}}^{\text{eq}}|$ is attained.

In the bottom-left panel we show the time evolution of $f_{\text{NL}}^{\text{eq}}$, evaluated on the scale $k_t/3 = k_\star = 0.002 \text{ Mpc}^{-1}$. The amplitudes $f_{\text{NL}}^{\text{fold}}$ and $f_{\text{NL}}^{\text{sq}}$ exhibit qualitatively similar time-dependence, although there are differences of detail. In each of these measures, the amplitude of 3-point correlations exhibits rapid growth after the transition up to a peak at $N \approx 9.6$, followed by rapid decay. Eventually, as the adiabatic limit is reached, the equilateral amplitude asymptotes to $f_{\text{NL}}^{\text{eq}} \sim 15.8$, with slightly different values for the other configurations. We plot the evolution only up to $N = 20$, beyond which the dynamics become uninteresting. For ease of comparison the top-left and bottom-left panels share the same horizontal scale.

This time evolution of $f_{\text{NL}}^{\text{eq}}$ closely matches the behaviour described by Elliston et al., associated with rolling between two approximate critical points of the potential [23]. In this case the critical points should be regarded as the angular minima connected by the rapid transition. Note that Ref. [23] considered only the case of two-field dynamics in which the trajectory rolls from the vicinity of a critical point at which the Hessian has one dominant

negative eigenvalue to the vicinity of a different critical point at which the Hessian has one dominant positive eigenvalue. However, it is plausible that similar behaviour occurs in transitions between critical points with different numbers of positive and negative eigenvalues. This example suggests it may be profitable to develop a general theory of such transitions. For example, the above analysis clearly invites a connexion with the language and methods of Morse theory. To our knowledge, however, this connexion is currently unexplored.

Numerical fidelity.—The abrupt character of the transition requires that we exercise caution before accepting numerical results. We have verified that the solutions are stable to adjustment of the time-sample mesh, numerical tolerances, and changes of stepper. For these trajectories we have compared the output from our Dormand–Prince 4th/5th-order stepper with an adaptive Bulirsch–Stoer stepper that can work up to 8th order where the solution has rapid changes or discontinuities. So far as we can judge, our numerical methods appear to correctly control the solution for each correlation function during the transition. Further, despite the abrupt evolution of the background fields, we have verified that the eigenvalues of the mass matrix evolve smoothly.

In the top-right panel of Fig. 16 we plot the time evolution for a representative sample of field-space correlation functions. These demonstrate that the evolution is smooth and the crucial decay during the subhorizon era is being followed accurately. It is this era that is typically most difficult to integrate, and conversely noise in this region is usually a reliable indicator of numerical problems [14, 15]. For this trajectory there are no significant subhorizon oscillations. Other trajectories *do* exhibit them in off-diagonal correlators $\langle 12 \rangle$ as a consequence of unbalanced phase factors $\sim e^{i(E_1 - E_2)t}$ between states 1 and 2 with energies E_1, E_2 . Where we have performed spot checks on such trajectories, the solutions are stable to the changes described above and the oscillations appear to be smoothly resolved.

Summary.—We caution that trajectories exhibiting these rapid transitions are rare; there is no sense in which they can be regarded as typical features of the D3/ $\overline{\text{D3}}$ model—although, curiously, the single adiabatic trajectory satisfying the (separate) WMAP7 3σ bounds on A_s and n_s is of this type. We observe ten examples of this kind in our primary catalogue for which $|f_{\text{NL}}^{\text{eq}}|$ is larger than unity, although there are certainly more examples that fall below this arbitrary threshold. The cases where $|f_{\text{NL}}^{\text{eq}}| > 1$ correspond to $f_{\text{NL}}^{\text{eq}}$ equal to $-18.7, -12.3, -9.3, -8.71, -8.49, -7.31, 11.0, 12.3, 15.8, 75.8$. Their rarity suggests it is unlikely that observable signatures of these transitions could be used to constrain the model. Nevertheless, despite their atypicality, these trajectories are very interesting as examples of behaviour that has been observed in toy models [23], but not (to our knowledge) in a model motivated by a purpose *other* than its ability to generate large 3-point correlations.

4.3 ‘Small’ ensemble comparisons

We now consider the ‘small’ ensembles produced by the **PyTransport** pipeline. (See Table 7.) In general these show that observational predictions are strikingly insensitive to many of the arbitrary choices made in §2.2. Specifically, we find very little difference between our principal catalogue and the ‘small’ catalogues produced by varying initial conditions, ϕ_{UV} , or the truncation point of the potential. (When varying the initial conditions we do observe

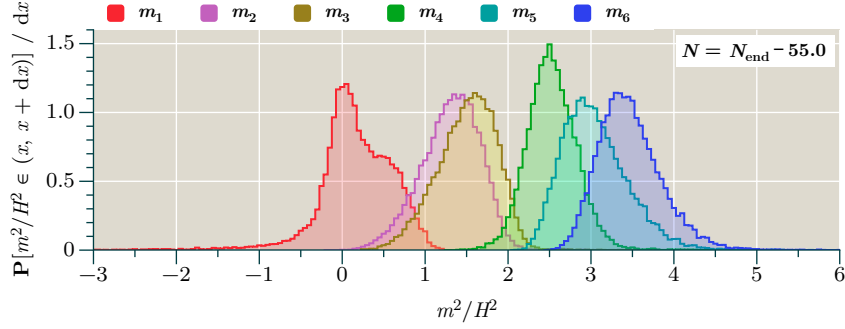


Figure 17. Mass distribution with $\mathcal{C}_{\mathbb{L},\mathbb{M}} = 0$ (see Table 7). Colour assignments correspond to Fig. 6.

a preferred non-zero initial x -velocity of the brane, but this does not propagate into the final distributions.)

Homogeneous model.—Significant changes do occur when dropping contributions to the potential sourced by the bulk flux product $g_s|\Lambda|^2/96$. We describe this as the ‘homogeneous’ case (see Table 7), which corresponds to setting $\mathcal{C}_{\mathbb{L},\mathbb{M}} = 0$. This is an artificial test in the sense that there is no meaningful limit that would justify dropping the $\mathcal{C}_{\mathbb{L},\mathbb{M}}$ while retaining the zero modes of the bulk Laplacian. However, the outcome is still interesting because it illuminates how features of the model arise from particular sectors of the potential.

In Fig. 17 we plot the mass distribution for this catalogue, measured at 55 e-folds prior to the end of inflation. In comparison with Fig. 6 the heavy eigenstates are more nearly degenerate, and their numerical values of m^2/H^2 are significantly smaller. Meanwhile, the tachyonic state (red distribution in Figs. 6 and 17) has a significantly broader tail towards negative values. The conclusion is apparently that the heavy masses are dominated by contributions sourced from the bulk fluxes. It is this feature that causes us to speculate that the difference in mass spectra reported by Agarwal et al. [52], Dias et al. [9] and this work may be associated with differing treatment of these sourced modes. Because the sourced modes also change the distribution of the lightest mass eigenstate, it is possible that they contribute to the difference in ϵ observed between all three studies.

By itself, a change in the spectrum of heavy modes need not imply any shift in the distribution of observables. Therefore in Fig. 18 we plot the distributions for $f_{\text{NL}}^{\text{eq}}$ and n_s in the homogeneous case, without applying a cut on A_s . Although the peak of each distribution remains fixed, the shape and length of the tail is adjusted significantly. We conclude that the impact on observables is modest. However, if treatment of the flux-sourced modes is really responsible for the differences observed between our analysis and Agarwal et al. or Dias et al., it is possible that conclusions at the level of observables may exhibit only limited sensitivity to these differences.

$\alpha = 0$ model.—The last study is the restriction to $\alpha = 0$, for which the posterior Q -distribution was already discussed in Fig. 8. This enables us to connect our analysis with the previous studies reported by Agarwal et al., Dias et al. and McAllister et al., each of which set $\alpha = 0$. We do not observe significant shifts in the distribution of observables, except for a

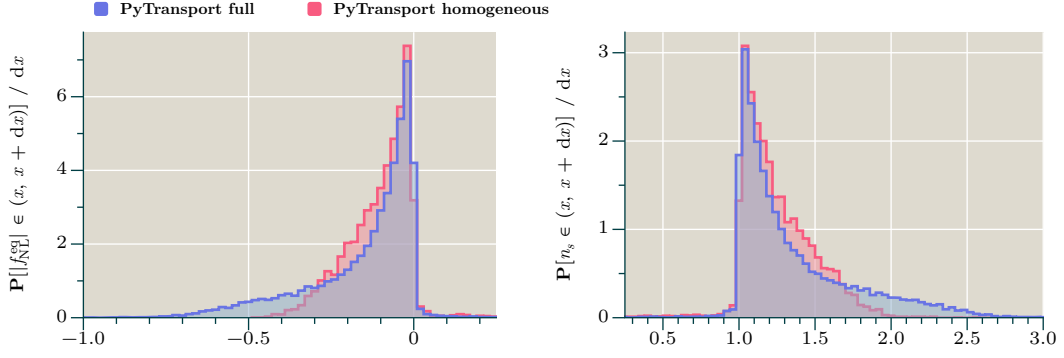


Figure 18. Change in observables for the ‘homogeneous’ catalogue. No cut is applied to A_s . **Left:** distribution of $f_{\text{NL}}^{\text{eq}}$ with the full potential (blue) and in the homogeneous case (red). **Right:** distribution of n_s with the same conventions.

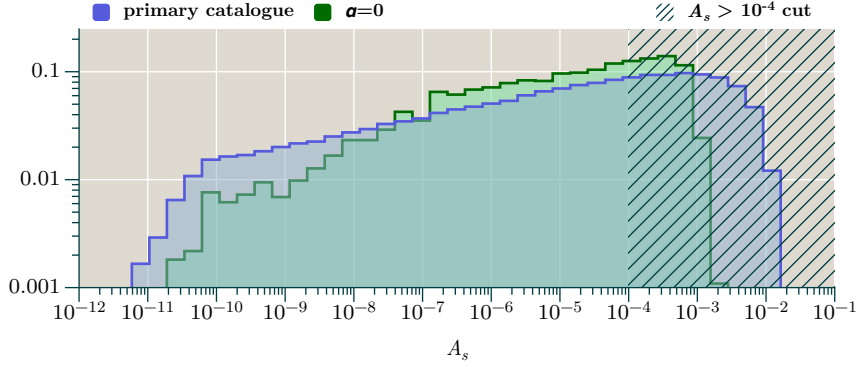


Figure 19. Distribution of A_s in the primary catalogue (blue) and the $\alpha = 0$ ‘small study’ (green). The hatched region indicates the part of the distribution excluded by our cut $A_s < 10^{-4}$.

small shift in the A_s distribution (see Fig. 19). This conclusion was anticipated by Hertog & Janssen [63]. On this basis, it appears that the differences observed between our analysis and these previous studies should be attributed to structural differences in the potential rather than changes in the sampling procedure.

5 Discussion

In this paper we have revisited the ‘delicate’ D3/ $\overline{\text{D3}}$ brane inflationary model, and computed the amplitude of three-point correlations for the density perturbations. These have not previously been reported. We find that $f_{\text{NL}}^{\text{eq}}$, $f_{\text{NL}}^{\text{fold}}$ and $f_{\text{NL}}^{\text{sq}}$ are all highly correlated with nearly degenerate amplitudes close to Maldacena’s single-field prediction $f_{\text{NL}} \approx -(5/12)(n_s - 1)$ for $|n_t| \ll 1$ [113], even when $|f_{\text{NL}}|$ is large. For trajectories that yield observationally acceptable CMB angular spectra C_ℓ^{XY} it follows that the amplitude of three-point correlations is usually negligible. For example, the best-fit trajectory for the Planck2015 $TT+TE+EE$ likelihood yields $|f_{\text{NL}}| \sim 5 \times 10^{-3}$. If the restriction to the observationally acceptable region is dropped,

the model has a tendency to produce scale-dependent, nonmonotonic power spectra with corresponding $|f_{\text{NL}}|$ of order unity.

A small number of trajectories yield atypically large $|f_{\text{NL}}|$, associated with abrupt transitions of the angular fields between different minima. At the extreme, we observe values $|f_{\text{NL}}| = \mathcal{O}(100)$, although still with unacceptable spectral behaviour. Closer to the allowed observational window we find one (adiabatic) trajectory of this type that yields $f_{\text{NL}} = -0.749$ and $n_s = 0.94$ with an acceptable A_s . However, because the spectrum is scale dependent the fit is not as good as these values would suggest. The occurrence of large three-point correlation amplitudes for these trajectories was originally conjectured by Agarwal et al. [52]. The large bispectra observed in our catalogue all appear to be produced by such transitions and not ‘gelaton’ or ‘QSFI’ effects [60, 61, 122]. In our smaller catalogue of squeezed configurations we observe some significant shifts between squeezed and equilateral configurations that could possibly be associated with QSFI behaviour, although the corresponding bispectrum amplitudes do not appear to be large. To decide one way or the other would require full computations of the bispectrum shape on these trajectories. Overall, the shape usually appears close to local, although there are exceptional cases that it would be interesting to explore.

We find only weak dependence on most of the arbitrary choices made during construction of the potential. In particular, we find our observable distributions are robust to variations in initial conditions and the field-space diameter ϕ_{UV} . We find they are also robust to changes in the truncation point of the potential, even for observables derived from the three-point function. This implies that the intrinsic three-body couplings do not play a significant role in setting the amplitude of the bispectrum, which is consistent with the suggestion that the observed large bispectra are sourced by field-space evolution on superhorizon scales associated with transitions between minima. When contributions to the potential sourced by bulk fluxes are dropped we find that the mass distribution changes significantly, but the effect on observables is much more modest. Variation in the treatment of these contributions may be responsible for the observed differences between independent analyses of the model. If so, there is some basis for optimism that predictions for observables (except perhaps r) might be robust.

It is sometimes suggested that $|f_{\text{NL}}| \sim 1$ is a generic prediction of inflationary models in which multiple fields are active [35]. This does appear to be the case for what we could call ‘type 1’ models where the fields are spectators during inflation, but become active in the post-inflationary universe—as in the curvaton, inhomogeneous-end-of-inflation and modulated reheating models [125]. Meanwhile, there is relatively little evidence to guide our expectations for ‘type 2’ models in which the fields are active during inflation, but the evolution becomes adiabatic before reheating. Many toy models of this type produce negligible $|f_{\text{NL}}|$. The D3/ $\overline{\text{D3}}$ model represents a more realistic example of this type, which can be attributed to the frequent emergence of an effectively adiabatic trajectory long before observable scales leave the horizon. To set our expectations for the interpretation of upcoming large galaxy surveys [126], it would be exceptionally interesting to know whether the same conclusion extends to a larger class of multiple-field models motivated by ideas in high energy physics.

In common with all prior analyses, we find the model is not favourable observationally.

Our best-fit trajectory yields a log-likelihood $\ln \mathcal{L} \approx -600$ based on Planck2015 temperature and polarization measurements [97], but most trajectories produce spectra that are significantly too scale dependent—even where the amplitude falls in the allowed range. Typically the bispectrum will also be scale dependent whenever the spectrum is scale dependent. Additionally, there is evidence for a characteristic *shape* running $n_{\text{shape}} \approx 0.02$ in the bispectrum that may possibly be generated from the same source as the scale dependence of the power spectrum. It is not yet clear whether the shape running can be significant when the scale dependence of the bispectrum is small—but, if so, this could be an interesting observational signature.

Our software pipeline depended on development of a new interface between **CppTransport** and **CosmoSIS** [34]. A future release of **CppTransport** is scheduled to include this interface, which can be used with any inflationary model. A similar interface to the more recent **Cobaya** framework [127] is also planned. These interfaces dramatically simplify the construction of end-to-end pipelines to constrain inflationary models directly from data—a capability which has been available for a long time in the collider phenomenology community, but which has taken longer to become mainstream for inflationary model analysis.

To mitigate the risk of implementation errors we deploy two independent pipelines. These show excellent agreement at the level of individual trajectories, but disagree in detail at the level of the entire catalogue. The factors driving this disagreement have not yet been identified, but we believe they relate to the sampling implementation. After applying the cut $A_s < 10^{-4}$ the catalogues are brought into statistical agreement. Because our codes operate at tree-level, a cut of this kind would likely be required anyway to remove trajectories on which there is a risk of the leading loop corrections becoming relevant.

Despite the complexity of the model, compute times are not prohibitive. Samples of the two-point function can be computed in a time of order seconds. They could perhaps be included in a parameter estimation Monte Carlo if not too many samples are needed to correctly predict the shape of the spectrum. Samples of the three-point function are substantially more expensive, with integration times of the order of a few hundred seconds depending on the underlying hardware. Therefore inclusion of this information in a Monte Carlo is impractical for the $D3/\overline{D3}$ model. In simpler models the compute time is much smaller, although even in this more optimistic case it would be necessary to sample the bispectrum sparsely rather than compute its full shape. It is an interesting question whether reliable methods can be developed to incorporate this information in a practical likelihood calculation.

The $D3/\overline{D3}$ model brings other computational challenges. We find that observables derived from the three-point function can require enhanced numerical precision for accurate computation, which is presumably a consequence of roundoff error due to large cancellations between the many intermediate terms that appear in this model. A second example is accurate computation of the tensor spectral index n_t , because the tensor spectrum is extremely flat. Nevertheless, such accurate computations seem worth pursuing because of the possibility that rare trajectories can violate the ‘consistency bound’ $r \lesssim -8n_t$ due to significant anticorrelations imprinted at horizon exit.

Comparison to previous work.—Our results are in qualitative agreement with previous analyses of the model [9, 52, 59]. However there are quantitative differences. In particular there is evidence for some systematic differences between the trajectories in our catalogue and those constructed by Agarwal et al. and McAllister et al. Our typical values of Q and ϵ (and hence r) are somewhat different, and our typical mass spectra have a qualitatively different structure but similar numerical magnitudes. There is also some evidence, although less strong, for similar systematic differences relative to Dias et al.

We have suggested these differences may be related to a different treatment of contributions to the potential sourced by bulk fluxes. There is also our inclusion of α as a sampling parameter, whereas Agarwal et al., Dias et al., and McAllister et al. imposed $\alpha = 0$. This seems to be responsible for some of the shift in the (unobservable) parameter Q , and also slightly broadening the distribution of A_s . Our typical values of ϵ and r are relatively close to those reported to Dias et al., although not the same. However, conversely, our mass spectra are in closer agreement with McAllister et al. We find a population of trajectories yielding red values for n_s that was not identified by previous analyses. The observational relevance of this population is not yet clear because their spectra almost certainly contain interesting features.

Despite these differences, there are many areas of agreement between our results and those reported by earlier studies. The overall shape of the mass spectrum, the form (but not normalization) of the r -vs.- n_s correlation, the occurrence of rapid transits between different minima of the angular fields, the presence of strong anticorrelation between field fluctuations at horizon exit (‘destructive interference’ in the language of McAllister et al.) and possible transgressions of the ‘consistency bound’ are all points of agreement. Although not discussed explicitly in §4, our catalogue reproduces a similar probability of inflation and distribution of total number of e-folds N_{tot} to those reported by Agarwal et al. However, Agarwal et al. gave a persuasive analytic argument for the functional form of the distribution of N_{tot} , which suggests it does not depend sensitively on properties of the potential.

A natural question is whether our conclusions are reliable given the apparent discrepancies between different analyses of the model. Ultimately this will require forensic comparison between the separate implementations of the D3-brane potential. The most optimistic outlook is that these differences reflect only minor divergences in construction of the potential, against which observables may be fairly robust, as in §4.3. The broad qualitative agreement between all three analyses apparently does suggest there can not be very significant differences in the structure of the D3-brane potential, at least when it is able to support an extended epoch of inflation.

To assist future comparison we have attempted to give enough detail in §2 that it will be possible for third parties to replicate our analysis. Also, we have made our model specification and sampling parameters available to download from the Zenodo open data repository. These files are provided under a permissive Creative Commons attribution license.

This situation illustrates the advantages of a standardized format for specification of inflationary models, analogous to the *Universal FeynRules Output* format used in the collider phenomenology community to specify the particle content, coupling constants and interactions of a model [3]. As inflationary models become more complex, there seems a persuasive



argument for the community to converge on a standardized way to exchange similar specifications.

Acknowledgments

We would like to thank Peter Adshead, Nishant Agarwal, Mafalda Dias, Anatoly Dymarsky, Jonny Frazer and Sébastien Renaux-Petel for helpful correspondence. An early version of the **CppTransport** interface to **CosmoSIS** was written by Sean Butchers, whom we thank for assistance during development of the pipeline described in §3. The ‘by hand’ fits for n_t using smoothed power spectra were done in conjunction with Thomas Butler and Jordan Ramsay–Clements. DS acknowledges support from STFC consolidated grants ST/P000525/1 and ST/T000473/1. KM acknowledges support from STFC training grant ST/S505766/1. AM acknowledges support from the University of Sussex Junior Research Associate scheme and a Royal Astronomical Society Undergraduate Fellowship.

A Data availability

The primary data product generated for the work reported in this paper is our trajectory catalogue. We have made this available from the Zenodo open-access repository, together with the **CppTransport** model file that documents our construction of the D3-brane potential and its parametrization. We also include configuration files for the **CosmoSIS** pipeline used to compute observables for each trajectory. This pipeline depends on a modified interface between **CosmoSIS** and the **CLASS** Boltzmann code.

License	Creative Commons Attribution-NonCommercial 4.0 International 
Author	Kareem Marzouk, Alessandro Maraio & David Seery
DOI	 10.5281/zenodo.4742082
Attribution	Please cite zenodo.org DOI and this paper
Download	https://zenodo.org/record/4742082

Pipeline.—We explain in Appendix B that this model requires a custom version of **CppTransport**. Researchers wishing to replicate our pipeline should therefore use commit [35c5ad8f](#). This implements an interface to the **CosmoSIS** framework. It also includes the necessary patches to ingest pre-computed expressions for the inverse metric, the components of the connexion, and the Riemann tensor (also described in Appendix B). These pre-computed expressions are part of the Zenodo deposit.

The customizations in [35c5ad8f](#) include extensions to the model file grammar. A new release of **CppTransport** is planned that will include the **CosmoSIS** interface, but the model file format should be regarded as unstable and subject to change. The interface targets **CosmoSIS** 1.6 (commit [b33cd531e](#)).

Other data products.—The Planck2015 data products, including the TT , TE and EE an-

gular power spectra (and uncertainties) used in §4, can be obtained from the [Planck Legacy Archive](#).

B Computational requirements

It was explained in §1 that numerical predictions in the D3-brane model are challenging due to the complexity of the potential. In this Appendix we report in more detail on some of these challenges, in the hope that such details may be useful to researchers interested in incorporating observables derived from three-point functions in their analyses.

Translation step.—For both **CppTransport** and **PyTransport** the analysis of a model is a two-step process. First, a model description must be translated into customized C++ code that implements the transport equations for each correlation function. This requires a number of computations involving computer algebra. Second, this code must be processed by the C++ compiler before practical computations can be performed. There are resource implications in each step. Where timings are quoted, they relate to our test machine—an Apple 16" MacBook Pro with 16 GB and an i9-9880H running at 2.30 GHz.

An initial difficulty is that the **CppTransport** translator does not work successfully out-of-the-box for this model, because the **GiNaC** library on which it relies performs poorly when computing the inverse conifold metric. This is somewhat surprising given that the inversion is not particularly difficult, but likely reflects the fact that **GiNaC** is not optimized for matrix operations. Instead, we perform the inversion with **SymPy** and allow **CppTransport** to read in the result of the calculation. It is likely that future versions of **CppTransport** will allow the inverse field-space metric to be specified explicitly as part of the model description. While this reduces the degree of automation in the analysis, it allows more potent tools such as **SymPy** or **Mathematica** to be used for those parts of the calculation to which they are best suited.

We find there are benefits to following the same procedure for the components of the connexion and the Riemann tensor. Using **SymPy** to pre-compute these leads to a significant reduction in the time required for the **CppTransport** translator to perform common sub-expression elimination (‘CSE’), which is needed to keep time and memory requirements in check during the compile stage. This happens because the CSE algorithm used in **CppTransport** does not perform well with very large expressions due to design constraints imposed by **GiNaC**.

With these choices, we find it takes of order ~ 1 hr for **CppTransport** to perform translation on our test machine. While this is not insignificant, the procedure need only be done once.

Compile step.—**CppTransport** produces a *core* .h file of size ~ 26 Mb and an MPI *implementation* .h file of size ~ 800 kb. (For details, see Ref. [5].) In future there may be some scope to reduce the size of the core file by more intelligent pooling of lengthy expressions. Code of this size represents a considerable workload for the compiler, but is still practical with modern systems. We find that Clang is able to compile the model in between 10 min and 20 min, with the exact time depending on the platform and the version of Clang in use. Memory usage

peaks between 3 Gb and 4 Gb. We have tested Clang 9 and Clang 10 on Linux and macOS platforms (the latter in the guise of Apple Clang 11 and 12).

GCC is also able to process the model, but it returns significantly slower compile times and has much greater resource utilization. With GCC 10, peak memory usage was recorded in the vicinity of 100 Gb, which may be prohibitive in a virtualized environment or on systems with slow virtual memory. On our test machine, compilation did not terminate in a reasonable time, likely due to performance issues associated with repeated paging to swap. However, we have successfully compiled using GCC on larger machines, including the HPC cluster used to compute our primary catalogue. On these machines the compile time was of order 1 hour. The measurements reported here are not definitive, and are intended only as a guide to relative performance. In particular, compilation performance depends strongly on CPU properties.

Its smaller footprint makes Clang much easier to deploy in a resource-constrained environment such as a virtual machine or Docker container. Subject to this proviso, we find Docker to be a convenient tool to deploy **CosmoSIS** and **CppTransport** together.

Compute time.—Finally, we consider typical compute times for samples of the inflationary two- and three-point functions. Although there is some variation, computation of a single k -mode of the two-point function takes a few seconds. The integration time for modes of the three-point function depends on the momentum configuration. Equilateral and folded configurations take a few hundred seconds, with folded configuration typically being between 1.5 and 2.5 times more expensive than the equilateral. Squeezed configurations are most expensive. For $\beta = 0.9$, corresponding to squeezing $k_3/k_t = 0.05$, the integration is between 10 and 15 times more expensive compared to equilateral configurations. For $\beta = 0.95$, corresponding to squeezing $k_3/k_t = 0.025$, the integration is between 10 and 20 times more expensive compared to equilateral configurations.

In Fig. 20 we plot the distribution of compute times for the entire set of 55,000 trajectories in our primary catalogue that satisfy the cut $A_s < 10^{-4}$. The individual calculations that contribute to this total are listed in §3; note that there is no computation of any squeezed configurations. A majority of trajectories ($\sim 70\%$) complete in less than 1,000 s, and most ($\sim 95\%$) complete in less than 1,500 s. The bimodality is due to trajectories for which we cannot compute the Planck2015 likelihood because there are too few total e-folds to sample the power spectrum on the largest necessary scale (see §3). For these trajectories we do not need to obtain a separate sample of \mathcal{P}_ζ for use by **CLASS**, making the calculation substantially shorter.

Although not displayed here, compute times in **PyTransport** are comparable to (if generally slightly slower than) those reported for **CppTransport**. Therefore, in this model, inclusion of three-point function observables is likely too slow for use in practical parameter estimation using Markov Chain Monte Carlo methods. It might be possible to compute the primordial two-point function directly from the model, if desired, and providing not too many sample points are used.

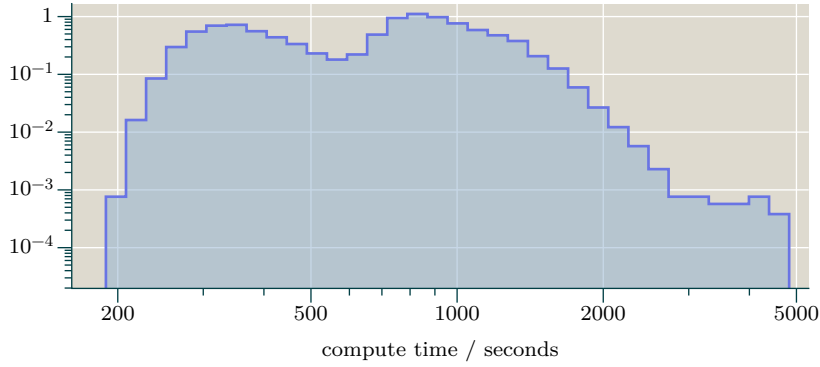


Figure 20. Distribution of integration times over our primary catalogue, measured in seconds. We have excluded a tail of rare trajectories up to 10^6 seconds. The bimodality is due to trajectories for which we cannot compute the Planck2015 likelihood.

C Transport equations for the spectral index

In this Appendix we briefly explain the transport computation of the scalar and tensor spectral indices. The superhorizon version of this calculation was given in Ref. [12], and extended to subhorizon scales in Ref. [14]. The discussion given here follows Ref. [14] with some refinements.

C.1 Scalar spectral index

First consider computation of the spectral index for ζ . As explained in §3.1.2, we start from the two-point function (3.7) on phase space, and define the ‘spectral matrix’ n^{AB} to satisfy [12]

$$n^{\text{AB}}(k) = \frac{d\Sigma^{\text{AB}}(k)}{d \ln k}. \quad (\text{C.1})$$

The ζ two point function (3.1a) can be expressed at tree level in terms of Σ^{AB} using

$$P_\zeta = N_{\text{A}} N_{\text{B}} \Sigma^{\text{AB}} + \text{O}(1 \text{ loop}), \quad (\text{C.2})$$

where the coefficients N_{A} may be obtained from standard perturbation theory or the separate universe formula, and are momentum-independent when the mode k is more than a few e-folds outside the horizon [32, 74]. It follows that

$$\frac{dP_\zeta}{d \ln k} \approx N_{\text{A}} N_{\text{B}} n^{\text{AB}}, \quad (\text{C.3})$$

from which the result (3.8) for n_s can be obtained.

Transport equation.—A transport equation for n^{AB} can be obtained by differentiating the transport equation for Σ^{AB} . This yields

$$\frac{dn^{\text{AB}}}{dN} = u^{\text{A}}_{\text{C}} n^{\text{CB}} + u^{\text{B}}_{\text{C}} n^{\text{AC}} + \frac{du^{\text{A}}_{\text{C}}}{d \ln k} \Sigma^{\text{CB}} + \frac{du^{\text{B}}_{\text{C}}}{d \ln k} \Sigma^{\text{AC}} + \text{O}(1 \text{ loop}). \quad (\text{C.4})$$

The result is a coupled system of ordinary differential equations for $\Sigma^{\mathbb{A}\mathbb{B}}$ and $n^{\mathbb{A}\mathbb{B}}$. For the definition of the ‘ u -tensor’ $u^{\mathbb{A}}_{\mathbb{B}}$, see Dias et al. [14, 15]. When the transport equation (C.4) is expressed with N as the independent variable, it can be written

$$u^{\mathbb{A}}_{\mathbb{B}} = \begin{pmatrix} 0 & \delta^{\mathbb{A}}_{\mathbb{B}} \\ \mathcal{M}^{\mathbb{A}}_{\mathbb{B}} & -(3 - \epsilon)\delta^{\mathbb{A}}_{\mathbb{B}} \end{pmatrix}, \quad (\text{C.5})$$

where A, B are species labels corresponding to the phase space indices \mathbb{A}, \mathbb{B} . Recall that these indices run over the fields *and* momenta. Therefore, when a phase space index such as \mathbb{A} runs over its entire range the corresponding species label A runs over its range twice. The matrix $\mathcal{M}^{\mathbb{A}}_{\mathbb{B}}$ is an effective mass matrix,

$$\mathcal{M}^{\mathbb{A}}_{\mathbb{B}} = -\frac{k^2}{a^2 H^2} \delta^{\mathbb{A}}_{\mathbb{B}} - \frac{M^{\mathbb{A}}_{\mathbb{B}}}{H^2}, \quad (\text{C.6})$$

where $M^{\mathbb{A}}_{\mathbb{B}}$ is the species mass matrix (3.6) appearing in the Lagrangian. Eq. (C.6) shows that the k -dependence of $u^{\mathbb{A}}_{\mathbb{B}}$ is exponentially suppressed on superhorizon scales. However, in this case it cannot be neglected. In the formula $P_{\zeta} \approx N_{\mathbb{A}} N_{\mathbb{B}} \Sigma^{\mathbb{A}\mathbb{B}}$ we evaluate $N_{\mathbb{A}}$ only far outside the horizon where $k^2/(a^2 H^2)$ is entirely negligible. In (C.4) we integrate over times when k is comparable to or smaller than the horizon scale. For this regime the $k^2/(a^2 H^2)$ term is important in fixing the correct amplitude of $n^{\mathbb{A}\mathbb{B}}$ at horizon exit and can not be dropped.

Initial conditions.—Eq. (C.4) can be solved simultaneously with the transport equation for $\Sigma^{\mathbb{A}\mathbb{B}}$, and future versions of **CppTransport** will do this by default. (The necessary functionality is already in the 201901 branch of the [GitHub repository](#) for those who wish to make use of it.) To proceed we require suitable initial conditions. A suitable set of initial values were given by Dias et al. [14], but these were truncated at leading order.²⁸ In this paper, in an attempt to improve convergence with fewer e-folds of subhorizon evolution, we include subleading terms in both the slow-roll expansion and $k/(aH)$.

A next-order expression for the scalar two-point function was given in Ref. [117],

$$\langle \delta X^A(\mathbf{k}_1, t_1) \delta X^B(\mathbf{k}_2, t_2) \rangle = (2\pi)^3 \delta(\mathbf{k}_1 + \mathbf{k}_2) [w(t_1)^A_I]^\dagger w(t_2)^{BI}, \quad (\text{C.7})$$

where the superscript ‘ \dagger ’ denotes complex conjugation, A is an index in the field tangent space at time t_1 , B is a similar index at time t_2 , and indices I, J, \dots , label the field tangent space at an arbitrary earlier time $t_* < t_1, t_2$ characterized by horizon exit of a fiducial mode k_* . As usual, all of these indices should be raised and lowered with the field-space metric evaluated at the appropriate field-space coordinates. We are interested in the equal-time commutator for which $t_1 = t_2 = t$, with t (corresponding to conformal time η) not too far from horizon exit of the mode $k = |\mathbf{k}_1| = |\mathbf{k}_2|$. To avoid the logarithm $\ln(-k_*\eta)$ in Eq. (C.8) below becoming large at this time we must usually choose t_* to be roughly comparable to t . The usual choice is to take t_* to be the moment when $k/(aH) = 1$. Up to next-order in the

²⁸In Ref. [14] the initial conditions are given for a different matrix $\tilde{n}^{\mathbb{A}\mathbb{B}} = (d/d \ln k)(k^3 \Sigma^{\mathbb{A}\mathbb{B}})$, in which the factor $1/k^3$ in the ordinary power spectrum is removed. With this definition, Eq. (3.8) should be adjusted so the numerical constant 4 appearing on the right-hand side becomes 1.

slow-roll expansion, but without making any approximation for the explicit time dependence, the wavefunction matrix w^A_I can be written²⁹

$$w(t)^A_I \equiv \frac{i}{\sqrt{2k^3}} H_* \Pi^A_K \left((1 - ik\eta) e^{ik\eta} \delta^K_I + \epsilon_* \left[\ln(-k_*\eta) - 1 \right] (1 - ik\eta) e^{ik\eta} \delta^K_I \right. \\ \left. + \left(\epsilon \delta^K_I - \frac{M^K_I}{3H^2} \right)_* \left[2e^{ik\eta} + i\frac{\pi}{2} (1 - ik\eta) e^{ik\eta} - (1 + ik\eta) e^{-ik\eta} \int_{-\infty}^{k\eta} \frac{dz}{z} e^{2iz} \right] \right) \quad (\text{C.8})$$

where a subscript ‘*’ indicates evaluation at the time t_* , $\eta \approx \int_t^\infty dt'/a(t')$ is the conformal time corresponding to the evaluation time t of the wavefunction, and Π^A_I is the parallel propagator on field space evaluated on the inflationary trajectory connecting the field-space coordinates at times t and t_* . The first term in brackets is lowest-order in the slow-roll expansion. The second and third terms exhaust the next-order corrections. For further details of Eq. (C.8) we refer to the literature [117].

Subhorizon limit.—We wish to use (C.8) to supply initial conditions for n^{AB} when k is on modestly subhorizon scales for which $|k\eta| \approx k/(aH)$ is in the range 5 to 10. To do so, Ref. [14] retained only the term at lowest order in slow-roll and highest order in $|k\eta|$. Here we retain subleading terms in both expansions.

First, Eq. (C.8) can be used to derive correlation functions involving the momenta $\pi^A \equiv dX^A/dN$. To do so we express d/dN in terms of η , up to next-order in the slow-roll expansion, using $d/dN = (aH)^{-1} d/d\eta$. Beginning with the unequal-time correlation function, the N derivative on each momentum operator π^A can be brought outside the expectation brackets, and the result evaluated by differentiation of the wavefunction factors (C.8). The equal-time limit should be taken only after all such differentiations have been carried out.

Second, after retaining terms in the ww product only up to next-order in the slow-roll expansion, we differentiate with respect to $\ln k$. This determines the element of the spectral matrix corresponding to each correlation function. Note that the evaluation time η is fixed and does not vary between k -modes. The same is true for the arbitrary evaluation time t_* : neither quantity generates any contribution when differentiated with respect to k . Finally, we expand in inverse powers of $k/(aH)$ and retain the leading- and next-order terms. This yields

$$\frac{d}{d \ln k} \langle \delta X^A \delta X^B \rangle' = -\Pi^A_I \Pi^B_J \frac{1}{2ka^2} \left(G^{IJ} + \frac{3}{2} \frac{a^2 H^2}{k^2} \left((2 - \epsilon) G^{IJ} - \frac{M_*^{IJ}}{H_*^2} \right) + \dots \right), \quad (\text{C.9a})$$

$$\frac{d}{d \ln k} \langle \delta X^A \delta \pi^B \rangle' = \Pi^A_I \Pi^B_J \frac{1}{2ka^2} \left((1 - \epsilon) G^{IJ} - \frac{15}{4} \frac{a^4 H^4}{k^4} \left(3\epsilon G^{IJ} - \frac{M_*^{IJ}}{H_*^2} \right) + \dots \right), \quad (\text{C.9b})$$

$$\frac{d}{d \ln k} \langle \delta \pi^A \delta \pi^B \rangle' = \Pi^A_I \Pi^B_J \frac{k}{2H^2 a^4} \left(G^{IJ} + \frac{1}{2} \frac{a^2 H^2}{k^2} \left(3\epsilon G^{IJ} - \frac{M_*^{IJ}}{H_*^2} \right) + \dots \right), \quad (\text{C.9c})$$

²⁹In Ref. [117] this expression was given for a flat field manifold. The generalization to a curved field-space was considered in Ref. [57], in which the (C.8) was used in the limit $|k\eta| \rightarrow 0$ but this expression did not

where the notation $\langle \dots \rangle'$ means that the momentum-conservation δ -function $(2\pi)^3 \delta(\mathbf{k}_1 + \mathbf{k}_2)$ has been dropped. To write Eqs. (C.9a)–(C.9c) we have combined terms to remove explicit dependence on t_* . Therefore a , H and ϵ should be determined at the evaluation time for the correlation function, and at lowest order we can take the Hubble-normalized mass matrix M_*^{IJ}/H_*^2 to be evaluated at the same time. Since $\Pi^A_I \Pi^B_J G^{IJ} = G^{AB}$ this means we can take all terms in Eqs. (C.9a)–(C.9c) to be evaluated at the same time and drop the parallel propagator factors.

C.2 Tensor spectral index

A similar analysis applies for the tensor spectral index. Each polarization behaves like an exactly massless scalar field, up to normalization. Therefore (C.9a)–(C.9c) apply, with $M^{IJ} = 0$. We need only one scalar field, and to account for the normalization of the tensor polarizations we should take $G_{IJ} \rightarrow M_{\text{P}}^2/2$, $G^{IJ} \rightarrow 2/M_{\text{P}}^2$.

We write the momentum for the tensor polarizations as $\pi_s = d\gamma_s/dN$ [15]. Then it follows that

$$\frac{d}{d \ln k} \langle \gamma_s \gamma_{s'} \rangle' = -\frac{1}{M_{\text{P}}^2} \frac{1}{ka^2} \delta_{ss'} \left(1 + \frac{3}{2} \frac{a^2 H^2}{k^2} (2 - \epsilon) + \dots \right), \quad (\text{C.10a})$$

$$\frac{d}{d \ln k} \langle \gamma_s \pi_{s'} \rangle' = \frac{1}{M_{\text{P}}^2} \frac{1}{ka^2} \delta_{ss'} \left((1 - \epsilon) - \frac{45\epsilon}{4} \frac{a^4 H^4}{k^4} + \dots \right), \quad (\text{C.10b})$$

$$\frac{d}{d \ln k} \langle \pi_s \pi_{s'} \rangle' = \frac{1}{M_{\text{P}}^2} \frac{k}{H^2 a^4} \delta_{ss'} \left(1 + \frac{3\epsilon}{2} \frac{a^2 H^2}{k^2} + \dots \right), \quad (\text{C.10c})$$

from which the necessary initial conditions can be extracted.

appear explicitly.

References

- [1] T. Appelquist and J. Carazzone, *Infrared Singularities and Massive Fields*, *Phys. Rev. D* **11** (1975) 2856.
- [2] D. Baumann and L. McAllister, *Inflation and String Theory*, Cambridge Monographs on Mathematical Physics. Cambridge University Press, 2015, [10.1017/CBO9781316105733](#), [[1404.2601](#)].
- [3] C. Degrande, C. Duhr, B. Fuks, D. Grellscheid, O. Mattelaer and T. Reiter, *UFO – The Universal FeynRules Output*, *Comput. Phys. Commun.* **183** (2012) 1201 [[1108.2040](#)].
- [4] A. Alloul, N. D. Christensen, C. Degrande, C. Duhr and B. Fuks, *FeynRules 2.0 – A complete toolbox for tree-level phenomenology*, *Comput. Phys. Commun.* **185** (2014) 2250 [[1310.1921](#)].
- [5] D. Seery, *CppTransport: a platform to automate calculation of inflationary correlation functions*, [1609.00380](#).
- [6] S. Butchers and D. Seery, *Numerical evaluation of inflationary 3-point functions on curved field space—with the transport method & CppTransport*, *JCAP* **1807** (2018) 031 [[1803.10563](#)].
- [7] D. J. Mulryne and J. W. Ronayne, *PyTransport: A Python package for the calculation of inflationary correlation functions*, [1609.00381](#).
- [8] J. W. Ronayne and D. J. Mulryne, *Numerically evaluating the bispectrum in curved field-space—with PyTransport 2.0*, *JCAP* **1801** (2018) 023 [[1708.07130](#)].
- [9] M. Dias, J. Frazer and A. R. Liddle, *Multifield consequences for D-brane inflation*, *JCAP* **1206** (2012) 020 [[1203.3792](#)].
- [10] D. J. Mulryne, D. Seery and D. Wesley, *Moment transport equations for non-Gaussianity*, *JCAP* **1001** (2010) 024 [[0909.2256](#)].
- [11] D. J. Mulryne, D. Seery and D. Wesley, *Moment transport equations for the primordial curvature perturbation*, *JCAP* **1104** (2011) 030 [[1008.3159](#)].
- [12] M. Dias and D. Seery, *Transport equations for the inflationary spectral index*, *Phys. Rev. D* **85** (2012) 043519 [[1111.6544](#)].
- [13] G. J. Anderson, D. J. Mulryne and D. Seery, *Transport equations for the inflationary trispectrum*, *JCAP* **10** (2012) 019 [[1205.0024](#)].
- [14] M. Dias, J. Frazer and D. Seery, *Computing observables in curved multifield models of inflation—A guide (with code) to the transport method*, *JCAP* **1512** (2015) 030 [[1502.03125](#)].
- [15] M. Dias, J. Frazer, D. J. Mulryne and D. Seery, *Numerical evaluation of the bispectrum in multiple field inflation—the transport approach with code*, *JCAP* **1612** (2016) 033 [[1609.00379](#)].
- [16] S. Weinberg, *Quantum contributions to cosmological correlations*, *Phys. Rev. D* **72** (2005) 043514 [[hep-th/0506236](#)].
- [17] S. Weinberg, *Quantum contributions to cosmological correlations. II. Can these corrections become large?*, *Phys. Rev. D* **74** (2006) 023508 [[hep-th/0605244](#)].
- [18] D. Seery, *Infrared effects in inflationary correlation functions*, *Class. Quant. Grav.* **27** (2010) 124005 [[1005.1649](#)].
- [19] D. Seery, *Magnetogenesis and the primordial non-gaussianity*, *JCAP* **08** (2009) 018 [[0810.1617](#)].

- [20] R. Flauger, M. Mirbabayi, L. Senatore and E. Silverstein, *Productive Interactions: heavy particles and non-Gaussianity*, *JCAP* **10** (2017) 058 [[1606.00513](#)].
- [21] D. Seery, *A parton picture of de Sitter space during slow-roll inflation*, *JCAP* **05** (2009) 021 [[0903.2788](#)].
- [22] N. Arkani-Hamed and J. Maldacena, *Cosmological Collider Physics*, [1503.08043](#).
- [23] J. Elliston, D. J. Mulryne, D. Seery and R. Tavakol, *Evolution of f_{NL} to the adiabatic limit*, *JCAP* **1111** (2011) 005 [[1106.2153](#)].
- [24] D. Seery, D. J. Mulryne, J. Frazer and R. H. Ribeiro, *Inflationary perturbation theory is geometrical optics in phase space*, *JCAP* **1209** (2012) 010 [[1203.2635](#)].
- [25] J. Garcia-Bellido and D. Wands, *Metric perturbations in two field inflation*, *Phys. Rev. D* **53** (1996) 5437 [[astro-ph/9511029](#)].
- [26] S. Weinberg, *Adiabatic modes in cosmology*, *Phys. Rev. D* **67** (2003) 123504 [[astro-ph/0302326](#)].
- [27] S. Weinberg, *Must cosmological perturbations remain non-adiabatic after multi-field inflation?*, *Phys. Rev. D* **70** (2004) 083522 [[astro-ph/0405397](#)].
- [28] S. Weinberg, *Can non-adiabatic perturbations arise after single-field inflation?*, *Phys. Rev. D* **70** (2004) 043541 [[astro-ph/0401313](#)].
- [29] G. I. Rigopoulos and E. P. S. Shellard, *The separate universe approach and the evolution of nonlinear superhorizon cosmological perturbations*, *Phys. Rev. D* **68** (2003) 123518 [[astro-ph/0306620](#)].
- [30] D. H. Lyth, K. A. Malik and M. Sasaki, *A General proof of the conservation of the curvature perturbation*, *JCAP* **05** (2005) 004 [[astro-ph/0411220](#)].
- [31] J. Elliston, D. Mulryne, D. Seery and R. Tavakol, *Evolution of non-Gaussianity in multi-scalar field models*, *Int. J. Mod. Phys. A* **26** (2011) 3821 [[1107.2270](#)].
- [32] J. Elliston, S. Orani and D. J. Mulryne, *General analytic predictions of two-field inflation and perturbative reheating*, *Phys. Rev. D* **89** (2014) 103532 [[1402.4800](#)].
- [33] D. Blas, J. Lesgourgues and T. Tram, *The Cosmic Linear Anisotropy Solving System (CLASS) II: Approximation schemes*, *JCAP* **1107** (2011) 034 [[1104.2933](#)].
- [34] J. Zuntz, M. Paterno, E. Jennings, D. Rudd, A. Manzotti, S. Dodelson et al., *CosmoSIS: modular cosmological parameter estimation*, *Astron. Comput.* **12** (2015) 45 [[1409.3409](#)].
- [35] P. D. Meerburg et al., *Primordial Non-Gaussianity*, [1903.04409](#).
- [36] G. R. Dvali and S. H. H. Tye, *Brane inflation*, *Phys. Lett. B* **450** (1999) 72 [[hep-ph/9812483](#)].
- [37] C. P. Burgess, M. Majumdar, D. Nolte, F. Quevedo, G. Rajesh and R.-J. Zhang, *The Inflationary brane anti-brane universe*, *JHEP* **07** (2001) 047 [[hep-th/0105204](#)].
- [38] G. R. Dvali, Q. Shafi and S. Solganik, *D-brane inflation*, in *4th European Meeting From the Planck Scale to the Electroweak Scale (Planck 2001) La Londe les Maures, Toulon, France, May 11-16, 2001*, 2001, [hep-th/0105203](#).
- [39] S. Kachru, R. Kallosh, A. D. Linde, J. M. Maldacena, L. P. McAllister and S. P. Trivedi, *Towards inflation in string theory*, *JCAP* **0310** (2003) 013 [[hep-th/0308055](#)].
- [40] S. Kachru, R. Kallosh, A. D. Linde and S. P. Trivedi, *De Sitter vacua in string theory*, *Phys. Rev. D* **68** (2003) 046005 [[hep-th/0301240](#)].

- [41] L. Randall and R. Sundrum, *A Large mass hierarchy from a small extra dimension*, *Phys. Rev. Lett.* **83** (1999) 3370 [[hep-ph/9905221](#)].
- [42] L. Randall and R. Sundrum, *An Alternative to compactification*, *Phys. Rev. Lett.* **83** (1999) 4690 [[hep-th/9906064](#)].
- [43] D. Baumann, A. Dymarsky, I. R. Klebanov, J. M. Maldacena, L. P. McAllister and A. Murugan, *On D3-brane Potentials in Compactifications with Fluxes and Wrapped D-branes*, *JHEP* **11** (2006) 031 [[hep-th/0607050](#)].
- [44] D. Baumann, A. Dymarsky, I. R. Klebanov, L. McAllister and P. J. Steinhardt, *A Delicate universe*, *Phys. Rev. Lett.* **99** (2007) 141601 [[0705.3837](#)].
- [45] D. Baumann, A. Dymarsky, I. R. Klebanov and L. McAllister, *Towards an Explicit Model of D-brane Inflation*, *JCAP* **0801** (2008) 024 [[0706.0360](#)].
- [46] D. Baumann, A. Dymarsky, S. Kachru, I. R. Klebanov and L. McAllister, *Holographic Systematics of D-brane Inflation*, *JHEP* **03** (2009) 093 [[0808.2811](#)].
- [47] D. Baumann, A. Dymarsky, S. Kachru, I. R. Klebanov and L. McAllister, *Compactification Effects in D-brane Inflation*, *Phys. Rev. Lett.* **104** (2010) 251602 [[0912.4268](#)].
- [48] D. Baumann, A. Dymarsky, S. Kachru, I. R. Klebanov and L. McAllister, *D3-brane Potentials from Fluxes in AdS/CFT*, *JHEP* **06** (2010) 072 [[1001.5028](#)].
- [49] S. S. Gubser, *Einstein manifolds and conformal field theories*, *Phys. Rev.* **D59** (1999) 025006 [[hep-th/9807164](#)].
- [50] A. Ceresole, G. Dall'Agata, R. D'Auria and S. Ferrara, *Spectrum of type IIB supergravity on $AdS(5) \times T^{1,1}$: Predictions on $N = 1$ SCFTs*, *Phys. Rev.* **D61** (2000) 066001 [[hep-th/9905226](#)].
- [51] A. Ceresole, G. Dall'Agata and R. D'Auria, *KK spectroscopy of type IIB supergravity on $AdS(5) \times T^{1,1}$* , *JHEP* **11** (1999) 009 [[hep-th/9907216](#)].
- [52] N. Agarwal, R. Bean, L. McAllister and G. Xu, *Universality in D-brane Inflation*, *JCAP* **1109** (2011) 002 [[1103.2775](#)].
- [53] M. J. Mortonson, H. V. Peiris and R. Easther, *Bayesian Analysis of Inflation: Parameter Estimation for Single Field Models*, *Phys. Rev. D* **83** (2011) 043505 [[1007.4205](#)].
- [54] R. Easther and H. V. Peiris, *Bayesian Analysis of Inflation II: Model Selection and Constraints on Reheating*, *Phys. Rev. D* **85** (2012) 103533 [[1112.0326](#)].
- [55] D. Larson et al., *Seven-Year Wilkinson Microwave Anisotropy Probe (WMAP) Observations: Power Spectra and WMAP-Derived Parameters*, *Astrophys. J. Suppl.* **192** (2011) 16 [[1001.4635](#)].
- [56] WMAP collaboration, *Seven-Year Wilkinson Microwave Anisotropy Probe (WMAP) Observations: Cosmological Interpretation*, *Astrophys. J. Suppl.* **192** (2011) 18 [[1001.4538](#)].
- [57] J. Elliston, D. Seery and R. Tavakol, *The inflationary bispectrum with curved field-space*, *JCAP* **1211** (2012) 060 [[1208.6011](#)].
- [58] D. J. Mulryne, *Transporting non-Gaussianity from sub to super-horizon scales*, *JCAP* **1309** (2013) 010 [[1302.3842](#)].
- [59] L. McAllister, S. Renaux-Petel and G. Xu, *A Statistical Approach to Multifield Inflation: Many-field Perturbations Beyond Slow Roll*, *JCAP* **1210** (2012) 046 [[1207.0317](#)].

- [60] X. Chen and Y. Wang, *Large non-Gaussianities with Intermediate Shapes from Quasi-Single Field Inflation*, *Phys. Rev. D* **81** (2010) 063511 [[0909.0496](#)].
- [61] X. Chen and Y. Wang, *Quasi-Single Field Inflation and Non-Gaussianities*, *JCAP* **04** (2010) 027 [[0911.3380](#)].
- [62] J.-O. Gong, S. Pi and M. Sasaki, *Equilateral non-Gaussianity from heavy fields*, *JCAP* **11** (2013) 043 [[1306.3691](#)].
- [63] T. Hertog and O. Janssen, *Sharp Predictions from Eternal Inflation Patches in D-brane Inflation*, *JCAP* **04** (2017) 011 [[1512.02722](#)].
- [64] A. Vilenkin, *Topological inflation*, *Phys. Rev. Lett.* **72** (1994) 3137 [[hep-th/9402085](#)].
- [65] A. D. Linde and D. A. Linde, *Topological defects as seeds for eternal inflation*, *Phys. Rev. D* **50** (1994) 2456 [[hep-th/9402115](#)].
- [66] S. A. Kim, A. R. Liddle and D. Seery, *Non-gaussianity in axion Nflation models*, *Phys. Rev. Lett.* **105** (2010) 181302 [[1005.4410](#)].
- [67] D. Baumann and L. McAllister, *A Microscopic Limit on Gravitational Waves from D-brane Inflation*, *Phys. Rev. D* **75** (2007) 123508 [[hep-th/0610285](#)].
- [68] I. R. Klebanov and M. J. Strassler, *Supergravity and a confining gauge theory: Duality cascades and chi SB resolution of naked singularities*, *JHEP* **08** (2000) 052 [[hep-th/0007191](#)].
- [69] L. Romans, *New Compactifications of Chiral $N = 2d = 10$ Supergravity*, *Phys. Lett. B* **153** (1985) 392.
- [70] P. Candelas and X. C. de la Ossa, *Comments on Conifolds*, *Nucl. Phys. B* **342** (1990) 246.
- [71] E. Witten, *Phases of $N=2$ theories in two-dimensions*, *AMS/IP Stud. Adv. Math.* **1** (1996) 143 [[hep-th/9301042](#)].
- [72] I. R. Klebanov and E. Witten, *Superconformal field theory on three-branes at a Calabi–Yau singularity*, *Nucl. Phys. B* **536** (1998) 199 [[hep-th/9807080](#)].
- [73] S. B. Giddings, S. Kachru and J. Polchinski, *Hierarchies from fluxes in string compactifications*, *Phys. Rev. D* **66** (2002) 106006 [[hep-th/0105097](#)].
- [74] M. Sasaki and E. D. Stewart, *A general analytic formula for the spectral index of the density perturbations produced during inflation*, *Prog. Theor. Phys.* **95** (1996) 71 [[astro-ph/9507001](#)].
- [75] T. T. Nakamura and E. D. Stewart, *The Spectrum of cosmological perturbations produced by a multicomponent inflaton to second order in the slow roll approximation*, *Phys. Lett. B* **381** (1996) 413 [[astro-ph/9604103](#)].
- [76] S. Groot Nibbelink and B. van Tent, *Scalar perturbations during multiple field slow-roll inflation*, *Class. Quant. Grav.* **19** (2002) 613 [[hep-ph/0107272](#)].
- [77] C.-Y. Sun and D.-H. Zhang, *Non-gaussianity of general multiple-field inflationary models*, *Int. J. Mod. Phys. D* **15** (2006) 1259 [[astro-ph/0510709](#)].
- [78] G. Rigopoulos, E. Shellard and B. van Tent, *Non-linear perturbations in multiple-field inflation*, *Phys. Rev. D* **73** (2006) 083521 [[astro-ph/0504508](#)].
- [79] C. M. Peterson and M. Tegmark, *Testing multifield inflation: A geometric approach*, *Phys. Rev. D* **87** (2013) 103507 [[1111.0927](#)].
- [80] D. I. Kaiser, E. A. Mazenc and E. I. Sfakianakis, *Primordial Bispectrum from Multifield Inflation with Nonminimal Couplings*, *Phys. Rev. D* **87** (2013) 064004 [[1210.7487](#)].

- [81] F. Peter and H. Weyl, *Die Vollständigkeit der primitiven darstellungen einer geschlossenen kontinuierlichen gruppe*, *Mathematische Annalen* **97** (1927) 737.
- [82] A. Salam and J. Strathdee, *On Kaluza-Klein Theory*, *Annals Phys.* **141** (1982) 316.
- [83] A. Ceresole, G. Dall'Agata, R. D'Auria and S. Ferrara, *Superconformal field theories from IIB spectroscopy on $AdS(5) \times T^{1,1}$* , *Class. Quant. Grav.* **17** (2000) 1017 [[hep-th/9910066](#)].
- [84] S. Gandhi, L. McAllister and S. Sjörs, *A Toolkit for Perturbing Flux Compactifications*, *JHEP* **12** (2011) 053 [[1106.0002](#)].
- [85] L. McAllister, P. Schwaller, G. Servant, J. Stout and A. Westphal, *Runaway Relaxion Monodromy*, *JHEP* **02** (2018) 124 [[1610.05320](#)].
- [86] *The Rotation Groups*, in *Group Theory*, E. P. Wigner, ed., vol. 5 of *Pure and Applied Physics*, pp. 142–152, Elsevier, (1959), [DOI](#).
- [87] J. Schwinger, *On angular momentum*. 1, 1952, [10.2172/4389568](#).
- [88] D. Baumann and D. Green, *Equilateral Non-Gaussianity and New Physics on the Horizon*, *JCAP* **09** (2011) 014 [[1102.5343](#)].
- [89] C. Bauer and H. S. Do, *One loop integrals with XLOOPS-GiNaC*, *Comput. Phys. Commun.* **144** (2002) 154 [[hep-ph/0102231](#)].
- [90] R. Easther, J. Frazer, H. V. Peiris and L. C. Price, *Simple predictions from multifield inflationary models*, *Phys. Rev. Lett.* **112** (2014) 161302 [[1312.4035](#)].
- [91] A. R. Liddle and S. M. Leach, *How long before the end of inflation were observable perturbations produced?*, *Phys. Rev. D* **68** (2003) 103503 [[astro-ph/0305263](#)].
- [92] P. Adshead and R. Easther, *Constraining Inflation*, *JCAP* **10** (2008) 047 [[0802.3898](#)].
- [93] P. Adshead, R. Easther, J. Pritchard and A. Loeb, *Inflation and the Scale Dependent Spectral Index: Prospects and Strategies*, *JCAP* **02** (2011) 021 [[1007.3748](#)].
- [94] J. R. Fergusson and E. P. S. Shellard, *Primordial non-Gaussianity and the CMB bispectrum*, *Phys. Rev.* **D76** (2007) 083523 [[astro-ph/0612713](#)].
- [95] G. Rigopoulos, E. Shellard and B. van Tent, *A Simple route to non-Gaussianity in inflation*, *Phys. Rev. D* **72** (2005) 083507 [[astro-ph/0410486](#)].
- [96] PLANCK collaboration, *Planck 2015 results. XI. CMB power spectra, likelihoods, and robustness of parameters*, *Astron. Astrophys.* **594** (2016) A11 [[1507.02704](#)].
- [97] PLANCK collaboration, *Planck 2015 results. XIII. Cosmological parameters*, *Astron. Astrophys.* **594** (2016) A13 [[1502.01589](#)].
- [98] W. H. Kinney, *Horizon crossing and inflation with large eta*, *Phys. Rev. D* **72** (2005) 023515 [[gr-qc/0503017](#)].
- [99] J. Martin, H. Motohashi and T. Suyama, *Ultra Slow-Roll Inflation and the non-Gaussianity Consistency Relation*, *Phys. Rev. D* **87** (2013) 023514 [[1211.0083](#)].
- [100] M. H. Namjoo, H. Firouzjahi and M. Sasaki, *Violation of non-Gaussianity consistency relation in a single field inflationary model*, *EPL* **101** (2013) 39001 [[1210.3692](#)].
- [101] S. Mooij and G. A. Palma, *Consistently violating the non-Gaussian consistency relation*, *JCAP* **11** (2015) 025 [[1502.03458](#)].
- [102] A. E. Romano, S. Mooij and M. Sasaki, *Global adiabaticity and non-Gaussianity consistency condition*, *Phys. Lett. B* **761** (2016) 119 [[1606.04906](#)].

- [103] X. Chen, H. Firouzjahi, M. H. Namjoo and M. Sasaki, *A Single Field Inflation Model with Large Local Non-Gaussianity*, *EPL* **102** (2013) 59001 [[1301.5699](#)].
- [104] X. Chen, H. Firouzjahi, E. Komatsu, M. H. Namjoo and M. Sasaki, *In-in and δN calculations of the bispectrum from non-attractor single-field inflation*, *JCAP* **12** (2013) 039 [[1308.5341](#)].
- [105] Y.-F. Cai, X. Chen, M. H. Namjoo, M. Sasaki, D.-G. Wang and Z. Wang, *Revisiting non-Gaussianity from non-attractor inflation models*, *JCAP* **05** (2018) 012 [[1712.09998](#)].
- [106] M. Dias, J. Elliston, J. Frazer, D. Mulryne and D. Seery, *The curvature perturbation at second order*, *JCAP* **02** (2015) 040 [[1410.3491](#)].
- [107] D. Wands, K. A. Malik, D. H. Lyth and A. R. Liddle, *A New approach to the evolution of cosmological perturbations on large scales*, *Phys. Rev. D* **62** (2000) 043527 [[astro-ph/0003278](#)].
- [108] J. Meyers and E. R. M. Tarrant, *Perturbative Reheating After Multiple-Field Inflation: The Impact on Primordial Observables*, *Phys. Rev. D* **89** (2014) 063535 [[1311.3972](#)].
- [109] S. C. Hotinli, J. Frazer, A. H. Jaffe, J. Meyers, L. C. Price and E. R. M. Tarrant, *Effect of reheating on predictions following multiple-field inflation*, *Phys. Rev. D* **97** (2018) 023511 [[1710.08913](#)].
- [110] V. F. Mukhanov, *Gravitational Instability of the Universe Filled with a Scalar Field*, *JETP Lett.* **41** (1985) 493.
- [111] M. Sasaki, *Large Scale Quantum Fluctuations in the Inflationary Universe*, *Prog. Theor. Phys.* **76** (1986) 1036.
- [112] J. Garcia-Bellido, A. D. Linde and D. Wands, *Density perturbations and black hole formation in hybrid inflation*, *Phys. Rev. D* **54** (1996) 6040 [[astro-ph/9605094](#)].
- [113] J. M. Maldacena, *Non-Gaussian features of primordial fluctuations in single field inflationary models*, *JHEP* **05** (2003) 013 [[astro-ph/0210603](#)].
- [114] L. Senatore and M. Zaldarriaga, *On Loops in Inflation*, *JHEP* **12** (2010) 008 [[0912.2734](#)].
- [115] V. Assassi, D. Baumann and D. Green, *Symmetries and Loops in Inflation*, *JHEP* **02** (2013) 151 [[1210.7792](#)].
- [116] J. Frazer, *Predictions in multifield models of inflation*, *JCAP* **01** (2014) 028 [[1303.3611](#)].
- [117] M. Dias, R. H. Ribeiro and D. Seery, *The δN formula is the dynamical renormalization group*, *JCAP* **10** (2013) 062 [[1210.7800](#)].
- [118] E. J. Copeland, E. W. Kolb, A. R. Liddle and J. E. Lidsey, *Reconstructing the inflaton potential: Perturbative reconstruction to second order*, *Phys. Rev. D* **49** (1994) 1840 [[astro-ph/9308044](#)].
- [119] E. J. Copeland, E. W. Kolb, A. R. Liddle and J. E. Lidsey, *Reconstructing the inflation potential, in principle and in practice*, *Phys. Rev. D* **48** (1993) 2529 [[hep-ph/9303288](#)].
- [120] D. Babich, P. Creminelli and M. Zaldarriaga, *The Shape of non-Gaussianities*, *JCAP* **0408** (2004) 009 [[astro-ph/0405356](#)].
- [121] C. Burrage, R. H. Ribeiro and D. Seery, *Large slow-roll corrections to the bispectrum of noncanonical inflation*, *JCAP* **07** (2011) 032 [[1103.4126](#)].
- [122] A. J. Tolley and M. Wyman, *The Gelaton Scenario: Equilateral non-Gaussianity from multi-field dynamics*, *Phys. Rev. D* **81** (2010) 043502 [[0910.1853](#)].

- [123] C. T. Byrnes, D. Regan, D. Seery and E. R. M. Tarrant, *The hemispherical asymmetry from a scale-dependent inflationary bispectrum*, *JCAP* **06** (2016) 025 [[1511.03129](#)].
- [124] Z. Kenton and D. J. Mulryne, *The Separate Universe Approach to Soft Limits*, *JCAP* **10** (2016) 035 [[1605.03435](#)].
- [125] L. Alabidi, K. Malik, C. T. Byrnes and K.-Y. Choi, *How the curvaton scenario, modulated reheating and an inhomogeneous end of inflation are related*, *JCAP* **11** (2010) 037 [[1002.1700](#)].
- [126] M. Alvarez et al., *Testing Inflation with Large Scale Structure: Connecting Hopes with Reality*, [1412.4671](#).
- [127] J. Torrado and A. Lewis, *Cobaya: Code for Bayesian Analysis of hierarchical physical models*, [2005.05290](#).